Assessing uncertainty in models of the ocean carbon cycle

Vivian Scott

A thesis submitted for the degree of Doctor of Philosophy
The University of Edinburgh

November, 2009

Declaration

This thesis is an account of research undertaken between October 2005 and May 2009 in The School of Geosciences at The University of Edinburgh, Edinburgh, Scotland, United Kingdom. Except where explicitly stated, this thesis and the material presented in it are my own work and have not been submitted in whole or part for a degree in any university.

Vivian Scott
May, 2009

Acknowledgements

While this thesis carries my name, there are many, both in Edinburgh and further afield, who have contributed both directly and indirectly to the work contained in it.

Firstly, I must thank my supervisors, Helen Kettle and Chris Merchant, for their time, dedication and guidance throughout my PhD. Their support and advice has been invaluable in the work that culminates in this thesis. At the National Oceanography Centre Southampton, I wish to thank John Hemmings, Peter Challenor, Robin Hankin (now of Cambridge University), and Tom Anderson for their time, help and hospitality during visits to NOCS.

My PhD was funded through the NERC CASIX research centre, which in addition to providing a generous stipend and research budget, has given me broad support and an insight into collaborative academic research through its many members and annual meetings. This work has made extensive use of the HadOCC biogeochemical model. I wish to thank its orginators, John Palmer and Ian Totterdell of the Met Office, for allowing me to use it.

For the later stages of this work, I thank SAGES for the opportunity to make use of the ECDF computing facility, in particular Mike Mineter and Simon Tett for their considerable investment of time and help. Thanks also, to Robin Smith and Jonathan Gregory of Reading University, and other members of NCAS and the climate model research community for the use of, and their help with, the FAMOUS GCM.

Finally, back in Edinburgh, I wish to thank the many staff and students in the Crew Building for their help, and for providing a stimulating and entertaining environment in which to work over the past few years.

Vivian Scott

Abstract

In this thesis I explore the effect of parameter uncertainty in ocean biogeochemical models on the calculation of carbon uptake by the ocean. The ocean currently absorbs around a quarter of the annual anthropogenic CO_2 emissions to the atmosphere [Scholes et al., 2009], slowing the increase in radiative forcing associated with the increasing atmospheric CO_2 concentration. Ocean biogeochemical models have been developed to study the role of the ocean ecosystem in this process. Such models consist of a greatly simplified representation of the hugely complex ocean ecosystem. This simplification requires extensive parameterisation of the biological processes that convert inorganic carbon to and from organic carbon in the ocean.

The HadOCC ocean biogeochemical model is a Nutrient-Phytoplankton-Zooplankton-Detritus (NPZD) model that is used to represent the role of the ocean ecosystem in the global carbon cycle in the HadCM3 and FAMOUS GCMs. HadOCC uses twenty parameters to control the processes of biological growth, mortality, grazing and detrital sinking that control the uptake and cycling of carbon in the ocean ecosystem. These parameters represent highly complex and in some cases incompletely understood biological processes, and as a result are uncertain in value.

A sensitivity analysis is performed to identify the HadOCC parameters that due to uncertainty in value have the greatest possible effect on the exchange of CO_2 between the atmosphere and the ocean—the air-sea CO_2 flux. These are found to be the parameters that control phytoplankton growth in the well lit surface ocean, the formation of carbonate by marine organisms and the sinking of biological detritus.

The uncertainty in these parameters is found to cause changes to the air-sea CO_2 flux calculated by the FAMOUS GCM. The initial effect of these changes is equivalent to the order of the error of current estimates of the net annual carbon uptake by the ocean (2.2 ± 0.3 Pg C y^{-1} [Gruber et al., 2009], 2.2 ± 0.5 Pg C y^{-1} [Denman et al., 2007]). This indicates that while the effect of ocean biogeochemical parameter uncertainty is non-negligible, it is within the bounds of the uncertainty of the total (inorganic and organic) ocean carbon system, and is considerably less than the uncertainty in the carbon uptake of the terrestrial biosphere [Houghton, 2007]. However, as the ocean plays a crucial role in the global carbon cycle and the regulation of the Earth's climate, further understanding and better modelling of the role of the ocean ecosystem in the global carbon cycle and its reaction to anthropogenic climate forcing remains important.

Contents

List of Figures

List of Tables

Introduction

1.1 The big picture

The Earth's climate has unequivocally warmed in recent history [Solomon et al., 2007]. Anthropogenic development over the past two centuries has been shown to be 'very likely' responsible for this rapid change in the Earths climate [Solomon et al., 2007]. Understanding and mitigating climate change is one of the great challenges of the current era [Tol, 2008]. Global mean temperature has gradually risen with the increase in radiative forcing attributed to the increase in atmospheric green house gas concentrations due to human activity. Athropogenic CO_2 emissions from fossil fuel burning, deforestation and other processes form the most significant contribution to these green house gases [Forster et al., 2007]. Understanding the global carbon cycle, and its role in regulating the atmospheric CO_2 concentration, is crucial to predicting the future climate, and determining the appropriate mitigation required to avert, and adapt, to the effects of climate change [Houghton, 2007]. Global climate models (GCMs)[1] are the current state of the art in addressing this issue [Randall et al., 2007], but remain condensed and limited representations of the global climate system. Knowledge of these limitations and their effects is essential to interpret the results of, and to further develop, such models [Randall et al., 2007; Friedlingstein et al., 2006; Stainforth et al., 2005; Murphy et al., 2004].

The tiny algae, collectively known as phytoplankton, that inhabit the well-lit upper region of the ocean form the basis of a major part of the global carbon cycle [Riebesell et al., 2007; Denman et al., 2007]. Algal photosynthesis accounts for just under half the global total photosynthesis [Fasham, 2003], resulting in a net primary production of around 48 Pg carbon per year[2] [Field et al., 1998; Mackenzie et al., 2004; Houghton, 2007]. While much of this carbon is cycled through the upper ocean ecosystem, a significant fraction—around a fith—is exported to the deep ocean, where some eventually adds to, and is buried, in sea-bed sediments providing a geological time-scale carbon sink [Sarmiento and Gruber, 2006]. The ocean ecosystem responsible for this export is hugely complex, and, as highlighted by recent discoveries in the role of fish in the basic cycling of carbonate [Wilson et al., 2009], and bacterivory by phytoplankton [Zubkov and Tarran, 2008], remains incompletely understood. In spite of this, the basic structure is

[1] While also commonly referred to as 'Global Circulation Models' I feel that the title 'Global Climate Models' is more appropriate to this thesis.

[2] 1 Pg C is 1×10^{15} g C $= 1$ gigaton carbon.

sufficiently homogeneous to enable simple models to crudely represent the ocean ecosystem's role in the global carbon cycle. This requires extensive simplification and parameterisation of many complex processes, but enables their essential role to be captured for inclusion in global climate models. In this thesis I seek to understand the limitations that arise from these simplifications by studying the effect of the uncertainty of the parameters used to govern these parameterisations on the results of the models in which they are used. Here, I begin by outlining the processes that control the cycling of carbon between the atmosphere and ocean and then describe their inclusion in ocean biogeochemical models. I then move on to discuss the objectives and structure of this thesis and briefly outline the content of the subsequent chapters.

1.2 The fate of anthropogenic CO_2

The atmospheric concentration of CO_2 has increased dramatically over the last two centuries from a pre-industrial level of around 280ppm to a present day value of around 390ppm which is likely to increase [Forster et al., 2007]. The annual increase in atmospheric CO_2 concentration accounts for only half of the total annual CO_2 estimated to have been released into the atmosphere by the burning of fossil fuels for power generation, industry, transport and other activities—principally land use change—arising from the rapid development of modern societies. The remaining half of the anthropogenic CO_2 emissions have been absorbed by processes on the land or ocean, slowing the increase in the radiative forcing of the climate associated with increasing the atmospheric CO_2 content [Sabine et al., 2004]. Detailed understanding of the global carbon cycle and of the amounts and location of carbon contained in its constituents is essential to furthering knowledge of the earth system, and predicting the potential absorbtion of future anthropogenically released carbon.

The medium-term—processes relevant to $\approx 10^5$ year timescale—global carbon cycle is shown in Figure 1.1. Some of the carbon released to the atmosphere by anthropogenic activity and is absorbed by the terrestrial biosphere and the ocean. While both the terrestral biosphere and ocean are net carbon sinks, both also release large amounts of carbon to the atmosphere complicating accurate estimation of the sizes of these sinks. The greatest current uncertainty in the global carbon cycle is the size and potential evolution of the carbon sink resulting from the terrestrial biosphere, the size of which is thought to have been previously underestimated. However, the location and size of these sinks is still a subject of active research (e.g. Stephens et al. [2007] and Luyssaert et al. [2008]). The size of the ocean carbon sink is better constrained, with current estimates using various methods ranging from 1.5 ± 0.9 to 2.4 ± 0.5 Pg C y^{-1}, with the most recent being 2.2 ± 0.3 Pg C y^{-1}[Gruber et al., 2009]. Further constraint of the size of the ocean carbon sink, and understanding of its possible development (e.g. Yoshikawa et al. [2008], Le Quéré et al. [2007] and Schuster and Watson [2007]), is essential to calculating the response of the carbon cycle to anthropogenic forcing.

1.3 The ocean in the carbon cycle

The ocean is the largest component of the global medium-term dynamic carbon cycle [3] containing an estimated 90% of the total carbon [Reay et al., 2007] (see also Figure 1.1). Of this ocean carbon, the vast majority (greater than 95%), resides in the intermediate and deep ocean, as dissolved inorganic and organic carbon, with the remainder in the mixed upper layer of the ocean, which is in regular contact with the atmosphere. For at least 11,000 years prior to anthropogenic industrial development, the ocean carbon reservoir was close to equilibrium with the atmosphere and terrestrial reservoir, with an estimated annual net air-sea CO_2 flux of around 0.6 Pg carbon out of the ocean, balancing the terrestrial input from riverine sources and the organic carbon buried in ocean sediments [Fasham, 2003; Mackenzie et al., 2004; Reay et al., 2007]. In this pre-anthropogenic global carbon cycle the release of geologically sequestered carbon by weathering and erosion is countered by the burial of organic matter in sediments. Anthropogenic exploitation of fossil fuels and land-use change has accelerated the release of geologically sequestered carbon by a factor of about one hundred, with the resulting increase in atmospheric CO_2 concentration perturbing the equilibrium of the carbon cycle and causing the ocean to absorb more CO_2 from the atmosphere, making the ocean a net carbon sink [Berner, 2003]. As atmospheric CO_2 concentration rises, the ocean uptake increases in response, but lags behind due to the continued increase in CO_2 emissions to the atmosphere. This dis-equilibrium between atmospheric and oceanic CO_2 is currently estimated to cause an oceanic uptake of around 2.2 Pg $\pm$ 0.5 Pg C y^{-1} [Denman et al., 2007]—roughly a third of current annual anthropogenic emissions [Sabine et al., 2004]—slowing the warming due to anthropogenic atmospheric CO_2.

Given the huge quantities of carbon contained in the ocean (see Figure 1.1) it is clear that the ocean plays the primary role in the regulation of the medium-term global carbon cycle [Murray, 2000]. Paleoclimate records such as past atmospheric CO_2 concentrations obtained from ice cores show a change in atmospheric CO_2 concentration of around 100 parts per million between glacial (180ppm CO_2) and intergalcial ($\approx$ 300ppm CO_2) periods [Jansen et al., 2007]. This change is largely attributed to oceanic processes [Peacock et al., 2006], both physical [Kurahashi-Nakamura et al., 2009] and biological [Kohfeld et al., 2005] increasing the oceanic uptake of CO_2 and hence reducing atmospheric CO_2 concentration during periods of glaciation. Emissions from athropogenic development have increased atmospheric CO_2 concentrations well-beyond any seen in the paleoclimate record for at least the last 650,000 years [Jansen et al., 2007]. Under 'business as usual' scenarios anthropogenic emissions and hence the atmospheric CO_2 concentration are projected to continue to rise, with the long term effects on the ocean's role in the global carbon cycle and on global climate still uncertain (e.g. Sabine et al. [2004]; Meehl et al. [2007]).

[3] The lithosphere is by far the largest component of the global carbon cycle but as the rate of turnover of the lithosphere is of the order of 10^8 years, it's inclusion is not relevant in the study of medium-term (order of 10^5 years) carbon cycle and it'e effect on the Earth's climate. [Murray, 2000].

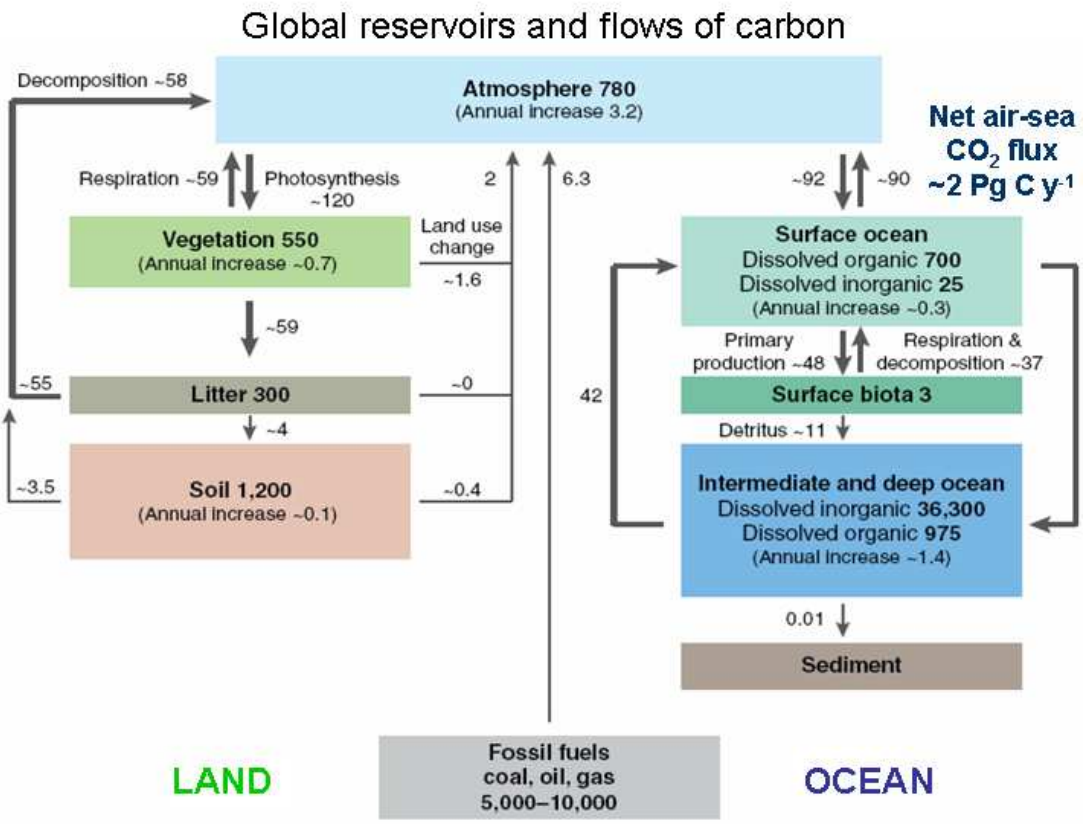

Figure 1.1: Estimated global reservoirs (in bold), and flows of carbon in Pg C yr^{-1} for the 1990's. The dynamic carbon reservoirs are the atmosphere, terrestrial biosphere (including soils) and ocean. The ocean is by far the largest carbon reservoir with the intermediate and deep ocean providing a huge medium-term (10^5 year) carbon sink. The anthropogenic exploitation of geologically sequestered carbon through the burning of fossil fuels and emissions associated with land use change are steadily increasing atmospheric CO_2 concentration. Some of this anthropogenic CO_2 is absorbed by the terrestrial biosphere and the ocean, with the remainder increasing the radiative forcing of the Earth's climate. The net carbon exchange between the atmosphere and ocean (the air-sea CO_2 flux), is estimated to be an oceanic uptake of 2.2 ± 0.4 Pg C yr^{-1} in the 1990's [Denman et al., 2007]. Adapted from Houghton [2007].

I now look at the important processes that govern the uptake of carbon by the ocean. Section 1.4 details the exchange of carbon between the atmosphere and the ocean at the air-sea interface, the interaction between the atmospheric and oceanic carbon reservoirs see in Figures 1.1. Following this, Section 1.5 explains the different physical and biological processes that transport carbon into the ocean, and the effect of the addition of anthropogenic carbon on ocean chemistry.

1.4 CO_2 transfer at the air-sea interface

The chemical interaction between the atmosphere and ocean is regulated by the transfer of gases across the air-sea interface. Atmospheric gases are exchanged between the atmosphere and ocean-surface waters with most gases in a state of near- to slight over-saturation [Bigg, 2003]. The solubility of a gas is used as a measure by which to compare the behaviour of different gases. The solubility of a gas in the ocean is defined as the the saturation concentration that would be found in the theoretical situation of the whole atmospere being composed of the gas in question. Solubility is dependant on temperature, with a high inverse dependance for heavier atmospheric gases such as CO_2. This is due to higher temperatures causing the average energy of the gas molecules to be greater, which leads to a higher exchange rate of molecules between air and water so that equilibrium (the same number of molecules leaving and entering the water) is acheived with fewer gas molecules in the liquid [Bigg, 2003]. CO_2 reacts with sea-water to form soluble ions (see Section 1.5), causing CO_2 to have a very high solubility in sea-water compared with most other principal atmospheric gases.

While the solubility describes the relative abilities of different gases to be absorbed into the ocean, as the atmosphere is a mixture of many gases the difference between the concentrations of the gas in the surface waters and atmosphere—the partial pressure—determines the actual exchange of the gas across the air-sea interface. The flux (rate of exchange) of a gas across the air-sea interface can be described in terms of the partial pressures of the gas in the atmosphere (p^{air}) and in the sea-surface waters (p^{sea}) such that

$$Flux = k(p^{sea} - p^{air}) \tag{1.1}$$

where k is the gas transfer velocity. The gas transfer velocity represents the effect on the rate of air-sea gas exchange caused by different sea and atmosphere states. In calm conditions, an unbroken sea-surface and still airmass results in a low rate of exchange as the turnover of the airmass and the renewal of gases is slow and the calm sea-surface has a relatively low surface area—no waves or bubbles. In rougher conditions, higher wind speeds result in frequent airmass mixing and renewal and the sea-surface area is increased by the presence of waves and bubbles. In conditions sufficiently rough to cause wave-breaking, the transfer velocity is dramatically increased as air bubbles are pumped into the surface waters. As the state of the airmass and sea-surface are largely dependent on wind speed, the transfer velocity k is taken as a function of wind speed, with various

parameterisations used to calculate it from wind data (e.g. Fangohr et al. [2008]; Wanninkhof and McGillis [1999]; Wanninkhof [1992]). While the gas transfer velocity k is most strongly a fuction of wind speed, other factors such as the temperature (and salinity) dependant solubility of the gas (see above) remain important so for the purpose of calculation an additional solubility term α_{sol} is added to Equation 1.1 so that k can be treated purely as a function of local wind speed—see Section 1.6.

1.5 Carbon in the ocean

Atmospheric CO_2 dissolves into the ocean surface waters with the rate determined by the CO_2 concentration of the surface waters and sea-surface conditions (see Sections 1.4 and 1.6). Most of the dissolved CO_2 reacts with seawater forming carbonic acid. Carbonic acid then ionises to form bicarbonate ions, some of which undergo a second ionisation, forming carbonate ions. These reactions are shown in Equation 1.2 below:

$$CO_2(gas) + H_2O(\rightleftharpoons H_2CO_3) \rightleftharpoons H^+ + HCO_3^- \rightleftharpoons 2H^+ + CO_3^{2-} \tag{1.2}$$

This creates a chemical buffer system that regulates the acidity and CO_2 concentration of the ocean [Sarmiento and Gruber, 2006]. These forms of carbon (including un-reacted CO_2) are collectively known as dissolved inorganic carbon (DIC). Bicarbonate accounts for approximately 90% of the total oceanic DIC content, with carbonate accounting for most of the remainder (around 8%), and CO_2 only around 1-2% [Reay et al., 2007]. While only the concentration of the unreacted CO_2 in the sea-water directly regulates the flux of further atmospheric CO_2 into the ocean, the local—constant temperature and non-carbon chemistry—proportions of different forms of dissolved carbon stay the same, so changes in the DIC concentration alter the unreacted dissolved CO_2 concentration.

Two different processes transport carbon through the ocean, changing the surface water CO_2 concentration and hence influencing the exchange of CO_2 between the ocean and atmosphere [Takahashi, 2004]. The first, known as the physical pump, results from ocean circulation physically transporting waters containing carbon away from the surface and interaction with the atmosphere (see 1.5.1 below). The second, the biological pump, arises from carbon-containing organic matter originating from photosynthetic growth sinking towards the sea-bed (see 1.5.2 below). In practice these processes are closely linked, as uptake of carbon by the ocean ecosystem influences the amount of inorganic carbon that dissolves in surface waters, while the ocean ecosystem is reliant on ocean mixing to replenish essential nutrients.

1.5.1 Physical pump

The physical pump occurs due to the solubility of CO_2 in sea-water increasing as the temperature of the sea-water decreases (see Section 1.4). Ocean circulation (thermohaline circulation) is

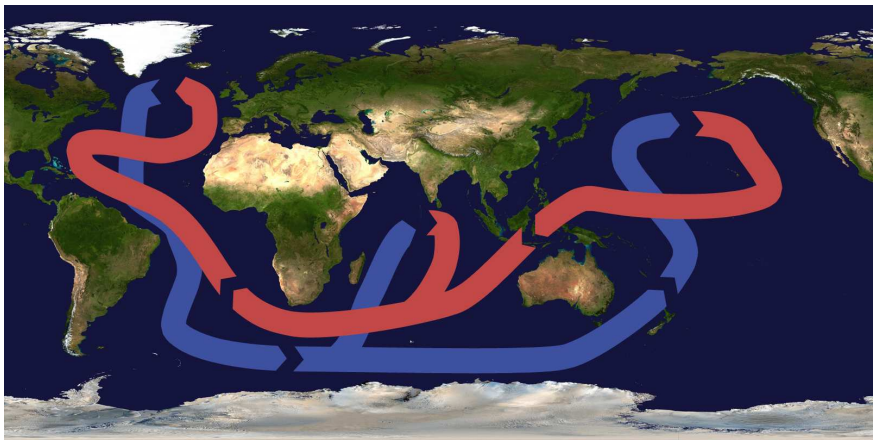

Figure 1.2: A simple schematic of the ocean 'conveyor belt' circulation. Waters warmed in the tropics are carried in surface currents (red) to high latitudes in the north Atlantic where the water cools and sinks forming cold deep ocean currents (blue) which return the water to the tropics.

driven by the interactions between solar heating of the ocean, winds, tides and salinity (e.g. Murray [2000]). Thermohaline circulation results in the so-called 'conveyor belt' circulation of ocean water mass, a simple representation of which is shown in Figure 1.2. Warm water orginating in the tropics (notably the equatorial Pacific and Indian Ocean) is transported in near-surface currents to high-latitude deep water forming regions (notably in the Labrador and Norwegian Seas in the far north Atlantic) where heat is transfered to the atmosphere and the cool water sinks returning to the tropics in cold deep ocean currents.

Atmospheric gases are well mixed, so the CO_2 concentration of the air in contact with the ocean surface is comparable across all ocean surfaces. As ocean surface-waters cool, the solubility of carbon in them increases, so more atmospheric CO_2 is absorbed—see Section 1.4. Toward the poles, this cool, dense and carbon-rich water sinks toward the sea-bed where it is transported back to lower latitudes in the deep cold currents. A complete turnover of the ocean takes around 600 years [Curry and Webster, 1999], so sea-water containing anthropogenic carbon that sinks to the deep ocean provides a sink on this timescale. When these waters resurface at lower latitudes and warm in the tropical sun, carbon is returned to the atmosphere, as less of the dissolved CO_2 is able to remain in solution.

Ocean circulation is driven by temperature, winds and salinity. Increasing global temperatures, the effect of these on winds and the input of greater quantities of fresh water from melting polar ice sheets have the potential to alter circulation patterns, generating climate feedbacks in the process [Clark et al., 2002]. Although still a subject of much debate, there is evidence that climate change is already influencing ocean circulation, and that such changes may influence the physical uptake of carbon by the oceans [Bryden et al., 2005; Le Quéré et al., 2007; Bindoff et al., 2007].

1.5.2 Biological pump

The biological pump is the result of CO_2 uptake by the ocean ecosystem being exported to sea-bed sediments by sinking. Figure 1.3 shows a schematic of the principal ocean ecosystem processes that result in the fixing of carbon and its export to the deep ocean. While the basic structure is relatively simple, each of the constituents contains many variations which have different biological and chemical behaviours, some of which remain poorly understood (see below).

Photosynthesising phytoplankton uptakes dissolved CO_2 from sea-water and converts it, using energy from sunlight, to carbohydrates required for their growth. This growth is referred to as primary production (PP), as it is the stage in which inorganic chemicals—CO_2 and nutrients—are converted to organic matter. This uptake reduces the sea-water CO_2 concentration, promoting the uptake of atmospheric CO_2 to replace it. Phytoplankton form the basis of the open ocean marine food chain and are grazed upon by higher organsims, principally zooplankton, which are grazed in turn by larger zooplankton and higher tropic levels. The by-products of this grazing, along with dead organisms arising from non-predatory (natural) mortality (collectively known as detritus) are in turn grazed upon by zooplankton and higher organisms, and broken down to more simple chemical compounds by bacteria. Through these processes much of the detritus remains in the upper ocean, but around a fifth of the total sinks away from the productive upper ocean into the deep with some reaching and adding to sea-bed sediments [Sarmiento and Gruber, 2006].

Phytoplankton are photosynthesising organisms, and are mostly single celled ranging in size from around 0.2-200μm in diameter, with different types optimised to exploit the different resources found in the oceans. Their growth is limited by all, or any of the following factors: the available sunlight (dependent on latitude and time of year, and weather conditions), temperature and the availability of key nutrients.

Phytoplankton (and their predators—namely zooplankton) inhabit the well-lit upper waters of the ocean, known as the $euphotic$ zone. This is the surface layer of the ocean where light levels are sufficient for photosynthesis to occur and is traditionally defined to be the region of the upper ocean where the available light is greater than 1% of that which is available at the ocean surface and usually extends to around 100-200m in the open ocean [Bigg, 2003]. Below this lies the dark $aphotic$ zone which extends to the sea-floor in which phytoplankton growth is prevented as photosynthesis cannot take place. The depth to which light can penetrate the ocean depends both on the amount and wavelength of light incident on the surface, and on the attenuation (intensity loss through absorbtion and scattering) of the light by the sea-water and other substances dissolved or suspended in it. Solar radiation at sea level ranges in wavelength from around 300 to 2500 nm, but phytoplankton only use radiation with wavelengths of between 400 to 700 nm (photosynthetically active radiation) for photosynthesis. As a result, concentrated phytoplankton growth close to the surface (blooms—see below) can absorb much of the available light, limiting photosynthesis deeper in the water, while less concentrated growth allows photosynthesis to take

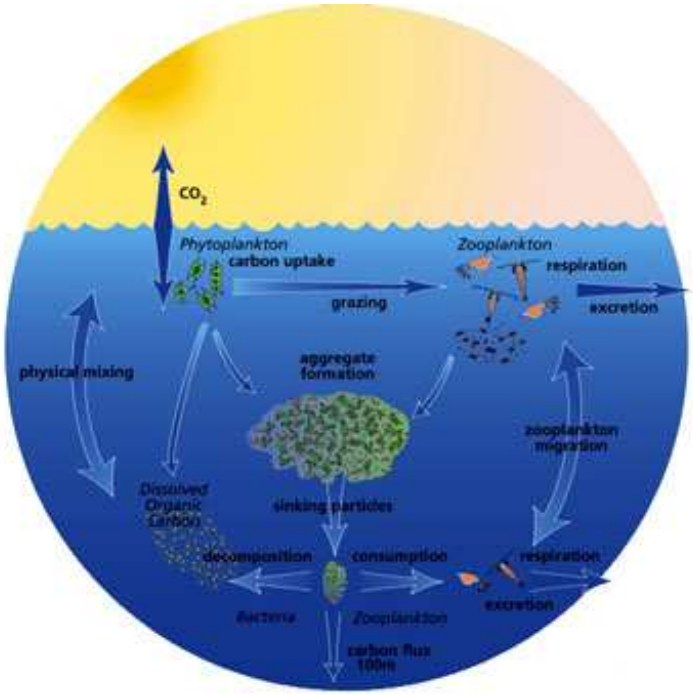

Figure 1.3: Schematic of the ocean ecosystem showing the principal biological processes that result in the eventual uptake of carbon by the ocean due to the sinking of organic detritus—the biological pump, c.f. the ocean ecosystem model schematic shown in Figure 3.1 (*JGOFS*).

place over more of the vertical water column. The calculation of light attenuation of sunlight in the ocean is discussed in Section 3.2.1.

The primary nutrient required by photosynthesising phytoplankton is nitrogen. While a few phytoplankton types are nitrogen fixers able to directly use dissolved nitrogen, most rely on more reactive nitrogen-containing compounds such as nitrate and ammonium. Phosphorous is another key nutrient, and certain types of phytoplankton—notably diatoms—require silicon to grow. In addition, other elements, notably iron, are crucial micro-nutrients. These are not required in quantity, but are neccessary for photosynthetic chemical reactions, and hence phytoplankton growth and the fixing of CO_2 [Sarmiento and Gruber, 2006; Aumont et al., 2003]. The major source of iron to the ocean is airborne dust from terrestrial sources—principally deserts [Jickells et al., 2005]. Primary production in ocean regions with little upwind landmass (notably large parts of the Southern Ocean) is iron rather than nitrogen limited, as has been demonstrated by iron fertilisation experiments such as the Southern Ocean Iron RElease Experiment (SOIREE) [Boyd and Law, 2001]. However, the potential of forcing additional CO_2 uptake by iron fertilisation has recently been argued to be hugely overestimated [Pollard et al., 2009]. Dissolved CO_2 is sufficiently abundant in surface waters to be non-limiting, particularly as removal of dissolved CO_2 by photosynthetic uptake triggers absorption from the atmosphere by altering the concentrations of the oceanic carbon buffer system discussed above.

The supply of nutrient to phytoplankton is largely determined by ocean mixing. The upper ocean is well mixed by waves and wind-stress creating a layer of water with near uniform temperature, salinity and biological organism concentrations. This layer is known as the mixed layer and usually extends over the upper 10-10^2 m of the ocean. The mixed layer plays a key role in ocean biology, as it controls the location of phytoplankton (and to some extent their predators) and the nutrient on which they depend. A deep mixed layer will carry phytoplankton to less well lit depths, limiting their growth, but will also replenish nutrient supplies by mixing deeper nutrient rich waters with the surface waters. Conversely, a shallow mixed layer keeps phytoplankton at the well lit surface, but prevents the replenishment of nutrients from deeper waters, limiting sustained growth [Bigg, 2003].

The light and nutrient limitation on phytoplankton growth leads to seasonal and spatial growth patterns. Phytoplankton grow quickly (phytoplankton have a lifetime of hours to a few days), and so respond rapidly to changes in their environment. In the northern-hemisphere spring, mid-latitude waters are well mixed from the winter storms and hence nutrient rich. As insolation and temperature increase with day-length, phytoplankton growth accelerates causing plankton blooms (containing both photosynthesising phytoplankton and grazing zooplankton), the location of which moves northwards as sun elevation increases. By early summer, the calmer weather and higher temperature mean the ocean becomes stratified, preventing nutrient replenishment from deeper waters, so the nutrient supply in the insolated surface waters becomes depleted, causing phytoplankton growth to slow. Early autumn storms mix the ocean, cycling nutrient from deeper waters triggering another period of high growth, before the decreasing day-length and lowering temperatures restrict photosynthetic activity for the winter. The southern hemisphere follows a similar cycle to that in the north, though, due primarily to iron limitation, Southern Ocean blooms are less productive than those in northern waters [Field et al., 1998; Aumont et al., 2003]. In the generally less well-mixed and less fertile subtropical gyres, any nutrient is rapidly used up so blooms are rare and there is less overall production than at the more fertile mid- and high-latitudes. In the tropics, high temperatures and consistent insolation year round mean that production is generally continuous, with blooms only occurring when tropical storms mix nutrient from deeper waters. Figure 1.4 shows the mean annual net primary production in the ocean for the years 1997-2002 derived from satellite observed ocean colour data, with the areas of highest production in nutrient rich mixed high-latitude or upwelling ocean regions.

To act as a carbon sink, the organic material resulting from phytoplankton photosynthesis must be transported away from the surface to the deep ocean. This export production occurs from the sinking of dead phytoplankton resulting from natural mortality, and from the grazing of phytoplankton by other organisms. The entire phytoplankton biomass of the ocean is estimated to be consumed every two to six days [Behrenfeld et al., 2006], principally by microscopic zooplankton, which egest organic matter, die through natural mortality and are grazed in turn

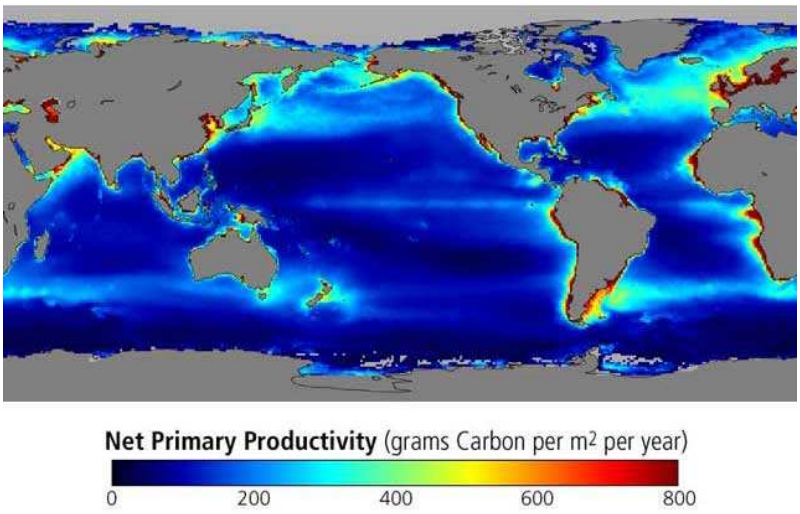

Figure 1.4: Mean annual net ocean primary productivity distribution for the years 1997-2002 derived from ocean colour data from the Sea-viewing Wide Field-of-view Sensor (SeaWiFS) satellite (*NASA*).

creating large amounts of detritus. Much of this detritus is eaten, or broken down by bacteria and recycled as nutrient in the upper ocean. Detrital material that sinks below the depth of vertical ocean mixing may eventually reach the sea-bed, where it adds to ocean sediments providing the end-point of the biological pump. A small proportion of these sediments (around 3%, Fasham [2003]) are permentantly buried, eventually forming rock and removing carbon from the medium-term (10^5 years) dynamic carbon cycle [Sarmiento and Gruber, 2006]. Due to the difficulty of collection, very little data are currently available on the amount of carbon exported to the deep ocean [Najjar et al., 2007]. Export estimates have traditionally used the f-ratio method of Eppley and Peterson [1979]. They proposed that nitrate fueled production is directly related to organic export flux, but the assumptions that underly this—principally that primary production is spatially isolated from nitrification—have recently been questioned (e.g. Martin and Pondaven [2006] and Yool [2007]). Current estimates of export vary hugely, with the Ocean Carbon-cycle Model Intercomparison Project (OCMIP), achieving results from 9-28 Pg C yr^{-1}, with model selection by data comparison narrowing this range to 11 ± 3 Pg C yr^{-1} [Najjar et al., 2007].

1.5.3 Ocean acidification

The increase in oceanic CO_2 uptake due to the increase in atmospheric CO_2 from anthropogenic sources is changing the basic chemistry of the ocean. The additional CO_2 is increasing the hydrogen ion concentration in the ocean, lowering the ocean pH which has been extremely stable for millenia [Denman et al., 2007]. Current estimates show a drop of 0.1 units of pH in surface waters compared to the pre-anthropgenic level, and projections show the process accelerating under 'business as usual' emission scenarios [Orr et al., 2005; Key et al., 2004]. This

process is slightly misleadingly referred to as ocean acidification, as the ocean is in fact slightly alkaline—the addition of anthropogenic CO_2 is gradually decreasing this alkalinity. Ocean acidification is expected to initially increase the air-sea CO_2 flux into the ocean, as the decrease in ocean pH leads to a reduction in organic carbonate formation—the precipitation of carbonate releases CO_2, increasing the pCO_2^{sea} of the surrounding water. While this process provides a temporary negative feedback to climate warming, the overall effect of decreasing ocean pH on the ocean ecosytem is still under debate (e.g. Doney et al. [2009a] and Denman et al. [2007]). Species that form calcium carbonate shells are likely to be adversely affected as their carbonate structures become vunerable to dissolution as the seawater pH decreases [Cao and Caldeira, 2008]. The sinking of this organic carbonate constitutes a significant part of the transport of organic matter to the deep ocean and hence the long-term ocean carbon sink [Loubere et al., 2007]. However, how individual species react to the decreasing pH requires further research (e.g. recent laboratory research by Iglesias-Rodriguez et al. [2008] found increased calcification by coccolithophores—a major calcifying phytoplankton group—in a CO_2 enriched enviroment, see also Doney et al. [2009a]). As on land, the ocean ecosystem is finely tuned to the chemical conditions of its environment and the decrease in oceanic pH due to anthropogenic CO_2 emissions is an additional stress on a system already adapting to changes associated with increasing temperatures.

1.6 Calculating the air-sea CO_2 flux

The exchange of CO_2 between the atmosphere and the ocean is a complex two way process with both temporal and spatial variation. An estimated 90 Pg of carbon is exchanged annually between the atmosphere and ocean [Houghton, 2007]. However, there is only a small imbalance between the fluxes in different directions. Current estimates of this net flux are an oceanic uptake of 2.2 $\pm$ 0.5 Pg of carbon per year (for the years 2000-2005) [Denman et al., 2007], and an oceanic uptake of 2.2 $\pm$ 0.3 Pg of carbon per year (for the year 1995) [Gruber et al., 2009].

The gas transfer equation is used to calculate the size of the flux according to local conditions.

$$\text{CO}_2 \text{ transfer} = k\alpha_{sol}[pCO_2^{sea} - pCO_2^{air}] \tag{1.3}$$

In the gas transfer equation, the direction of the CO_2 flux is determined by the difference between the partial concentration of CO_2 in the atmosphere (pCO_2^{air}) and in the ocean surface (pCO_2^{sea}). This difference, combined with the solubility α_{sol} (which depends on salinity and temperature), and the gas transfer velocity k—governed by wind speeds and sea-surface conditions such as wave type, bubbles and the presence of slicks—determine the size of the flux. Of these, the wind speed through the gas transfer velocity k has the greatest effect on the size of flux, with high winds (more prevalent at high latitudes) leading to much greater fluxes. As a result, the parameterisation chosen to model the relationship between wind-speed and gas transfer velocity can have a large effect on the calculated flux [Fangohr et al., 2008; Takahashi et al., 2002]. Figure

1.5 shows the mean annual air-sea CO_2 flux for 1995 as calculated from interpolated cruise and mooring data by Takahashi et al. [2002]. This clearly shows the spatial variation in the direction and size of the air-sea CO_2 flux, with warm tropical waters outgassing to the atmosphere, and cold mid- and high-latitude waters absorbing atmospheric CO_2. The greatest uptake of atmospheric CO_2 occurs in high-latitude deep-water forming regions, most notably in the north-east Atlantic [Sabine et al., 2004]. Here, surface currents sink to the deep ocean having cooled, taking huge quantities of dissolved carbon away from contact with the atmosphere.

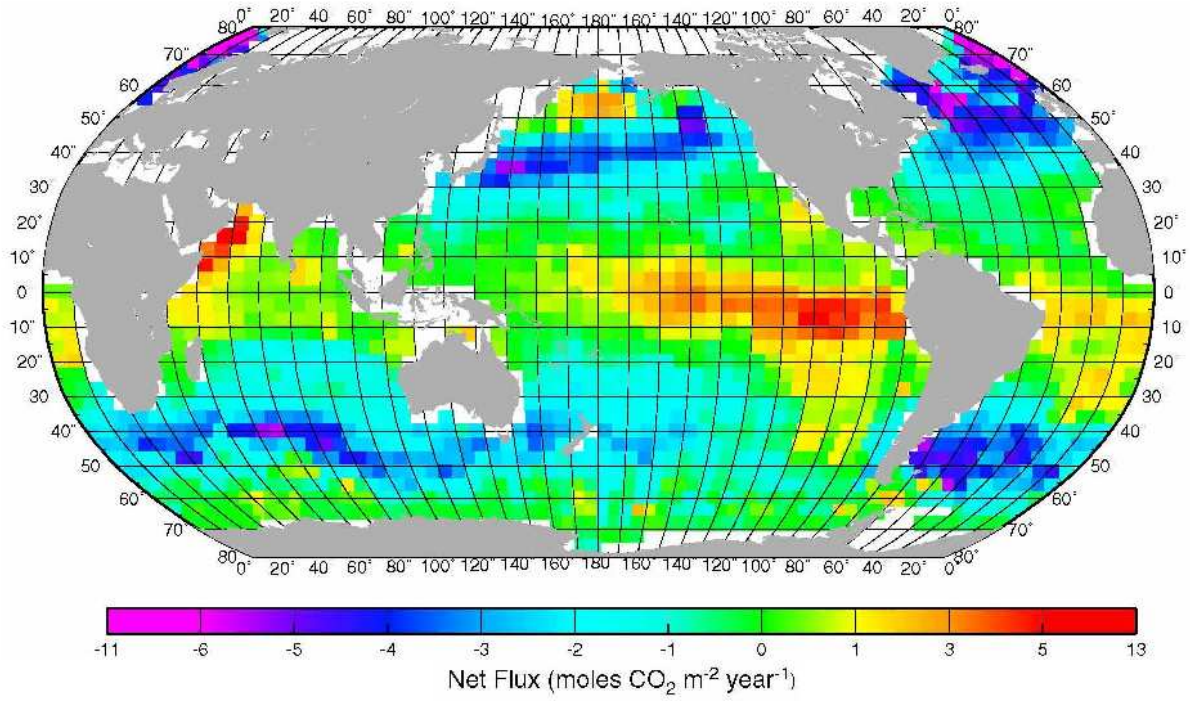

Figure 1.5: Mean annual air-sea CO_2 flux for 1995, clearly showing ingassing at high latitudes—notably in the north-east Atlantic due to CO_2 rich water sinking to the deep ocean, and outgassing in the tropics. From Takahashi et al. [2002].

1.7 Earth system modelling

Modelling plays a central role in the study of complex systems such as the Earth's climate and the processes that influence it [Randall et al., 2007; Jacobson et al., 2000]. Models allow knowledge gained from different observations to be combined, explored and assessed, and provide a viable method for predicting the future evolution of a system. However, models of complex systems are limited by the degree of detail with which we understand the system and the resources available to build and evaluate them.

Models of the Earth's climate have to capture the many different physical, chemical and biological processes and the interactions between them that control the Earth's ability to absorb and retain solar radiation. Climate models take many forms, from simple models of individual processes and components of the climate system through to hugely complex state-of-the-art global climate models (GCMs) such as the Met Office HadCM3 model [Gordon et al., 2000; Randall et al., 2007]. GCMs are constructed of many component models that describe individual processes that influence climate, which are in turn based upon our current knowledge of these processes—which can range from considerable to limited [Randall et al., 2007]. As a result, the assessment of model ability and accuracy is key to interpreting and qualifying confidence in their results [Stainforth et al., 2005; Murphy et al., 2004].

Many of the models of climate processes are parameterisations of the real world situation—a combination of equations and parameters that seek to represent to the best of our knowledge the climate influencing ability of a particular process. Equations are developed from basic principles or experimentation, and parameter values can either be observed (measured), or selected by tuning the model to reproduce an observable or known quantity [Smith and Smith, 2002]. The accuracy of a model depends on the quality of the parameterisations used—the ability of the equations and parameters to capture the relevant detail. If our knowledge of a process remains limited by constraints in observations (lack of data) and/or inaequate understanding then this limitation will be integral to the model, and the results of the model questionable to some degree. However, a model can be used to study the limitations of our knowledge by exploring the effect of adjusting the models parameterisations on the results [Smith and Smith, 2002; Saltelli et al., 2001].

The parameter values used in models are uncertain to a degree set by the quality of their measurement or of the tuning method by which they are determined [Saltelli et al., 2001]. Many of the parameters used in climate models are uncertain in value, and this uncertainty has the potential to influence the results of the model. The investigation of the effect of parameter uncertainty in climate models is therefore a key part of their assessment and development, particularly in areas of climate science such as the global carbon cycle in which our current knowledge is limited [Jones et al., 2006]. Chapter 2 details some of the methods and techniques for exploring the effects of parameter uncertainty that are used in this thesis.

1.8 Ocean carbon cycle modelling

Models have been developed to describe and study the role of the ocean in the global carbon cycle. These take the form of an ocean biogeochemical model representing the ocean ecosystem, nested within a physical ocean model, which describes the ocean mixing [Sarmiento and Gruber, 2006]. Physical ocean mixing models range in complexity from simple slab models, to 1D water columns with different levels[4], through to highly complex 3D global ocean circulation models of the vertical and lateral transport of water masses in the ocean. Similarly, ocean biogeochemical models range from simplistic representations of only the very basic components of the ecosystem, to more complex models featuring greater detail (see Section 1.8.1 below). These coupled physical-biological models use meteorological data (wind speed and temperature), atmospheric data (the atmospheric CO_2 concentration), sea-surface data (salinity, temperature and sea-surface state), and data on the availability of sunlight (latitude, time of year and cloud cover) and nutrient to the ocean ecosystem to calculate the terms in Equation 1.3, and the resulting air-sea CO_2 flux. These models can then be used in the global carbon cycle component of global climate models (GCMs) used for climate study and prediction [Randall et al., 2007].

Several studies have been and continue to be undertaken to compare and develop models of the ocean carbon cycle. The Ocean Model Intercomparison Project (OCMIP `www.ipsl.jussieu.fr/OCMIP/`) focusses on assessing the effect on the ocean carbon cycle of differences in the modelled ocean circulation [Najjar et al., 2007; Watson and Orr, 2003]. The principal conclusion of the OCMIP-2 project which compared the results of twelve different global ocean circulation models using a common biogeochemical model is the high sensitivity of ocean tracer distributions and biogeochemical fluxes to the ocean circulation regime used, with huge differences seen in for instance the calculated export (see Section 1.5.2) [Najjar et al., 2007]. Other studies such as that of Smith and Marotzke [2008] also find the representation of ocean circulation to have a large effect on the uptake and storage of carbon by the ocean. This highlights the potential impact on the cycling of ocean biogeochemical tracers and carbon of climate change forcing of large scale ocean circulation discussed in Section 1.5.1 [Bindoff et al., 2007].

The effect of climate forced changes to the global carbon cycle is one of the major uncertainties in climate prediction [Cox et al., 2000; Chuck et al., 2005; Huntingford et al., 2009]. The Coupled Carbon Cycle Model Intercomparison Project (C^4MIP `http://c4mip.lsce.ipsl.fr/`) seeks to address this by exploring the effect of carbon cycle feedbacks on global climate using GCMs that include ocean and terrestrial carbon cycle models [Friedlingstein et al., 2006]. The results of eleven coupled climate-carbon cycle models were compared with all of them indicating negative feedbacks to climate change from the global carbon cycle, but with less consensus in the size and attribution of climate change feedback to terrestrial or oceanic processes [Friedlingstein

[4] In this thesis I use the term 'level' to refer to the partitioning of the water column in a model, and 'layer' to describe the different regions of the water column e.g., the mixed layer and the euphotic layer.

et al., 2006]. To help address these issues, greater understanding of the uncertainties and limitations of the treatment of the ocean ecosystem in ocean carbon cycle models is needed (see Section 1.8.1 and Chapter 5).

1.8.1 Ocean biogeochemical models

The purpose of ocean biogeochemical models is to capture the effect of the ocean ecosystem on global chemical cycling. To model the role of the ocean ecosystem in the global carbon cycle, biogeochemical models need to calculate the effect of carbon uptake by photosynthesising phytoplankton on the ocean surface CO_2 concentration (pCO_2^{sea} in Equation 1.3), and the transport of this organic carbon to the deep ocean through the sinking of detrital material. Only the lowest trophic levels of the ocean ecosystem are represented in biogeochemical models as higher levels are assumed to have negligible effect on the transport of carbon in the ocean (an assumption that may require revision in the light of recent work on the role of fish in carbonate transport [Wilson et al., 2009]). The uptake of carbon near the sea-surface by phytoplankton growth is limited by the availability of nutrients (nitrogen is the single most important nutrient), and the availability of sunlight. The production of detrital material arises from the natural mortality of phytoplankton and grazing upon them by higher trophic levels—principally zooplankton (see Section 1.5.2).

Simple ocean biogeochemical models, such as those used in GCM's, partition the ocean ecosystem into basic components to make nutrient-phytoplankton (NP), nutrient-phytoplankton-detritus (NPD) or nutrient-phytoplankton-zooplankton-detritus (NPZD) models in which nitrogen is assumed to be the sole limiting nutrient, and the phytoplankton, zooplankton and detritus are given global characteristics [Sarmiento and Gruber, 2006]. These simple models are relatively computationally efficient and can be tuned to reproduce bulk properties like remotely estimated primary production, so are widely used in GCMs. This study uses the NPZD Hadley centre ocean Carbon Cycle model (HadOCC) of Palmer and Totterdell [2001], which is currently used in the Met Office Hadley centre Climate model 3 (HadCM3) [Gordon et al., 2000], and FAst Met Office and Universities Simulator (FAMOUS) [Smith et al., 2008] GCMs (see Chapter 3).

Recently, more complex models have been developed that attempt to represent the makeup of the ecosystem and its behaviour more precisely by subdividing the basic components into different classes with different properties. This can involve the inclusion of multiple nutrients, different sizes and types of phytoplankton and zooplankton, different types of detrital material depending on origin and the explicit inclusion of bacterial activity [Fasham, 2003; Sarmiento and Gruber, 2006].

At present, a major focus of this work is on improving the representation of the phytoplankton component by replacing it with varying numbers of different phytoplankton functional types (PFTs) [Hood et al., 2006; Le Quéré et al., 2005]. Phytoplankton functional types are groupings of phytoplankton species based on a common ecological functionality, such as the ability to fix

nitrogen or being sufficiently large to sink. Chemical behaviour is a function used to subdivide phytoplankton in models, as certain groups of phytoplankton play an important role in the global cycling of certain chemical compounds e.g., calcifiers such as coccolithophores and silicifiers such as diatoms [Sarmiento and Gruber, 2006; Hood et al., 2006]. This requires the expansion of the nutrient compartment of the model to include relevant nutrients (e.g. silicon and iron). Size is another method used to divide phytoplankton into functional groups, as small phytoplankton e.g. nanoplankton or picoplankton (0.2-20 μm diameter) form the majority of the biomass in the low nutrient open ocean where their ability to efficiently recycle organic matter is advantageous, while the larger micro-, meso- and macroplankton (20-2000 μm diameter) dominate in nutrient rich coastal and upwelling ocean regions [Sarmiento and Gruber, 2006].

The development of PFT models for biogeochemical purposes is the subject of much current debate. While these models give greater insight into the behaviour of the ecosystem in response to anthropogenic climate forcing, the present selection of functional groups is based on our arguably inadequate current knowledge of the role of the various constituents of the ocean ecosystem in chemical cycles [Hood et al., 2006; Anderson, 2005]. At present, complex ocean biogeochemical models are generally too computationally expensive for widespread inclusion in GCMs, but with advances in computing facilities, may be included in the future in attempts to further understand the effects of climate feedback on the global carbon cycle [Hood et al., 2006; Friedlingstein et al., 2006].

1.9 Thesis objectives and outline

This thesis has two principal objectives. Firstly, to identify the ocean ecosystem parameters that through uncertainty in value affect the air-sea CO_2 flux calculated by a biogeochemical model. Secondly, to explore the effect of the uncertainty in these parameters on the calculation of the air-sea CO_2 flux in a GCM.

To address the first objective I have investigated the uncertainty in the calculation of carbon fluxes that arises from the simplification of the ocean ecosystem's role in the global carbon cycle for inclusion in global climate models. An NPZD model contains around twenty parameters that control the processing of carbon through the ocean ecosystem by the key processes of photosynthetic growth, mortality, grazing, and detrital sinking. Such parameters are estimated global averages for these biological processes, many of which have poorly understood details, or high degrees of regional variation, making the values given to these parameters highly uncertain (e.g. Fasham [2003]; Fennel et al. [2001]). This parameter uncertainty has the potential to influence the accuracy of the results of the model, and the results of the global climate models in which it is used.

A sensitivity analysis is performed to identify the parameters in the HadOCC NPZD model which

due to uncertainty in value have the most effect on the calculation of the air-sea CO_2 flux. In addition, the parameters that have the greatest effect on the detrital carbon export to the deep ocean and on the amount of primary production are also identified as these are the initial, and final stages, of the ocean biological pump.

Sensitivity analysis is the study of the relationship between information given to a model and information output by the model [Saltelli et al., 2001]. Here it is used to explore the effect of parameter uncertainty on the outputs of the HadOCC model. Chapter 2 discusses the application and techniques of sensitivity analysis detailing some of the many different design, sampling and analysis methods, with particular focus on those used in this thesis. In Chapter 3, the focus of this work, the Hadley centre Ocean Carbon Cycle model (HadOCC) of Palmer and Totterdell [2001] is introduced by describing the model structure and equations, and detailing the parameters investigated in the sensitivity analysis. To perform the sensitivity analysis, HadOCC is coupled with the General Ocean Turbulence Model (GOTM) [Burchard et al., 1999] to give a fast running, flexible 1D model known as HadOCC-GOTM [Kettle and Merchant, 2008]. This is also dicussed in Chapter 3.

Chapter 4 describes the application and results of a sensitivity analysis of the HadOCC-GOTM model at four different locations: 0°N, 15°N, 30°N and 45°N along the 30°W meridian. The literature is used to establish the uncertainty in the value of the HadOCC parameters. This information is then used with the sensitivity analysis methods detailed in Chapter 2 to identify the HadOCC biogeochemical parameters that have the greatest effect on the calculation of the annual net air-sea CO_2 flux, the annual deep carbon export, and the primary production.

The second objective is to use these results to study the effect of the uncertainty of the most important parameters on the global air-sea CO_2 flux calculated in a GCM. To do this, in Chapter 5 the values of the three ocean biogeochemical parameters found in Chapter 4 to have the greatest influence on the calculation of the air-sea CO_2 flux are perturbed in the FAst Met Office UK Universities Simulator (FAMOUS) GCM [Smith et al., 2008]. The FAMOUS GCM—introduced in Chapter 3—is a fast running derivative of the widely used HadCM3 GCM [Gordon et al., 2000] in which the HadOCC NPZD model is used to represent the ocean biogeochemistry. In addition to investigating the effect of the parameter perturbations on the calculated air-sea CO_2 flux, the effects of the perturbations on the cycling of nutrients and resulting primary production are also explored.

Chapter 6 summarises the findings of this thesis and explores the implications for the field arising from these. Lastly, possible questions and directions for the future are discussed.

Sensitivity Analysis

2.1 Overview

Computer modelling has revolutionised our approach to understanding and studying complex systems such as the Earth's climate. Computer models consist of series of equations which process initial input information to generate an output. These models provide a representation of the system under investigation, and hence, derived results are limited by the accuracy of this representation. The quality of the initial information is a major contributor to this limitation. Input information is limited by many factors, including lack of information or understanding and accuracy of measurement. The confidence placed in the results of a computer model depends to some extent on the confidence in the information used to drive the model. Sensitivity Analysis (SA) studies this relationship between the information that has been input to the model, and the results that are calculated from these. This chapter is largely based on Sensitivity Analysis by Saltelli et al. [2001].

The aim of SA is to understand how a model output is influenced by the accuracy of the input information. The results of a SA can then be used to focus attention on the specific input information which has greatest effect on the model output. In computer models, knowledge of which areas of input information contribute significantly to confidence in model outputs is invaluable to understanding and improving the modelling of the system. In general, all SA methods are computationally expensive to perform, requiring both large numbers of model runs and subsequent analyses, but the potential benefit of identifying the sources of uncertainty in models' outputs is considerable.

2.1.1 Use of SA in this project

The primary task of SA in earth system models is to relate the uncertainty in input parameters arising from limited measurement and understanding to the uncertainty of the model predictions. SA is performed by investigating how the model output responds to the perturbation of input parameters within the limits of their uncertainty. The sensitivity of an input parameter is a measure of the effect of perturbation of that parameter on the output of interest. High sensitvity

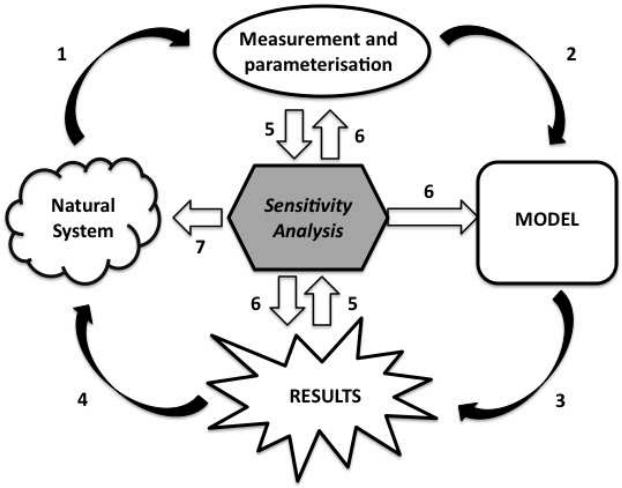

Figure 2.1: Modelling and SA procedure. 1: Natural system under investigation is measured and parameterised. 2: Model constructed from this information. 3: Model run to produce results. 4: Results used to understand natural system. 5: Information from parameterisation and results used to perform SA. 6: Results of SA interpreted for measurement and parameterisation, model and results. 7: SA results add to information used to understand natural system.

indicates that variation in the parameter has a significant effect on the calculated output, while variation in a low sensitivity parameter has a negligable effect on the output.

In this thesis, I use the methods and techniques of SA detailed in this chapter to assess the effect of ocean biogeochemical parameter uncertainty on the calculation of the sizes of important ocean carbon cycle processes in an ocean biogeochemical model—the Hadley Centre Ocean Carbon Cycle Model (HadOCC—see Chapter 3) [Palmer and Totterdell, 2001; Kettle and Merchant, 2008]. The processes investigated are the air-sea CO_2 flux, the export of organic detritus to the deep ocean and ocean primary production (see Sections 1.3 and 1.5). Each of these processes have large seasonal variability, so the net annual quantity is used as the output by which the sensitivity of each process to parameter uncertainty is assessed. In the case of the air-sea CO_2 flux this is the annual net air-sea CO_2 flux. For export, the annual deep detrital export is defined to be the total accumulation of detritus below the maximum annual mixed layer depth, and for primary production the total annual primary production is used. This work is detailed fully in Chapter 4.

2.2 Types of SA

At its simplest, SA is performed using one-at-a-time (OAT) analysis, in which each parameter is varied individually while all others remain constant at a nominal value which is usually that established by observation or experiment. This method provides simple insight into the relationship between parameter and output uncertainty, but assumes that the influence of interactions between parameters are negligable. This assumption is hard to justify in complex models where parameter interactions have the potential to contribute to output uncertainty. The more complex two-at-a-time (TAT) analysis varies two parameters at once, allowing the exploration of the effect of possible interaction between them on the output. This logic can be extended to a full Global Sensitivity Analysis (GSA) in which all parameters are varied simultaneously. While considerably more complex to implement that OAT analysis, GSA provides a much more detailed insight into the influence of parameter uncertainty on model output and as such is the preferred method for analysing complex models [Saltelli et al., 2001; Smith and Smith, 2002].

2.3 Method

A SA study can be broken down into four distinct stages. First, the possible range of each parameter is identified and an appropriate probability distribution chosen. Second, a parameter value sample set is generated from this distribution to represent the possible values for the parameters being studied. Third, the model is run for each parameter set and the output recorded to create an input-output data set. Fourth, this information generated from the model runs is used to perform the sensitivity assessment by an appropriate method. There are many different methods employed in these four stages. The choice of methods can influence the eventual result of the SA, but providing the methods chosen are appropriate, the results obtained generally agree. Commonly used methods for the first three stages are discussed below. Stage four, the sensivity assessment is treated separately below.

2.3.1 Selection of ranges and probability distributions

The first step in a SA study is to decide on the range of possible values for each parameter, and the probability distribution to describe the likelihood of the parameter value being that selected. This process can be highly subjective, as the information available on a parameter can be very limited. The range and probability distribution chosen can have a significant effect on the results of the SA, so this must be considered when interpreting SA results.

The range of credible values for the parameter can be established from any available reliable sources: data, literature research and expert opinions are all valid. However, defining a range for a model parameter often proves difficult as the parameter in question can result from the

parameterisation of poorly understood and poorly constrained processes. A possible approach to this problem is to identify the theoretical bounds to the parameter (e.g. the parameter must be positive), and to use the range established from research as a 'reasonable confidence interval', typically 5th and 95th percentiles of the parameter probability distribution. This information combined with an 'open' distribution (see below) arguably provides a more robust parameter distribution to sample from than using an absolute range with fixed upper and lower bounds from the literature, as these 'bounds' often contain a degree of uncertainty.

The probability distribution chosen to represent the likelihood of the parameter having any specific value will influence the results of the SA to some degree. In the absence of specific information, a uniform distribution between the upper and lower bounds established for the parameter is often assumed. However, the use of a uniform distribution, while straightforward and possible, is often not justified. Firstly, parameter values just outside the range are excluded completely, and secondly, a uniform distribution gives the same likelihood to extreme (just inside the limits) parameter values as to more central values that are in practice usually much more likely to occur. A traditional approach to overcome this second problem is the use of triangular distribution, often using the original parameter value as the mean. However, this still requires the use of the possible range as absolute bounds, which can be hard to justify. Very large parameter ranges can be used to overcome this, but choosing the size of this 'maximum range' is highly subjective. A better approach is possibly to use an 'open' distribution (e.g. a normal distribution), with the absolute upper and lower bounds replaced by a confidence interval as described above.

2.3.2 Sampling

For OAT SA, the parameter under investigation can be given as many incremental changes in value from the assigned distribution as are relevant, or allowed for by the computing resources available for the next step. For GSA the sampling process is more complex. The parameter ranges, and corresponding probability distributions established in step one, need to be simultaneously sampled to generate sets of parameters with which to run the model in step three. The classic method is to use random sampling to create N independent sets of parameters, where each set consists of randomly selected parameter values from each parameter's probability distribution. However, random sampling does not guarantee full coverage of the parameter sample space, so a large number of parameter sets is required to compensate. In practice, the number of parameter sets N used is limited by the available computing resources for step three, so this 'brute force' approach to sampling is impractical.

A better approach is to use a Latin Hypercube sampling method based on the use of latin squares developed by McKay et al. [1979] in the late 1970's [Saltelli et al., 2001]. Latin hypercube sampling generates N sets of parameters by splitting the range of each parameter into N divisions that each contain equal probability. One value is then randomly selected from each division of

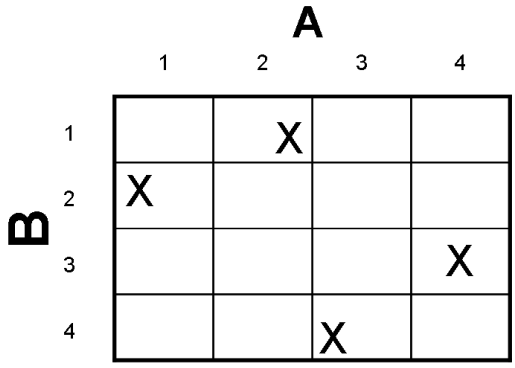

Figure 2.2: An illustration of Latin Hypercube sampling for two parameters A and B with uniform closed distributions. To generate four different parameter combinations that maximise coverage of the parameter space each parameter's range is subdivided into four sections each containing equal probability. A randomly selected value from the first of these sections for parameter A is paired with a randomly selected value from one of the four sections for parameter B—here the second section—marked by **X**. Both these sections of the parameters ranges are now covered so are not used again. The process is repeated for the second section of the range of parameter A, this time being paired with a randomly selected value from the first section of the range for parameter B. As before these sections of the ranges (second for parameter A, first for parameter B) are not sampled again. A randomly selected value from the third section of the range of parameter A is now paired with a value for parameter B taken from one of the remaining unused sections to create the third parameter combination, leaving the remaining unused sections to be sampled for the final parameter combination.

the first parameter and paired randomly, without replacement, with N values taken randomly from each equal division of the second parameters distribution. These pairs are then combined at random, without replacement with the N values for the third parameter and so on. Figure 2.2 shows a simple illustration of Latin Hypercube sampling generating four parameter sets from two parameters with uniform distributions. Unlike random sampling, this process ensures coverage of every parameter's range according to the probability distribution of that parameter, so far fewer parameter sets (typically of the order of 10 times) need to be generated to provide comparable cover to a random sampling. While N should still be as large as practical, this reduction makes a huge difference to the parameter space coverage achieved within the limits of the time and resources required in step three.

2.3.3 Model runs

The model is now run with the parameter sets generated in the previous stage. Depending on the complexity of the model, and the number of parameters under investigation, this stage often requires some degree of modification to the model code. Each value of the model output against which the sensitivity of the parameters is being tested needs to be recorded alongside the corresponding parameter set for use in the final stage.

As stated above, the number of parameter sets used is usually limited by the resources available to perform the model runs. The more complex the model, the more resources are required to perform a relevant (and with added complexity usually greater) number of runs. A recent approach to this limitation has been to employ statistical emulation techniques to generate a far greater model response than is achievable through the use of the model on its own. Here, a limited number of model runs are used to create a 'training set' of the parameters and corresponding outputs. This training set is used to emulate the model, creating a much greater coverage of the parameter and model response space. SA methods are then applied to the emulated model, which provides much more data than available from the orginal model.

2.4 Analysis

Many different techniques of varying complexity exist for determining the sensitivity of parameters from the results obtained in step three above. The chosen technique depends to a large extent on the information desired from the analysis. If the analysis is seeking to identify the parameters which have greatest influence on the output then simple techniques can often suffice. More complex methods are required to assess the influence of parameter interactions or the response of a system to extreme changes. The techniques used later in Chapter 4 are outlined below.

2.4.1 Scatter plots

One of the simplest and most intuitive methods of interpreting parameter sensivity is to use scatter plots. Scatter plots display all the values of a parameter from the parameter sets against the model output produced. For k parameters varied in the analysis this creates k different plots giving a qualitative measure of sensitivity and providing efficient intuition into the relationships between parameter and output. Features such as non-linear relationships and thresholds are immediately obvious, and it is easy to spot individual model runs that do not agree with overall trends and which may require detailed inspection or removal from the input-output data set. The ease of interpretation of scatter plots increases with the size of the suite of runs, and a judgement must be made about how many runs are sufficient to allow trends to be reliably identified. The obvious limitations are that many plots may need to be generated and studied, and scatter plots give only a qualitative description of the sensitivity of the parameters investigated.

2.4.2 Correlation

The simplest quantitative measure of parameter sensitivity is the correlation of that parameter with the output. The correlation between a parameter and the output is a number from -1 to 1 that indicates how strong the relationship between variation in the parameter is to the

variation in the output. A positive correlation means that as the value given to the parameter increases, so does the output, while a negative correlation means that the output decreases as the parameter value increases. The closer the absolute value of the correlation to 1, the stronger the relationship between the parameter and the output. A correlation of 1 or -1 means that change in the model output is completely dependent on the value given to that parameter. However, a correlation of 0 does not neccessarily mean that the parameter has no affect on the model as some methods of calculating correlation are only sensitive to certain relationships.

There are two principal ways of calculating a correlation. The first, often called the Pearson correlation, is most commonly used. This seeks to relate the values of the parameter to the corresponding value of the output and so defines the strength of the linear relationship between the parameter and the output. While this is useful, unless it is known that the relationship between the parameter and output is linear the results can be mis-interpreted. Strong non-linear correlations can have a small (or zero) Pearson correlation.

The second seeks to relate the rank (i.e. the position of the specific parameter value relative to the other values for that parameter) to the rank of the corresponding output. The use of rank instead of actual value means that the calculation identifies how well any monotomic relationship (rather than exclusively linear) describes the relationship between the parameter and output. The most commonly used rank correlations are the Spearman and the Kendall (also known as the τ rank) correlations.

A generic model consists of a number of parameters $x_1, x_2, ...x_p$, where p is the total number of parameters that are used to calculate an output y. The linear Pearson correlation r_{Pear} between the parameter x_j, where $j = 1, 2, ..., p$, and the output y, with n different values for that parameter is

$$r_{Pear} = \frac{\sum_{i=1}^{n}(x_{ij} - \bar{x_j})(y_i - \bar{y})}{[\sum_{i=1}^{n}(x_{ij} - \bar{x_j})^2]^{1/2}[\sum_{i=1}^{n}(y_i - \bar{y})^2]^{1/2}} \tag{2.1}$$

where $\bar{x_j} = \sum_i \frac{x_{ij}}{n}$ and $\bar{y} = \sum_i \frac{y_i}{n}$.

The Spearman and Kendall correlations differ in how they use the rank to calculate the degree of the relationship between a parameter and the output. The Spearman correlation r_{Spear} takes the form of the linear correlation but adapts it to use the rank of the parameter and corresponding ouput values.

$$r_{Spear} = \frac{\sum_{i=1}^{n} R(x_{ij})R(y_i) - n\left(\frac{n+1}{2}\right)^2}{\left(\sum_{i=1}^{n} R(x_{ij}^2) - n\left(\frac{n+1}{2}\right)^2\right)^{1/2}\left(\sum_{i=1}^{n} R(y_i^2) - n\left(\frac{n+1}{2}\right)^2\right)^{1/2}} \tag{2.2}$$

where $R(x_{ij})$ and $R(y_i)$ are the ranks of the j^{th} parameter and the output y.

The Kendall correlation τ calculates the difference between the number of concordant (n_c) and discordant (n_d) pairs in the rankings.

$$\tau = \frac{n_c - n_d}{\frac{1}{2}n(n-1)} \tag{2.3}$$

A concordant pair is one where $sgn(x_i - x_{i-1}) = sgn(y_i - y_{i-1})$ while a discordant pair is where $sgn(x_i - x_{i-1}) = -sgn(y_i - y_{i-1})$ where sgn is the sign function defined as

$$\textit{sgn}\ x = \begin{cases} -1 & : \quad x < 0 \\ 0 & : \quad x = 0 \\ 1 & : \quad x > 0 \end{cases} \tag{2.4}$$

Although the calculations of these rank based correlations differ, in most cases the results are usually comparable, though the Kendall correlation is arguably the more robust of the two.

2.4.3 Regression analysis

More complex methods of SA are based on regression analysis. Starting from a fit that uses all the parameters to calculate the output, the aim is to regress the number of parameters needed while maintaining calculation of the output to within a reasonable degree, as assessed by an appropriate measure (see below) [Grafen and Hails, 2002]. A linear fit involving j parameters takes the form

$$y_i = c_0 + \sum_j c_j x_{ij} + \epsilon_i \tag{2.5}$$

where each output value y_i is equal to the intercept c_0 plus each parameter x_j multiplied by a constant c_j and a residual ϵ_i (the error of the fit). The c_j are known as the regression coefficients and are commonly calculated by the method of least-squares. The better the fit the smaller the quantity known as the residual sum of squares (RSS)

$$RSS = \sum_{i=1,j=1}^{n} (y_i - (c_0 + c_j x_i))^2 \tag{2.6}$$

which is the difference between the output of the model, and the output given by the regression fit (the sum of squares of estimates of ϵ_i). The primary question in regression analysis is how to assess the accuracy of the regression model. Three regression fit tests are discussed below. The method by which parameters are removed from regression fits is also discussed. In practice, despite their differences these methods usually give very similar results when applied to the same model.

2.4.3.1 R^2—the coefficient of determination

The most commonly used measure of the accuracy of a regression fit is the coefficient of determination R^2, which calculates the fraction of the output variance that is explained by the regression model (e.g. Grafen and Hails [2002]).

$$R^2 = \frac{\sum_{i=1}^{n}(\hat{y}_i - \bar{y})^2}{\sum_{i=1}^{n}(y_i - \bar{y})^2} \tag{2.7}$$

where $\hat{y}_i$ is the estimate of y_i given by the regression fit. The closer the value of R^2 to 1 the better the fit according to this method of assesment. However, as the regression coefficients are often determined by least-squares (which form part of the denominator of the above equation) increasing the number of parameters used in the fit increases the R^2. As the object of regression in SA is to reduce the number of parameters used so as to identify the most important, this limits the usefulness of R^2.

The adjusted R^2 is defined by

$$R^2_{adj} = 1 - \left((1 - R^2)\frac{n-1}{n-k-1}\right) \tag{2.8}$$

where n is the size of the output data set and k the number of parameters used in the regression is a measure that penalises the R^2 fit for the number of parameters used. The adjusted R^2 will always be less than R^2, but in the case of SA work where n is often much greater than k, the values of R^2 and the adjusted R^2 are often comparable as for a small k and a large n

$$\frac{n-1}{n-k-1} \to 1 \tag{2.9}$$

For this reason, measures of R^2 are maybe not ideal for assessing regression fits in SA, as the addition of another parameter will usually increase both R^2, and the adjusted R^2, even if the resulting improvement in the fit is very slight. Measures of fit that penalise the number of parameters more heavily (such as the two described below) are better suited to use in SA work.

2.4.3.2 Akaike information criterion

The Akaike information criterion (AIC) is a measure frequently used to select regression models [Burnham and Anderson, 2002]. As a model selection tool it gives a relative measure of the amount of information lost between different fits used to describe a relationship between input information and output data. It takes the form

$$AIC = lnV + \frac{2k}{n} \tag{2.10}$$

where V is the loss function (a measure of the information lost in the fit), k is the number of parameters used in the fit, and n the size of the output data set as before. Under the assumption that the model errors are normally distributed and independent, the AIC can be written as

$$AIC = 2k + n\left[\ln\left(\frac{2\pi RSS}{n}\right) + 1\right] \tag{2.11}$$

where RSS is the residual sum of squares as detailed in Equation 2.6. The lower the AIC (more often than not negative), the better the fit. As the AIC is a relative measure used to compare different fits, all the constant terms in Equation 2.11 can be factored out so that

$$AIC = n\left[\ln\frac{RSS}{n}\right] + 2k \tag{2.12}$$

As k must be positive, increasing the number of parameters increases (worsens) the AIC unless the RSS is sufficiently reduced by the additional parameters. This balance between the number of parameters required and the accuracy of the fit penalises the addition of more parameters much more strongly that the adjusted R^2 (cf. Equation 2.8 and Equation 2.12). This makes the AIC arguably more appropriate for use in assessing regression fits for SA, as AIC assessed best-fits will use only parameters whose inclusion significantly reduces the error of the fit—the most sensitive parameters.

2.4.3.3 Bayesian information criterion

The Bayesian information criterion (BIC), is another model selection tool frequently used to compare regressions [Burnham and Anderson, 2002; Carlin and Louis, 2008; Saltelli et al., 2001]. It is defined to be

$$BIC = -2\ln L + k\ln(n) \tag{2.13}$$

where L is the maximised value of the likelihood function (the probability of the parameter given the output), n is the size of the output set, and k the number of regressors (parameters plus the intercept) used. As with the AIC above, under the assumption that the model errors are normally distributed and independent the BIC can be expressed in terms of the RSS as

$$BIC = n\ln\left(\frac{RSS}{n}\right) + k\ln(n). \tag{2.14}$$

In this form it is easy to see that the BIC of a regression increases with both an increase in the RSS and in the number of parameters used (k). As in the calculation of the AIC, this represents a balance between the accuracy of the regression (the RSS), and the number of regressors (parameters), needed to achieve this accuracy. The lowest (again often negative) BIC identifies the best balance between description and complexity in competing regression fits. Comparing the BIC (Equation 2.14), with the AIC (Equation 2.12), it can be seen that provided the size of the output set $n > e^2 \approx 7$—almost always the case, the second term of the BIC

will be greater than that of the AIC ($k\ln(n) > 2k$). Thus the BIC penalises more strongly against the number of parameters used in the regression. This stronger penalising of the number of parameters used makes the BIC arguably even more appropriate for use in regression for SA.

2.4.3.4 Stepwise regression

Regression analysis requires the removal or addition of parameters to a fit to improve the quality of the fit as assessed by one of the methods above. For small numbers of parameters it is possible to explore the possible combinations by hand, but for the larger numbers likely to be involved in the SA of more complex models this is impractical. A commonly used approach is to perform a stepwise regression to automate the parameter selection procedure. There are three types of stepwise regression—forward selection, backward elimination and combined methods. Forward selection consists of starting with no parameters in the fit, then adding one by one and including if the addition of the parameter improves the fit according to the chosen assessment method. Backward elimination starts with a regression consisting of all parameters and eliminates them one by one, only keeping the parameters that when eliminated cause the quality of the fit to decrease. Combined methods test the effect of the inclusion or exclusion of each parameter in turn. While stepwise regression is an efficient approach to identifying the important parameters, the arguably arbitrary order in which parameters are listed can influence the result. This arises because as a parameter is included or excluded from the fit, the importance of the other parameters in the fit changes. As the parameters are added/removed in a predetermined order the signal of an important parameter can be swamped by the inclusion of other parameters. This is most easily seen in the case of forward selection where the first parameter used will almost certainly improve the fit (and hence be kept), regardless of its actual importance. Combined methods reduce the effect of ordering but do not eliminate it completely.

2.4.3.5 All-subsets regression

All-subsets regression improves on stepwise methods by forming every possible combination of parameters, from each individually to all k parameters giving $\sum_{p=1}^{k} \frac{k!}{p!(k-p)!}$ different regression fits. Each of these regression fits is assessed by an appropriate method to identify the fit (or fits) that perform best, and hence contain the most important parameters. By calculating all possible combinations all-subsets regression is not influenced by the order of the parameters, but does take considerably more effort to perform. All-subset regression also clearly orders the parameters in significance order by inclusion or exclusion from the fit. Once all possible subsets have been tested, the best subset of each size (one subset of each size from 1 to k) allows easy reading off of the parameters in order of importance, as well as showing how many of the parameters are crucial in the calculation of the output.

2.4.3.6 Non-linear regression

Regression fits are not limited to exclusively linear combinations of parameters. Second and higher order terms of existing parameters can be introduced as additional parameters, as can interaction terms between parameters. The addition of higher order and interaction terms to regression fits can improve their performance, though the addition of terms greater than second order and three-way or greater interactions needs careful justification. However, including just second order terms doubles the number of possible terms in the fit and including all possible two-way interactions adds $(k-1)!$ terms drastically increasing the complexity of selection in the regression and the resources required. For SA work, a practical approach is to start with linear fits to establish the important parameters and then to explore if the inclusion of second order or interaction terms involving these parameters gives any further insight.

2.4.4 SA packages: GEM-SA

Various computer packages have been developed to perform sensitivity analyses. In this work, the SA package Gaussian Emulation Machine for Sensitivity Analysis (GEM-SA) `www.ctcd.group.shef.ac.uk/gem.html`, developed at the Centre for Terrestrial Carbon Dynamics (CTCD), is used to provide comparison with the traditional methods described above. A common problem with performing SA is the computational expense of performing large numbers of model runs to generate the input-output data set for study. To reduce this computational cost, GEM-SA uses an input-output data set as a training set to build an emulation of the relationship between the inputs and output in the model, allowing the input-output set, and the corresponding cost of generation, to be smaller. This emulation is a statistical approximation to the actual model, which allows the SA to use information from the emulated regions between the points defined by the processed input-output data, as well as the points themselves.

To emulate the relationship between the inputs and the output, GEM-SA interpolates between the points in the training set using a Gaussian process. At each of the points in the training set the emulator gives the same result as that found in the training set—at these points the uncertainty in the fit of the emulator is zero. Between these training set points the emulator gives a ‘best guess’ to the true value of the output that would have been calculated if the corresponding parameter value had been explicity used, with the uncertainty of this ‘best guess’ as a normal distribution. This means that uncertainty in the goodness of fit of the emulator increases as the emulated parameter moves further away from the points of the training set as shown in Figure 2.3. In practice, provided the relationship between the parameter and output is smooth, and a suitably sized training set is used, the emulated data is virtually indistinguishable from genuine data.

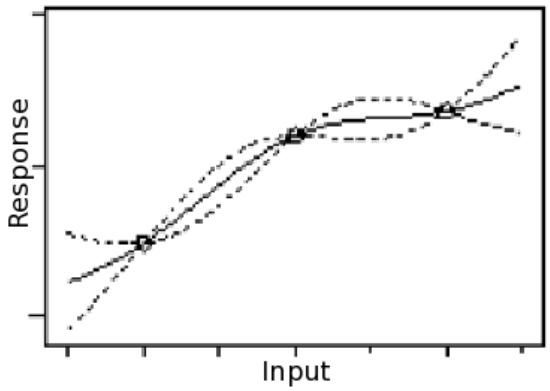

Figure 2.3: Emulation of a function from three data points. Solid line is the mean of the emulated function, while dotted lines show the confidence interval of the emulated function—zero at a data point in the training set, and increasing with the distance from a data point. Where there is no further training data to constrain the function, the confidence interval diverges rapidly, so the training data must adequately cover the full parameter space.

2.4.4.1 Using GEM-SA

The selection of appropriate parameter ranges for use in GEM-SA is carried out as for traditional SA methods, as described in Section 2.3.1. These ranges are input to GEM-SA, which uses them to design the training set for the emulator. Uniform distributions between the specified limits of each parameter are sampled using a latin hypercube method (ensuring full coverage of the parameter space—see Section 2.3.2) to produce the training set. This GEM-SA generated set of parameter values are processed through the model as before (Section 2.3.3), and the resulting output returned to GEM-SA. The model output is combined with the parameter sets and used to build the emulation of the model. SA is then carried out on the emulated model.

GEM-SA calculates the contribution of the variance in the value of each parameter to the variance in the output in two ways. Firstly, the individual contribution of each parameter to output variance is calculated. Secondly, the total effect of each parameter is calculated. This is the individual contribution and the contribution arising from any interaction between the parameters. A large total effect relative to the individual effect indicates that interactions involving this parameter are important. GEM-SA allows the calculation of the effect of interaction between any two parameters to assess this.

HadOCC ocean carbon cycle and FAMOUS global climate models

3.1 Overview

The Hadley centre Ocean Carbon Cycle (HadOCC) model [Palmer and Totterdell, 2001], is a Nutrient-Phytoplankton-Zooplankton-Detritus biogeochemical model used by the UK Met office in GCMs to represent the role of ocean biogeochemistry in the global carbon cycle. To efficiently perform a sensitivity analysis on HadOCC it is coupled with the General Ocean Turbulence Model (GOTM) [Burchard et al., 1999]. This gives a fast and flexible 1-D ocean biogeochemical model appropriate for the large number of runs required for sensitivity analysis, hereafter known as HadOCC-GOTM [Kettle and Merchant, 2008]. The FAst Met Office Univerities Simulator (FAMOUS) model [Smith et al., 2008] is a lower resolution version of the Hadley centre Climate Model 3 (HadCM3) GCM [Gordon et al., 2000], in which HadOCC is used to simulate the influence of ocean biogeochemistry on the global carbon cycle. This chapter describes HadOCC and the biological parameters studied in this thesis, and gives a brief overview of HadOCC-GOTM and FAMOUS.

3.2 HadOCC

The HadOCC biogeochemical model is a simplified explicit representation of the ocean ecosystem, which simulates the movement of carbon due to ecosystem processes in the ocean. Photosynthesis by phytoplankton, and hence fixing of carbon in organic matter through their growth, is limited by the availability of sunlight and nutrient. Phytoplankton die through natural mortality and are grazed upon by zooplankton producing detritus that sinks through the water column—the biological pump (see Section 1.5.2). Some of this detritus is broken down by bacterial action and the nutrient and carbon contained is released. This nutrient is circulated by ocean mixing allowing further phytoplankton growth. The model computes the flow of nitrogen between four state variables; In-organic Nutrient, Phytoplankton, Zooplankton and Detritus (NPZD). Each state variable is a single simple representation of the many different types of that variable that exist in the ocean (e.g. different nutrients, phyto- and zooplankton species, and

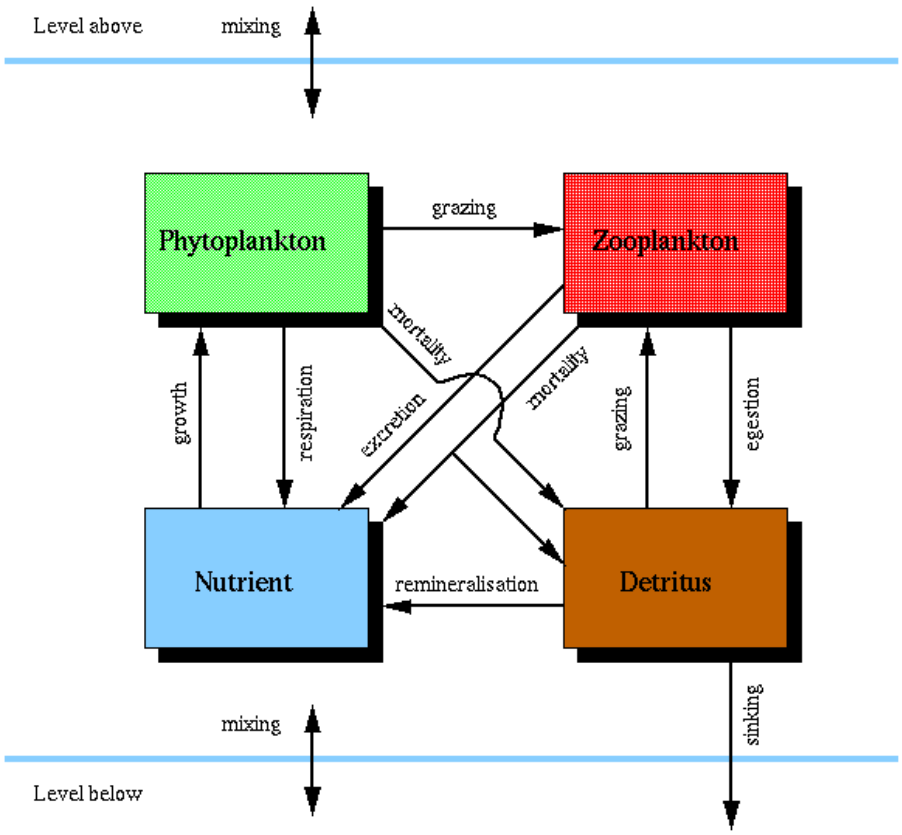

Figure 3.1: Schematic of the HadOCC biogeochemical model (c.f. Figure 1.3). The model computes the flow of nitrogen between the four state variables—nutrient, phytoplankton, zooplankton and detritus. These state variables exist at all depth levels and the concentrations of each exchange with the those of the levels above and below, as determined by the physical mixing. Only detritus moves independently of mixing, sinking at a fixed rate per day *(*from Met Office).

particle sizes and chemical makeup). Their concentration is measured in terms of their nitrogen content in mMol N m^{-3}. This nitrogen flow is then used to calculate the corresponding flow of carbon and the alkalinity. The flow of carbon has no direct effect on these processes, as dissolved inorganic carbon (DIC) is abundant throughout the water column so does not limit phytoplankton growth. Figure 3.1 shows the structure and pathways followed by nitrogen in the model. Each state variable exists at all depths, with exchange in the concentrations of the state variables between the depths controlled by the mixing regime of the physical model. As well as mixing with adjacent levels driven by the physical model, detritus sinks at a fixed rate. This simulates the final stage of the biological pump by exporting organic carbon to the ocean floor.

The change in nitrogen concentration is calculated as

$$\frac{\partial Nit}{\partial t} = \text{phys. mixing} + \text{bio. process } (Nit) \tag{3.1}$$

where physical mixing is governed by the ocean turbulence model, and the biological process

term contains the production and destruction terms for each of the state variables. The biological process equations are detailed in the following section.

3.2.1 Modelling underwater penetration of solar radiation

Calculating the amount of light available to phytoplankton for photosynthesis is the first step in modelling the ocean carbon cycle. The amount of sunlight incident on the ocean surface depends on the time of year and the amount of cloud present in the atmosphere (a term in the meteorological forcing). A proportion of this radiation is reflected from the ocean surface, while the remainder penetrates the water column with rapidly decreasing intensity according to depth. As a result the water column can be divided into two distinct layers. The upper is the light bathed $euphotic$ zone, where phytoplankton can photosynthesise and grow, which extends to approximately 100-200m below the surface. Beneath this, extending to the ocean floor, lies the dark $aphotic$ zone where there is insufficient radiation for photosynthesis.

The exact depth to which solar raditation penetrates and so is available for use in photosynthesis depends both on the wavelength of the radiation—different wavelengths penetrate to different degrees, and the absorption and scattering of this radiation by the seawater and its constituents. Photosynthesis uses only the wavelengths of sunlight between 400-700nm. This is known as Photosynthetically Active Radiation (PAR), and is taken to be a fixed fraction (0.46 [Baker and Frouin, 1987]) of the total solar radiation available at the ocean surface in μ mol quanta $\mathrm{m}^{-2}\mathrm{s}^{-1}$ (1 μ mol quanta = 0.2178 Wm^{-2}). The PAR available I at depth z is given by

$$I(z,t) = I(0,t)\int_{\lambda=400}^{700} \omega(\lambda)\exp\left(-\int_{z}^{0} K_d(\lambda,z)dz\right)d\lambda \tag{3.2}$$

where the first integral sums the light field over wavelengths and the second the attenuation coefficient K_d over depth. $K_d$is the attenuation coefficient for solar radiation in the the ocean which is a combination of K_w—the attenuation by seawater and attenuation by chlorophyll pigments such that

$$K_d(\lambda) = K_w(\lambda) + \chi(\lambda)Chl^{\gamma(\lambda)} \tag{3.3}$$

where χ and γ are empirical constants as functions of wavelength [Morel, 1988; Morel and Maritorena, 2001].

To improve computational efficiency HadOCC uses the Anderson [1993] non-spectral method for estimating K_d and hence calculating I. The water column is divided into three levels (0-5m, 5-23m and 23m-ocean bed) and K_d is estimated for each of these levels as a function of the square root of the chlorophyll concentration in that level. The chlorophyll concentration in each level is

$$K_{d,A,i} = b_{0,i} + b_{1,i}c + b_{2,i}c^2 + b_{3,i}c^3 + b_{4,i}c^5 + b_{5,i}c^5 \tag{3.4}$$

where $c = \sqrt{\text{Chl mg m}^3}$ and i is the number (1-3) of the level. The coefficients b for each level are given in Table 4 of Anderson [1993]. $K_{d,A}$ is computed from the chlorophyll concentration for each depth level of the physical ocean model (see Section 3.3 below) according to the level of Anderson [1993] in which it lies (the physical ocean model levels are not the same as those of Anderson [1993]). The non-spectral PAR is then calculated using

$$I_{(z,t)} = I(0,t) \exp\left(-\int_z^0 K_{d,A}(z)dz\right). \tag{3.5}$$

3.2.2 Phytoplankton

Phytoplankton concentration P in (mMol N m^{-3}) is

$$\left.\frac{\partial P}{\partial t}\right|_{bio} = I_{lim} N_{lim} P - M_P - H_P - \eta P \tag{3.6}$$

where the first term represents the light and nutrient limited growth of the phytoplankton, M_P the loss due to natural phytoplankton mortality, H_p the loss due to grazing by the zooplankton compartment (see Section 3.2.3), and ηP the loss due to respiration.

The light limitation I_{lim} is estimated using the daily-averaged version of the spectrally-averaged parameterisation by Anderson [1993] such that

$$I_{lim} = 1 - \exp\left(\frac{-\alpha_{max}}{P^s_{max}\Theta N_{lim}}\alpha^{\#} I\right) \tag{3.7}$$

where $\alpha_{max} = 2.602\alpha$ (α is the initial slope of the photosynthesis-irradiance curve—see Section 3.2.8 and Figure 3.2 below). I is the photosynthetically active radiation (now in W m^{-2}) as discussed in Section 3.2.1 above, and $\alpha^{\#}$ is derived empirically as a polynomial based on the square root of the chlorophyll concentration using the method of Anderson [1993] as detailed above in Section 3.2.1.

N_{lim} is the limitation on growth by the availability of nutrient given by

$$N_{lim} = \frac{N}{N + K_{nit}}. \tag{3.8}$$

where N is the available nutrient (see below), and K_{nit} the nutrient half saturation constant in mMol N m^{-3} (see Section 3.2.8).

Viral infection is assumed to be responsible for all phytoplankton natural mortality so that the specific rate increases or decreases with the population. M_P is the phytoplankton mortality, where $M_P = m_0 P^2$. However, in the instance that the concentration of phytoplankton falls below $P \leq 0.01$ mmol^{-3}, the phytoplankton specific mortality rate m_0 is set to zero to prevent extinction of the population. Dead phytoplankton is partitioned as follows: as much as possible, as limited by the different carbon to nitrogen ratio (see Section 3.2.3) flows into the detrital

compartment, while any remaining nitrate is returned to the nutrient compartment. The specific rate of phytoplankton respiration η is constant for all concentrations.

3.2.3 Zooplankton

Zooplankton concentration Z in mMol N m^{-3} is

$$\left.\frac{\partial Z}{\partial t}\right|_{bio} = F_{ingest}(\beta_P H_P + \beta_D H_D) - M_Z \tag{3.9}$$

where the first term encompasses the assimilation of grazed phytoplankton and detritus by zooplankton and the second term all zooplankton losses due to natural mortality, predation by other marine organisms, respiration and excretion.

Zooplankton graze on both phytoplankton and detritus and are assumed to be non-discriminatory in their feeding, ingesting phytoplankton and detritus in the proportions in which they are available. This proportion must be considered in terms of biomass as the nitrogen content per unit biomass in zooplankton, phytoplankton and detritus is different. This is calculated by use of the carbon to nitrogen ratio of phytoplankton $\Theta_P = 6.625$ (the Redfield ratio), zooplankton $\Theta_Z = 5.625$, and of detritus $\Theta_D = 7.5$. The factors B_P, B_Z and B_D where

$$B_P = \frac{14.01 + 12.01\Theta_P}{14.01 + 12.01\Theta_{Red}} = 1 \tag{3.10}$$

$$B_Z = \frac{14.01 + 12.01\Theta_Z}{14.01 + 12.01\Theta_{Red}} \tag{3.11}$$

$$B_D = \frac{14.01 + 12.01\Theta_D}{14.01 + 12.01\Theta_{Red}} \tag{3.12}$$

where Θ_{Red} is the Redfield ratio of 6.625, are used to convert nitrogen content to biomass.

If h is the grazing rate per unit food concentration, then the ingestion by zooplankton and corresponding losses to phytoplankton and detritus are $H_P = hP$ and $H_D = hD$ respectively, where

$$h = \frac{B_Z Z}{F_{tot}} g_{max} \frac{F^2}{F^2 + K_F^2} \tag{3.13}$$

in which $F = \max(0, F_{tot} - F_{th})$, $F_{tot} = B_P P + B_D D$ with B_P and B_D as described above, the grazing threshold $F_{th} = 0.1$, g_{max} is the maximum zooplankton grazing rate, and K_F is the half saturation constant for grazing.

The zooplankton mortality is given by

$$M_Z = \mu_1 Z + \mu_2 Z^2 \tag{3.14}$$

where μ_1 are the linear and μ_2 the quadratic zooplankton mortality rates—see Section 3.2.8.

3.2.4 Detritus

Detritus contains all dead organic material: both phytoplankton and zooplankton, and egested faecal pellets. At a given depth level, the production terms encompasses the contribution from phytoplankton mortality, zooplankton mortality and zooplankton egestion, while the destruction term arises from grazing by zooplankton, remineralisation and the sinking of detritus to the depth level below. Detritus sinks at a daily rate through the water column—the detrital flux from the depth level above is $v_s D_{above}$, and the flux to the level below is $v_s D$, where v_s is the daily sinking rate, and D_{above} and D the concentrations of the adjacent depth levels. The detritus concentration D in a depth level in mMol N m^{-3} is

$$\begin{aligned} \left.\frac{\partial D}{\partial t}\right|_{bio} &= \frac{\Theta_P}{\Theta_D}(1-F_{nmp})M_P + \frac{\Theta_Z}{\Theta_D}(1-F_{zmort})M_Z \\ &+ \frac{\Theta_P}{\Theta_D}a_{PD}H_P + (a_{DD}-1)H_D - \lambda D \end{aligned} \tag{3.15}$$

where $\Theta_P = 6.625$, $\Theta_Z = 5.625$ and $\Theta_D = 7.5$ are the carbon:nitrogen ratios of phytoplankton, zooplankton and detritus as before (see Section 3.2.3). $a_{PD} = (1-F_{messy})(1-F_{ingest})+(1-\beta_P)F_{ingest}$, $a_{DD} = (1-F_{messy})(1-F_{ingest})+(1-\beta_D)F_{ingest}$ and $\lambda = Rm_{shall}$ above 100m and $\lambda = Rm_{deep}$ below 100m. Detritus cannot sink out of the water column, so detritus that accumulates at the bottom of the water column is spread equally over the bottom three levels.

3.2.5 Nutrient

Nutrient in the ocean is depleted in areas of high productivity by phytoplankton growth, but replenished by upwelling of nutrient rich water from beneath the euphotic zone. The state equation for nutrient N in mMol N m^{-3} is

$$\begin{aligned} \left.\frac{\partial N}{\partial t}\right|_{bio} &= \left\{F_{nmp} + \left(1-\frac{\Theta_P}{\Theta_D}\right)(1-F_{nmp})\right\}M_P + \eta P \\ &+ \left\{F_{zmort} + \left(1-\frac{\Theta_Z}{\Theta_D}\right)(1-F_{zmort})\right\}M_Z \\ &+ F_{messy}(1-F_{ingest})(H_P+H_D) \\ &+ \left(1-\frac{\Theta_P}{\Theta_D}\right)a_{PD}H_P \\ &+ \lambda D - I_{lim}N_{lim}P \end{aligned} \tag{3.16}$$

where the terms are (in order), the contributions from phytoplankton mortality and phytoplankton

respiration (first line), zooplankton mortality (second line), grazing byproducts (third and fourth lines) and detrital remineralisation (first term of fifth line). The final term (second term of fifth line), is the nutrient loss due to phytoplankton growth (see Section 3.2.2).

3.2.6 Dissolved inorganic carbon

Dissolved inorganic carbon (DIC) (mMol m^{-3}), is assumed to have no direct effect on the biological system as it is sufficiently abundant to never limit the growth of phytoplankton. However, the flow of carbon in the ocean ecosystem is of primary interest as it constitutes a major component of the ocean carbon sink. This effect is described in HadOCC by

$$\begin{aligned}\frac{\partial C}{\partial t} &= \Theta_P F_{nmp} M_P + \Theta_P \eta P + \Theta_Z F_{zmort} \\ &+ F_{messy}(1 - F_{ingest})(\Theta_P H_P + \Theta_D H_D) \\ &+ F_{ingest}\{(\Theta_P - \Theta_Z)\beta_P H_P + (\Theta_D - \Theta_Z)\beta_D H_D\} \\ &+ \Theta_D \lambda D - (1 - \Upsilon_c)\Theta_P I_{lim} N_{lim} P\end{aligned} \tag{3.17}$$

where the terms are (in order), the contributions from phytoplankton mortality, phytoplankton respiration and zooplankton mortality (first line), grazing byproducts (second and third lines), remineralisation and the uptake of DIC by phytoplankton growth (fourth line)—modified by the rain ratio Υ_c to account for carbonate formation (see Section 3.2.8).

3.2.7 Alkalinity

The uptake of DIC and nutrients from seawater by the ocean ecosystem also affects the alkalinity of the water. As with the DIC above, the alkalinity is assumed to have no direct effect on the operation of the ecosystem—a possible limitation in long term climate forecasting in the light of ocean acidification—see Section 1.5.3. The alkalinity, A in mMol m^{-3} is determined by

$$\frac{\partial A}{\partial t} = -2\Upsilon_c \Theta_P I_{lim} N_{lim} P - \frac{\partial N}{\partial t} \tag{3.18}$$

where the terms are the change due to carbonate production (see Section 3.2.8), and the change in nutrient concentration.

3.2.8 HadOCC parameters

Table 3.1 lists the HadOCC parameters investigated in this thesis with their current value in HadOCC-GOTM. Each parameter is detailed individually below.

Table 3.1: HadOCC parameters, units, description and current values in HadOCC-GOTM. A fuller description of each parameter is given in Section 3.2.8.

Parameter No.	Parameter	Units	Description	HadOCC value
1	K_{nit}	mMolNm^{-3}	Half saturation constant for nutrient limitation	0.1
2	P^s_{max}	d^{-1}	Chl-specific maximum rate of photosynthesis	1.5
3	α	mgC mg chl^{-1} h^{-1} (Wm^{-2})$^{-1}$	Initial gradient of P-I curve	0.02
4	η	d^{-1}	Phyto.-specific respiration rate	0.05
5	m_0	d^{-1} (mMol N m^{-3})$^{-1}$	Natural phyto. mortality rate	0.05
6	μ_1	d^{-1}	Density independent zoo. mortality rate	0.05
7	μ_2	d^{-1} (mMol N m^{-3})$^{-1}$	Density dependent zoo. mortality rate	0.3
8	K_F	d^{-1}	Zoo. half stauration constant for grazing	0.5
9	g_{max}	d^{-1}	Maximum grazing rate of zoo.	0.8
10	β_P	-	Assimilation efficiency of zoo. on phyto.	0.9
11	β_D	-	Assimilation efficiency of zoo. on detritus	0.65
12	F_{ingest}	-	Food fraction injested by zoo.	0.77
13	F_{messy}	-	Contribution of messy feeding by zoo. to labile N and C	0.1
14	F_{nmp}	-	Contribution of phyto. mortality to labile N and C	0.01
15	F_{zmort}	-	Contribution of zoo. mortality to labile N and C	0.67
16	v_s	m d^{-1}	Daily sinking rate of detritus	10
17	Rm_{shall}	d^{-1}	Shallow remineralisation rate	0.1
18	Rm_{deep}	m d^{-1}	Deep remineralisation rate	8.58
19	Υ_c	-	Rain ratio (carbonate formation by phyto.)	0.013
20	Θ	-	C:Chl ratio in phyto.	40

1. K_{nit}: The value of K_{nit}, the half saturation constant for nutrient limitation, controls the sensitivity of phytoplankton growth to the amount of available nutrient through the relationship

$$N_{lim} = \frac{N}{K_{nit} + N} \tag{3.19}$$

where N_{lim} is the nutrient limitation factor used in the calculation of phytoplankton growth and N is the level of available nutrient. At low values of K_{nit}, phytoplankton growth is not nutrient limited unless the concentration of nutrient is very low. Conversely, at high values of K_{nit}, phytoplankton growth is nutrient limited at higher concentrations.

2. P^s_{max}: This is the chlorophyll-specific maximum rate of photosynthesis, determining the irradiance level at which photosynthesis become light saturated and is hence the upper bound of the photosynthesis-irradiance (P-I) curve shown in Figure 3.2. This controls the rate of photosynthesis beyond which increasing irradiance has no further effect. Since the amount of light that is available to phytoplankton decreases as ocean depth increases, for a fixed value of α, P^s_{max} controls the depth at which photosynthesis becomes light limited. Low values of P^s_{max} mean that the overall rate of photosysnthesis will be lower, but the depth at which this photosynthesis becomes light limited will be greater than that for high values of P^s_{max}. At these high values, the overall photosynthetic rate is higher, but photosynthesis becomes light limited close to the surface as the amount of radiation that penetrates deeper is insufficient to reach saturation level. The photosynthetic rate below the irradiance saturation level is dependent on the value of α.

3. α: This determines how the rate of photosynthesis changes under light limited conditions and is hence the initial gradient of the P-I curve (see Figure 3.2). The relationship between α and P^s_{max} as gradient and upper bound of the P-I curve determines the growth of phytoplankton with respect to the availability of light. Most simply—for a fixed P^s_{max} and fixed amount of photosynthetically active radiation (PAR), a low α gives less photosynthesis than a higher α value.

4. η: This is the phytoplankton specific respiration rate, and determines the loss to the phytoplankton compartment due to respiration. η is a constant rate applied as ηP (see Equation 3.6). Clearly, the higher the value of η the greater the loss to the phytoplankton compartment from respiration.

5. M_p: The natural mortality of phytoplankton is assumed to occur exclusively through viral infection and is hence taken as a constant fraction M_P of the phytoplankton concentration

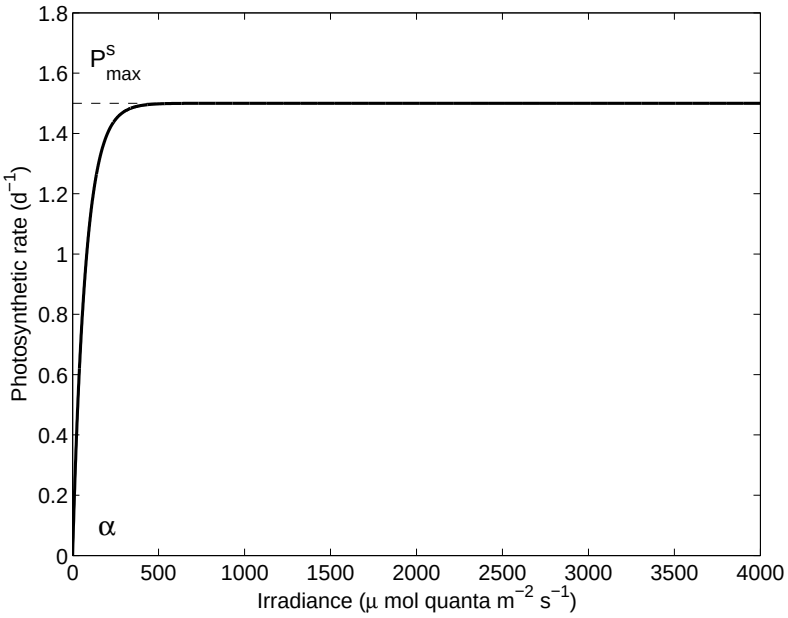

Figure 3.2: Photosynthesis-Irradiance curve. P^s_{max} is the upper bound of the curve and sets the limit on the photosynthetic rate when solar radiation is abundant. α is the initial gradiant of the curve and controls the photosynthetic rate under light limited conditions.

(see Equation 3.6). However, if the phytoplankton concentration falls below the level of $P_{min} = 0.01$ mmol m^{-3}, natural phytoplankton mortality is switched off until the concentration increases above this threshold again. This prevents the extinction of the phytoplankton population when nutrient and sunlight supplies are insufficient for growth.

6. μ_1: The zooplankton mortality M_Z is determined by two paramenters, a density independent rate μ_1, and a density-dependent rate μ_2 such that $M_Z = \mu_1 Z + \mu_2 Z^2$—the destruction term for the zooplankton compartment (see Equation 3.9). These represent the cost of natural mortality, respiration and grazing by higher organisms that are not explicit in the model. The density independent zooplankton mortality is set by the parameter parameter μ_1.

7. μ_2: The density dependent zooplankton mortality term μ_2 in the destruction term for the zooplankton compartment ($M_Z = \mu_1 Z + \mu_2 Z^2$ in Equation 3.9) is present to implicitly represent the fact that zooplankton grazers (not included in the model) will favour areas of high zooplankton concentration to feed. This arrangement also means that when the concentration of zooplankton is low (e.g. during the winter months), zooplankton survival is boosted by a lower overall mortality rate.

8. K_F: The zooplankton half-saturation constant for grazing K_F works in a similar fashion to

that for the phytoplankton K_{nit}. In Equation 3.13, the value of K_F works alongside g_{max} to control the losses to phytoplankton and zooplankton through grazing. As K_F increases in value (assuming all other terms in Equation 3.13 remain fixed), the losses to phytoplankton and detritus through grazing decrease.

9. g_{max}: The maximum grazing rate g_{max} applies to feeding on both phytoplankton and detritus as zooplankton are assumed to be non-discriminatory feeders eating both phytoplankton and detritus in whatever proportion they are available. g_{max} works alongside K_F (above) in Equation 3.13, to determine the losses of the phytoplankton and detritus compartments to zooplankton by grazing. The higher the value of g_{max} (assuming all other terms in Equation 3.13 remain fixed) the greater the loss to the phytoplankton and detrtius compartments through grazing.

10. β_P: The assimilation efficiency of zooplankton feeding on phytoplankton is given by β_P. The proportion β_P of the eaten phytoplankton is digested and contributes to zooplankton growth, the remainder (1-β_P) is egested and as much as possible of this—within the bounds of the different carbon:nitrogen ratios of the different compartments (see Section 3.2.3)—is placed in the detrital compartment.

11. β_D: The assimilation efficiency of zooplankton feeding on detritus is given by β_D. This works similarly to β_P above with the proportion β_D of the eaten detritus digested and the remainder egested and placed in the detrital compartment. It is generally assumed that $\beta_P > \beta_D$ to reflect the higher nutritional value of phytoplankton.

12. F_{ingest}: This gives the fraction of the available food (phytoplankton and detritus) that is ingested by the zooplankton. This is used to multiply the assimilation of phytoplankton and detritus by zooplankton (see Section 3.2.3), to create the production term for the zooplankton.

13. F_{messy}: This parameterises the messy feeding by zooplankton—the fact that zooplankton do not ingest all the prey they eat. This material is returned to labile nitrogen and carbon—the nitrogen returns to the nutrient compartment and carbon to the DIC concentration. In Equations 3.15, 3.16 and 3.17 it can be seen that if all other parameters remain fixed increasing F_{messy} reduces the detrital concentration, and increases the nutrient and DIC concentrations.

14. F_{nmp}: This parameterises the contribution to labile nitrogen and carbon (nutrient and DIC), of the phytoplankton mortality. For DIC, Equation 3.17 shows simply that increasing F_{nmp}

increases the contribution of phytoplankton mortality to DIC. The same is true for nutrient, though to a lesser extent as F_{nmp} appears twice in Equation 3.16. Phytoplankton mortality is a major contributor to the detrital compartment. This contribution is reduced for higher values of F_{nmp} (see Equation 3.15).

15. F_{zmort}: In a similar way to F_{nmp} above, this parameterises the contribution to the nutrient and DIC concentrations of zooplankton mortality, with higher values leading to greater loss to the detrital compartment (Equation 3.15), and corresponding gain to nutrient and DIC concentrations (Equations 3.16 and 3.17).

16. v_s: The daily sinking rate for detritus is set by the value of v_s. Detritus is the only variable in HadOCC that sinks through the water column independently of ocean mixing. Below the mixed layer depth this sinking provides the primary export to the ocean floor. However, as nothing can sink through the ocean floor the build-up of un-remineralised (see below) detrital material is redistributed across the bottom three levels of the water column model.

17. Υ_c: The rain ratio parameter governs the effect of the formation of organic carbonate. HadOCC has only a single generic phytoplankton type explicity represented. Certain types of phytoplankton—principally coccolithophores—develop calcium carbonate shells, the formation of which changes the concentration of DIC and the alkalinity of the seawater in the euphotic zone. This effect is parameterised by assuming the production of carbonate to be proportional to new organic production, which in turn is assumed to be a fixed proportion of total gross production so that carbonate production is proportional to nutrient uptake at a rate determined by the rain-ratio Υ_c—the final term of Equation 3.17. The formation of carbonate releases organic carbon, so the higher the value of Υ_c, the more organic carbon is released to the DIC compartment.

18. Rm_{shall}: Bacteria are largely responsible for the remineralistion of detrital material in the ocean. They are not explicity present in HadOCC but instead are implicitly represented as a fraction, determined by the value of the remineralisation parameter of the available detritus being converted to dissolved nutrient. The remineralistaion parameter is given two separate values in HadOCC depending on the depth at which it is applied. Above 100m the shallow remineralisation rate Rm_{shall} is used as a constant.

19. Rm_{deep}: To represent the remineralistion of detrital material by bacteria below 100m in the water column a fraction, as determined by the value of the depth-dependent remineralisation rate of the available detritus is broken down to dissolved nutrient. The depth-dependent remineralisation rate is given by

$$\frac{Rm_{deep}}{z_i} \tag{3.20}$$

where Rm_{deep} is the deep remineralisation rate parameter and z the midpoint of the i^{th} depth level below 100m in the physical mixing model. This gives the remineralisation a decreasing effect with depth through the water column, with the rate at its lowest in the bottom depth level. Here, due to the large z—typically $\geq$ 3000m—the remineralisation approches 0, thereby forming the long-term biological pump component of the ocean carbon sink by mimicking the formation of stable sediments from the detritus.

20. Θ: Θ is the carbon to chlorophyll ratio in phytoplankton. It is known from measurements in culture to be highly variable, and to change according to the availability of light and nutrient, and with the temperature of the seawater [Cloern et al., 1995]. This work uses a single constant value for Θ in HadOCC as a fixed value is used in FAMOUS (see Section 3.4). In addition, fixing Θ as a parameter allows its effect to be explored directly in the sensitivity analysis.

3.3 HadOCC-GOTM

The sensitivity analysis detailed in Chapter 4 requires large numbers of HadOCC runs using different parameter values. To enable this, HadOCC is coupled with the General Ocean Turbulence Model (GOTM) of Burchard et al. [1999] (`www.gotm.net`), to produce a flexible 1-D ocean biogeochemical model [Kettle and Merchant, 2008], hereafter referred to as HadOCC-GOTM. HadOCC-GOTM is computationally relatively inexpensive to run (a one year integration of HadOCC-GOTM takes around 2-4 mins on a LINUX desktop computer), and can easily be adapted to run at different locations and for different timescales making it ideal for use in the sensitivity analysis.

GOTM is set up as a vertical column structure with levels of increasing size extending downwards from the sea surface. The top three levels are 10m in depth, then increase steadily to 1200m below which the remaining depth is split into levels of 615.3m (see Table 3.2). The number of levels used in the 1D HadOCC-GOTM is set to the level with the closest bottom of level depth to the depth of the site according to bathymetry data. This structure is the same as that used in FAMOUS and HadCM3 (see Section 3.4 below) and is appropriate for use with a biogeochemical model such as HadOCC since the key processes governing the uptake of carbon by phytoplankton growth occur in the upper ocean, as limited by the maximum mixed layer depth (usually around 50-200m).

The dynamics of the GOTM water column are based on Navier-Stokes equations (e.g. Acheson [1990]) for fluid motion simplified by both the use of the Boussinesq approximation—pressure is considered hydrostatic, and the thin shell approximation—the radius of the Earth is much greater than ocean depth, which allows simplification of the Earth rotation term. In addition, turbulent transport is approximated by diffusive transport—the eddy viscosity approximation. Horizontal

Table 3.2: GOTM water column depth levels used in HadOCC-GOTM and FAMOUS.

Level	Width (m)	Depth—mid-point of level (m)	Depth—bottom of level (m)
1	10	5	10
2	10	15	20
3	10	25	30
4	10.2	35.1	40.2
5	15.3	47.85	55.5
6	23.0	67.0	78.5
7	34.5	95.75	113.0
8	51.8	138.9	164.8
9	77.8	203.7	242.6
10	116.8	301.0	359.4
11	175.3	447.05	543.7
12	263.2	666.3	797.9
13	395.3	995.55	1193.2
14	615.3	1500.85	1808.5
15	615.3	2116.15	2423.8
16	615.3	2731.45	3039.1
17	615.3	3346.75	3654.4
18	615.3	3962.05	4269.7
19	615.3	4577.35	4885.0
20	615.3	5192.65	5500.3

terms in the three-dimensional mean flow equations are then parameterised assuming horizontal homogeneity to give a one-dimensional equation along the vertical axis [Burchard et al., 1999].

Properties of the water (temperature and density), and dissolved (nutrient and DIC) and non-dissolved (phytoplankton, zooplankton and detritus) substances are considered in GOTM as tracers. The general 1-D equation for the tracer Y is

$$\partial_t Y = \partial_z(\nu_Y^t \partial_z Y) + \Gamma_Y - \Lambda_Y + R_Y \tag{3.21}$$

where ∂_t is the time derivation, ∂_z the vertical gradient, ν_Y^t the turbulent diffusivity, Γ_Y the inner source production term (e.g. $I_{lim}N_{lim}P$ for phytoplankton in Equation 3.6), Λ_Y the inner source destruction term (e.g. $-M_P - H_P - \eta P$ for phytoplankton in Equation 3.6) and R_Y the restoring term (see below for the use of the restoring term to replenish nutrients).

The movement of all the HadOCC biological compartments, with the exception of detritus which sinks independently (see Section 3.2.4), is determined by turbulent mixing of the GOTM water column. The upper ocean is well mixed by waves and wind-stress creating a layer of water with near uniform temperature, salinity and biological tracer concentrations—the mixed layer (see Section 1.5.2). The depth of the mixed layer in HadOCC-GOTM is calculated using the Richardson number (the ratio of kinetic to potential energy) of the water column. The mixed layer is defined to

be the levels of the water column in which the Richardson number satisfies the condition $R_i \leq 0.5$, where

$$R_i = \frac{\mathcal{N}^2}{\mathcal{M}^2} \tag{3.22}$$

where $\mathcal{N}$ is the bouyancy frequency and $\mathcal{M}$ the shear frequency of the water column.

As stated previously, phytoplankton growth in HadOCC is dependent on the availability of sunlight and nutrient. The replenishment of nutrient in the upper ocean by mixing depends partly on lateral advection from upwelling regions and estuarine regions. To represent this additional input from outside the 1-D GOTM column, the nutrient in HadOCC-GOTM is relaxed below the productive depth to a nutrient profile taken from Levitus et al. [1993]. The productive depth is defined to be the greatest depth at which both light and nutrient are available in sufficient quantities for photosynthesis to take place—i.e. the shallower of the mixed layer depth or euphotic depth. The modelled nutrient profile (N) is relaxed to the fixed Levitus et al. [1993] profile (N_{Lev}) by reducing the difference between them by $1/60$ per days worth of timesteps (Δt_d) such that the replenished nutrient

$$N_{new} = \frac{N + (N_{Lev} - N)\Delta t_d}{60} \tag{3.23}$$

HadOCC-GOTM is forced with meterological data for air pressure, wind speed, relative humidity, air temperature and total cloud cover at six hourly intervals. This data is taken from the ECMWF 40-year Re-analysis (ERA-40) dataset (see Section 4.2.1).These are the meteorological processes that influence the rate of air-sea CO_2 transfer (wind, humidity, pressure and temperature—see Sections 1.4 and 1.6) and the amount of light (cloud cover) that reaches the ocean surface and is hence available for phytoplankton photosynthesis—see Section 1.5.2.

3.4 FAMOUS

To further investigate the global effects of uncertainty in the ocean biogeochemical parameterisation on the air-sea CO_2 flux it is neccessary to use a global climate model with a 3D representation of ocean circulation. The FAst Met Office UK Universities Simulator (FAMOUS) model (`www.famous.ac.uk`) [Smith et al., 2008; Jones et al., 2005], is a lower resolution version of the widely used Hadley centre Climate Model 3 (HadCM3) [Gordon et al., 2000] ocean-atmosphere GCM.

FAMOUS uses most of the HadCM3 code but by using a lower resolution and a longer timestep

requires only around 10% of the computational cost of HadCM3, enabling simulations of 100 years or more per wallclock day to be carried out on high performance computing facilities. FAMOUS has roughly half the resolution of HadCM3, a 5° lat x 7.5° long atmosphere grid with 11 levels (HadCM3 uses 2.5° lat x 3.75° long with 19 levels), and a 2.5° lat x 3.75° long ocean grid with 20 depth levels (HadCM3 uses 1.25° lat x 1.25° long). FAMOUS is tuned to reproduce the equilibrium climate and climate sensitivity of HadCM3. This 'traceability' allows FAMOUS to be used to perform ensemble runs to explore parameter sensitivities that are too costly to perform directly on HadCM3 [Jones et al., 2005]. FAMOUS uses the HadOM3 model for the ocean, in which HadOCC is used to represent the role of marine biogeochemistry in the global carbon cycle, though HadOCC in FAMOUS uses simplified parameterisations of light penetration and shading to those used in the original model of Palmer and Totterdell [2001] [Smith et al., 2008].

For this project, FAMOUS job xdbua (xdbua is the National Centre for Atmopheric Sciences (NCAS) Unified Model job code) as detailed in Smith et al. [2008] was ported to Edinburgh and run on the Edinburgh Compute and Data Facility (ECDF) computing cluster (`www.ecdf.ed.ac.uk`) which enables a run-time of approximately one model year to ten minutes. The FAMOUS model runs detailed in Chapter 5 start from well spun-up (6000 years) FAMOUS job xdbua data fields so that the initial biogeochemical tracer fields used in the analysis (nutrient, phytoplankton etc...) do not depend on the original fields used.

3.4.1 FAMOUS carbon cycle

FAMOUS job xdbua uses a fixed atmospheric CO_2 concentration with a pCO_2^{air} of 290 ppm, which approximates to the pre-industrial atmosphere of the 1850s. The global carbon cycle in FAMOUS is not fully coupled. The ocean 'sees' the fixed pCO_2^{air} which is not altered by changes to the air-sea CO_2 flux. In the well spun up FAMOUS job xdbua of Smith et al. [2008], the ocean carbon content is in equilibrium with the atmosphere, resulting in a near-zero net global air-sea CO_2 flux.

3.4.2 Ocean tracers in FAMOUS

The conservation of tracers in the ocean is important to prevent artificial effects in long climate simulations [Smith et al., 2008]. As a ridgid-lid fixed-volume ocean model, the representation of freshwater input and evaporation requires corrections to the tracer fields to conserve their quantities [Smith, 2009]. In FAMOUS the effect of local freshwater fluxes into the ocean and evaporation that can change tracer concentrations is represented as a 'virtual' tracer flux. HadCM3 uses a global reference salinity to conserve global salinity concentrations but this was found to distort ocean circulation in the development of FAMOUS. Instead, the earlier version of FAMOUS of Jones et al. [2005] used local salinity concentrations but this did not

guarantee conservation of global salinity and biogeochemical ocean tracers [Smith et al., 2008]. To ensure global conservation of tracers FAMOUS version xdbua uses a small time-dependent volume-uniform adjustment to the salinity, alkalinity, DIC and nutrient fields.

For each model year, the freshwater fluxes f_{fresh} and virtual tracer fluxes f_{virt} are accumulated for each timestep (giving $F_{fresh} = \int f_{fresh} dt$, $F_{virt} = \int f_{virt} dt$). The global drift for each tracer that should result from the summed freshwater fluxes is then calculated at the end of each year using constant global reference values T_{ref}—35 psu (practical salinity units) for salinity, 2363 μmol l^{-}1 for alkalinity and 2075 μmol l^{-}1 for DIC ($D_{fresh} = T_{ref} \int F_{fresh} dxdy$). These are compared with the actual drift in each tracer calculated from the virtual tracer fluxes ($D_{virt} = T_{ref} \int F_{virt} dxdy$), and a constant global adjustment $Adj = D_{fresh} - D_{virt}$ is calculated for each tracer and applied uniformly throughout the vertical water column to the tracer field on every timestep of the next year. This adjustment corrects the global tracer drift with respect to freshwater fluxes [Smith et al., 2008; Palmer, 1998].

There is no riverine input of nutrient or DIC in FAMOUS, so in the absecnce of uptake from the atmosphere, the total ocean carbon and nutrient (both labile and in organic matter) is essentially fixed, subject to the global drift corrections described above [Smith, 2009]. In contrast to HadOCC-GOTM, no sedimentation of organic detritrus takes place in FAMOUS [**?**]. The small amount of detritus that arrives at the ocean floor is returned to the top ocean level to conserve carbon and nutrient quantities [Palmer, 1998]. With a detrital sinking rate of 10m day^{-1} this introduction of detritus to the top of the ocean has a timescale of between 1-2 years assuming vertical transport only.

Sensitivity analysis of HadOCC-GOTM

4.1 Overview

A sensitivity analysis is performed on HadOCC-GOTM at four sites in the North Atlantic: 0^oN, 15°N, 30°N and 45°N along the 30^oW meridian. These sites have different ocean surface meteorology (see Figures 4.1 and 4.2) and resulting physical ocean behaviours allowing investigation of the overall importance in the model of the biological parameters detailed in Section 3.2.8. This offers greater insight to the global importance of parameters than similar single-site studies (e.g. Druon and Le Fèvre [1999]). Assessing the global parameter importance is relevant as HadOCC is used to represent the role of the ocean ecosystem in global biogeochemical cycles in the HadCM3 and FAMOUS GCMs (see Section 3.1 and 3.4).

Probability distributions appropriate to the fundamental properties of the parameters are used to perform the analysis. The analysis is performed using both the traditional SA methods and the GEM-SA package detailed in Section 2.4.4, and the results of the two methods compared. The sensitivity of three model outputs—net annual air-sea CO_2 flux (mol CO_2 m^{-2} yr^{-1}), annual export (mg C m^{-2} yr^{-1}), and primary production (gC m^{-2} yr^{-1})—to variation in the parameters is tested. Air-sea CO_2 flux is essential in the calculation of absorption of anthropogenic emissions by the ocean, and all three are key processes in climate prediction models.

There are varying definitions for the export of sinking organic carbon through the water column. The most commonly used is for export to be defined as the material that sinks below the euphotic zone as this is material exported away from the site of production. However, the mixed layer can extend well below the euphotic zone, allowing recycling of the material that has sunk out of the euphotic zone back into it. This recycled material can then be eaten or broken down to nutrient and used for growth. Here export is defined to be the annual accumulation of detrital material that sinks below the maximum mixed layer depth (MLD) of the water column and is therefore permanently removed from productive waters on the $\sim$ 600 year timescale of ocean turnover [Curry and Webster, 1999]. This material, for the purposes of short-term modelling of the ocean carbon cycle, is the biological pump component of the ocean carbon sink.

4.2 Method

4.2.1 Model Setup

HadOCC-GOTM is run at 0°, 15°, 30° and 45° N along the 30° W meridian in the Atlantic ocean. Initial conditions at each location for alkalinity [Lee et al., 2006] and dissolved inorganic carbon (DIC) [Key et al., 2004] are obtained from the Carbon Dioxide Information Analysis Center (CDIAC). Nitrate profiles, to which the model relaxes to resupply, are taken from the World Ocean Atlas 2005 [Garcia et al., 2006]. To drive the model, meteorological data are taken from ECMWF 40-year Re-analyis (ERA-40) data; these comprise of air pressure, wind speed, relative humidity, air temperature and total cloud cover, at 6 hourly intervals. Figure 4.1 shows temperature, and Figure 4.2 wind speed for the four sites, with increasingly strong seasonal cycles in temperature and wind speeds with increasing latitude. HadOCC-GOTM uses the quadratic Wanninkhof '92 gas transfer parameterisation [Wanninkhof, 1992] as used in the Takahashi et al. [2002] CO_2 flux climatology to calculate the effect of the wind speed on the gas transfer velocity.

At each location, HadOCC-GOTM is run with five hundred different sets of the biological parameters under investigation (see Section 3.2.8) which used in conjuction with a latin hypercube sampling method (see Section 2.3.2) gives good coverage of the parameter space. The model is spun up for six years with yearly repeating meteorological data from 2004 to remove sensitivity to the initial conditions (see Section 4.2.2 below). The three model outputs under investigation (air-sea CO_2 flux, export and primary production) are then taken from the seventh year. Output differences between the runs for a given location can be attributed solely to the change in the parameter values.

4.2.2 Model spin up

HadOCC-GOTM needs to be spun up so that the initial concentrations of the state variables do not affect the results. Figures 4.3 to 4.6 show the concentrations of the HadOCC state variables at 15°N for a ten year run. The annual concentration cycle for these can be seen to stabilise after six years—the other sites (not shown) also stabilise after six years or less. The seasonal ocean ecosystem cycle can be clearly seen, with high nutrient concentration early in the year leading to a rapid increase in phytoplankton concentration, which leads in turn to increasing zooplankton and detrital concentrations. Data for use in the SA are taken from the seventh year to minimise the computational expense of performing the large number of runs required.

4.2.3 Model parameters and sensitivity analysis

Twenty parameters are investigated in this study. These are listed in Table 4.1 with the current HadOCC value, and values given in the literature e.g. from other comparable models. For each

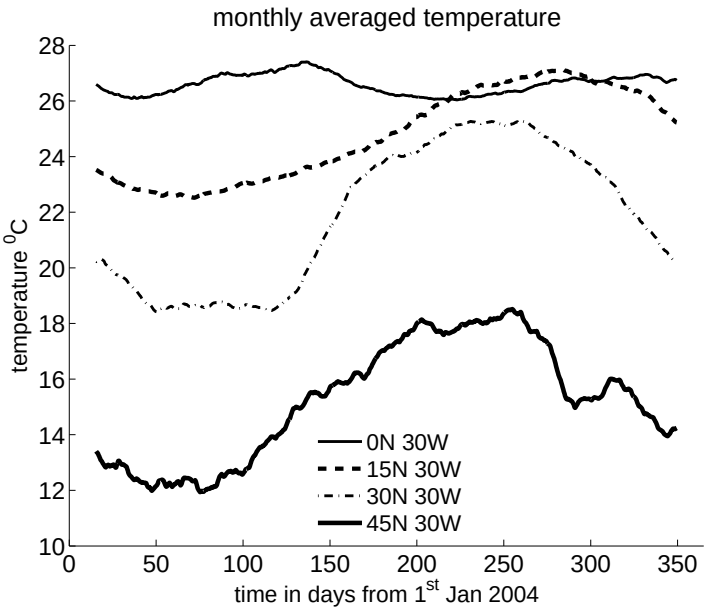

Figure 4.1: ECMWF temperature meteorology—for clarity data plotted are smoothed monthly average temperature for the year 2004 at the four sites (GOTM-HadOCC is forced by unsmoothed time series). Note the stronger seasonal cycle of the higher latitude sites.

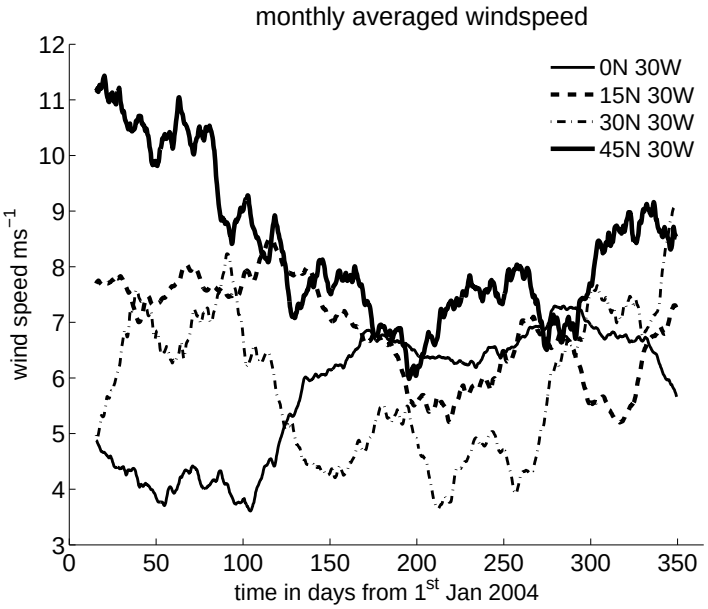

Figure 4.2: ECMWF windspeed meteorology—for clarity data plotted are smoothed monthly average windspeed for the year 2004 at the four sites (GOTM-HadOCC is forced by unsmoothed time series). Note higher windspeed and greater seasonsal variability at higher latitudes.

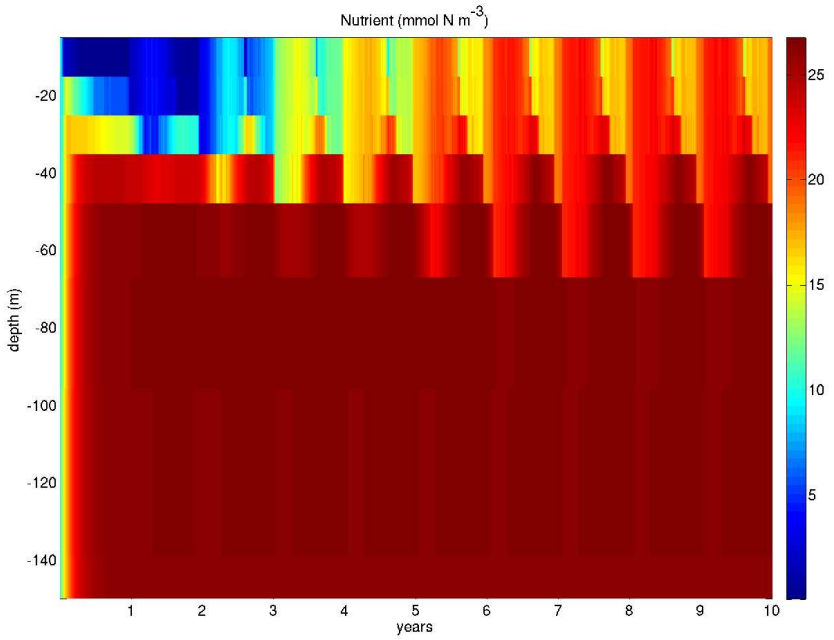

Figure 4.3: Nutrient concentration (mmol N m^{-3}) at 15°N forced with repeat meteorology for ten years showing stabilisation in seven years. Runs at the other sites behave similarly.

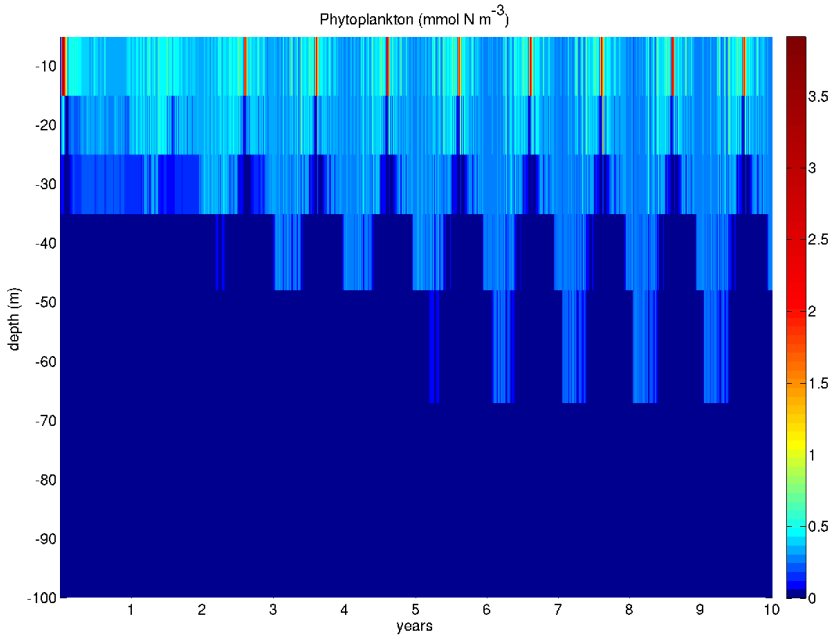

Figure 4.4: Phytoplankton concentration (mmol N m^{-3}) at 15°N forced with repeat meteorology for ten years showing stabilisation in seven years. Runs at the other sites behave similarly.

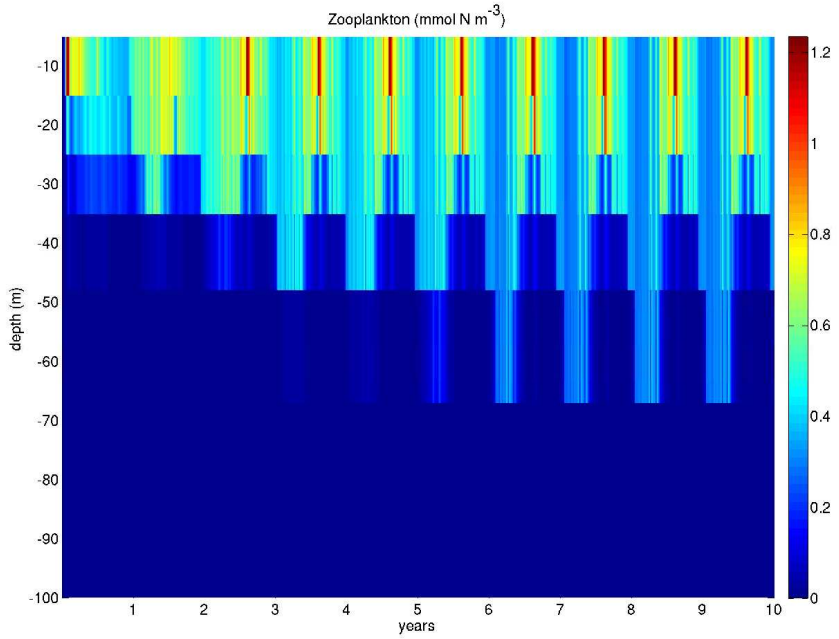

Figure 4.5: Zooplankton concentration (mmol N m^{-3}) at 15°N forced with repeat meteorology for ten years showing stabilisation in seven years. Runs at the other sites behave similarly.

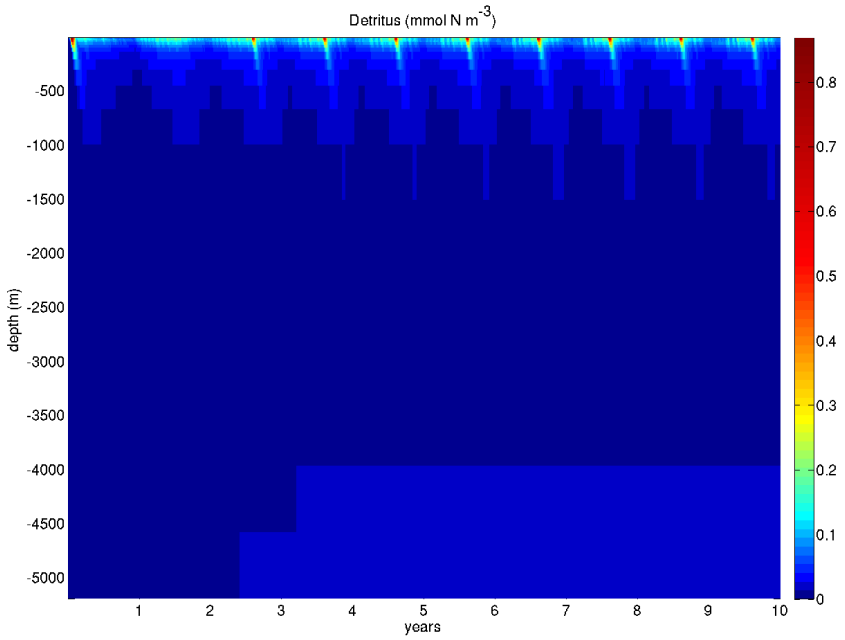

Figure 4.6: Detritus concentration (mmol N m^{-3}) at 15°N forced with repeat meteorology for ten years showing stabilisation in seven years. Detritus cannot sink out of the water column, so any that sinks to the bottom of the ocean is spread over the bottom three model levels leading to the rise in detrital concentration seen here (see Section 3.2.4). Runs at the other sites behave similarly.

Table 4.1: HadOCC parameters and literature values (references and additional information in Table 4.2).

Parameter	Units	Had -OCC value	Literature values
K_{nit}	mMolNm^{-3}	0.1	0.01-0.5, 0.82, 0.85[1], 0.5[2], 0.001, 0.003 [3], 0.5[4]
P^s_{max}	d^{-1}	1.5	3-5.1 [3], 0.25, 0.1-4.1 [6], 0.01-1.71[1]
α	mg C mg Chl^{-1} h^{-1} (W m^{-2})$^{-1}$	0.09	0.023-0.399[7], 0.033-0.2167[2], 0.036, 0.032, 0.07[5], 0.042, 0.113-0.172, 0.067-1.2[1], 0.085, 0.185, 1.055[14]
η	d^{-1}	0.05	0.001[8], 0.0-0.025[3]
m_0	d^{-1} (mMolNm^{-3})$^{-1}$	0.05	0.1-0.25, 0.03[1], 0.05[9], 0.008[10], 0.035[11], conversion[25]
μ_1	d^{-1}	0.05	0.03-0.05[5], 0.2[12]
μ_2	d^{-1}(mMolNm^{-3})$^{-1}$	0.3	0.2 [13]
K_F	mMolNm^{-3}	0.5	0.4-0.5[14], 1.0[11]
g_{max}	d^{-1}	0.8	0.06-1.9, 1.1, 2.0 [1], 0.1-0.5, 0.9[5], 2.0[15]
β_P	-	0.9	0.75[9], 0.75, 0.46, 0.76[16], 0.7-0.95[17]
β_D	-	0.65	0.75[9], and others in β_P above
F_{ingest}	-	0.77	-
F_{messy}	-	0.1	0.23[18], 0.02[8]
F_{nmp}	-	0.01	-
F_{zmort}	-	0.67	-
v_s	m d^{-1}	10	32.0[19], 5.0[2], 3.0[19], 20.0[20], 24.7[8]
Rm_{shall}	d^{-1}	0.1	0.05-0.1[21], 0.05[22]
Rm_{deep}	md^{-1}	8.58	see Rm_{shall} above
Υ_c	-	0.013	0.15, 0.25, 0.08-0.12[6], 0.16[23], 0.05-0.25[24]
Θ	-	40	10-333[26]

parameter, its 5% to 95% confidence interval is estimated from expert opinions and the literature values in Table 4.1. Since precise numerical limits for the parameters are unknown, use of a range is arguably unjustified and confidence intervals are more appropriate for describing the likely spread of values (see Section 2.3.1). The parameters are in two distinct categories—positive definite parameters (e.g., the detrital sinking velocity v_s), and those with a value confined in the interval 0 to 1 (e.g., the assimilation efficiency of zooplankton feeding β_P). For the first group, a Davies distribution [Hankin and Lee, 2006] is used to represent their probability, while for the second group a Beta distribution [Freund, 1992] is used.

The Davies distribution is a continuous positive probability distribution defined by three parameters which determine the central value, and the shapes of the tails either side of this central value [Hankin and Lee, 2006]. As the shapes of the tails of the Davies distribution are controlled by independent and potentially different parameters, the central value will not necessarily be the mean of the distribution. The definition of the Davies distribution allows the use of the nominal model value as the central value, with the tail-shape parameters generated from the 5^{th} and 95^{th} percentile confidence intervals of the parameter. This allows for more information to be included in the prior distribution than would appear using a log normal distribution, the other possible candidate for a continuous positive distribution, which is defined by only a mean and spread.

Table 4.2: References and additional information for Table 4.1.

Footnote Number	Citation and information
1	Waniek and Holiday [2006]
2	Zielinski et al. [2002]
3	Geider et al. [1998]
4	Baklouti et al. [2006]
5	Druon and Le Fèvre [1999]
6	Chuck et al. [2005]
7	Geider et al. [1997]
8	Pahlow et al. [2008]
9	Popova et al. [2002]
10	Tjiputra et al. [2007]
11	Pätsch et al. [2002]
12	Pätsch et al. [2002] single zooplankton mortality rate
13	Waniek and Holiday [2006] single zooplankton mortality rate
14	Kettle and Merchant [2008]
15	Anderson and Pondaven [2003]
16	Waniek and Holiday [2006] single assimilation parameter
17	Druon and Le Fèvre [1999] single assimilation parameter
18	Anderson and Pondaven [2003] to DOM
19	Anderson et al. [2007]
20	Kawamiya et al. [2000]
21	Druon and Le Fèvre [1999] at all depths
22	Waniek and Holiday [2006] at all depths
23	Fujii and Chai [2007]
24	Fujii et al. [2005]
25	Phytoplankton concentration is assumed to be 1 mMol N m^{-3} for purposes of conversion
26	Cloern et al. [1995]

The beta distribution is a family of continuous probability distributions defined on the interval [0,1] with a shape determined by the values of two non-negative parameters, α and β [Freund, 1992]. Different combinations of α and β values allow for a huge range of different distribution shapes; straight slopes, concave and convex curves. Of primary importance to this project is the restriction on the interval [0,1] which prevents any theoretically meaningless parameters being generated during the sampling. The relevant α and β values are computed as before from the 5^{th} and 95^{th} percentile confidence intervals of the parameter. In this instance it gives the parameters a convex non-symmetric sampling distribution which goes to zero at 0 and 1.

The parameters that relate directly to phytoplankton growth (K_{nit}, P^s_{max}, α, m_0), are generic to many NPZD and more complex models giving a good resource in determining confidence intervals. For these parameters the smallest and largest values found in the literature are used for the 5% to 95% confidence interval (see Tables 4.1 & 4.3). Parameterisations of processes

such as zooplankton grazing are however less universal, meaning that there is less information available on which to base confidence intervals. Following consultation with experts who use HadOCC in their work these parameters are given a 5% to 95% confidence interval of the nominal HadOCC value $\pm$ 90% of the difference between the nominal HadOCC value and the closest theoretical limit. Figure 4.7 shows plots of the priors generated using this approach.

The treatment of the deep remineralisation rate Rm_{deep} (used at all levels deeper than 100m) is different. While the value input to the model is > 1 m d^{-1}, the actual remineralisation rate is determined by the value of Rm_{deep} divided by the depth of the midpoint of the depth level at which it is applied, giving a decreasing rate with increasing depth (see Section 3.2.8). Due to this, a scaled Beta sampling distribution is used for Rm_{deep} as its value as used in the model must lie in the [0-1] interval. To establish a confidence interval for Rm_{deep}, the 95% confidence interval for Rm_{shall} is used as the upper limit for $Rm_{deep}/138.9$m (the midpoint of the depth level below 100m in GOTM is at 138.9m), from which the 90% range is established as with the other parameters above.

From these distributions 500 parameter sets are selected using a latin hypercube sampling method (see Section 2.3.2), which maximizes efficient coverage of the whole parameter space by ensuring selection of parameter values from their full range. These parameter sets are then run in HadOCC-GOTM and the results recorded alongside the appropriate parameter set. The calculated outputs are screened to check for failed runs that have produced wholly unfeasible results created by parameter combinations causing numerical problems (e.g. divison by zero). The Takahashi climatology [Takahashi et al., 2002] is used to screen the CO_2 flux results and set the condition that export amd primary production must be ≥ 0 (see below).

4.2.4 Screening

The outputs are screened for implausible results using three conditions. Export and primary production are required to be ≥ 0. The CO_2 flux results are screened by using the global range of the Takahashi annual CO_2 climatology [Takahashi et al., 2002] of -11 to 13 mol CO_2 m^{-2} yr^{-1}. The Takahashi range is used for the standard deviation $\sigma = 12$ mol CO_2 m^{-2} yr^{-1} and the upper and lower limits on the CO_2 flux dataset are set to be four σ from the midpoint ($= 2$ mol CO_2 m^{-2} yr^{-1}) of the Takahashi range giving limits of -46 to 50 mol CO_2 m^{-2} yr^{-1}. Runs that produce results outwith these conditions are discarded in their entirety.

At 0°N no runs produced results outside these limits. A negative primary production was produced by two runs at 15°N and five runs at 30°N and one run at 45°N—these were all discarded. These error runs were noted to coincide with very low values (5-13) of the carbon to chlorophyll ratio Θ. In total, only eight model runs from a total of two thousand (four times five hundred) were removed by screening.

Table 4.3: HadOCC parameters: Prior distributions and confidence intervals sampled to generate parameter sets to perform SA. Intervals are taken from either upper and lower literature values (where available), or from 90% of HadOCC value to closest theoretical limit each way (CTL). The resulting priors are shown in Figure 4.7. Intervals are used as range for the GEM-SA analysis.

no	Parameter	Units	Sampling Distribution	5 %ile	95 %ile	Source
1	K_{nit}	mMolNm^{-3}	Davies	0.01	0.85	Upper and lower literature
2	P^s_{max}	d^{-1}	Davies	0.01	5.1	Upper and lower literature
3	α	mgC mg chl^{-1} h^{-1} (Wm^{-2})$^{-1}$	Davies	0.023	1.2	Upper and lower literature
4	η	d^{-1}	Davies	0.005	0.095	90% of HadOCC to CTL
5	m_0	d^{-1} (mMol N m^{-3})$^{-1}$	Davies	0.008	0.25	Upper and lower literature
6	μ_1	d^{-1}	Davies	0.03	0.2	Upper and lower literature
7	μ_2	d^{-1} (mMol N m^{-3})$^{-1}$	Davies	0.03	0.57	90% of HadOCC to CTL
8	K_F	d^{-1}	Davies	0.4	1.0	Upper and lower literature
9	g_{max}	d^{-1}	Davies	0.06	2.0	Upper and lower literature
10	β_P	-	Beta	0.46	0.95	Upper and lower literature
11	β_D	-	Beta	0.46	0.75	Lower limit from β_P literature
12	F_{ingest}	-	Beta	0.63	0.977	90% of HadOCC to CTL
13	F_{messy}	-	Beta	0.02	0.23	Upper and lower literature
14	F_{nmp}	-	Beta	0.001	0.019	90% of HadOCC to CTL
15	F_{zmort}	-	Beta	0.373	0.967	90% of HadOCC to CTL
16	v_s	m d^{-1}	Davies	3.0	32.0	Upper and lower literature
17	Rm_{shall}	d^{-1}	Beta	0.05	0.1	Upper and lower literature
18	Rm_{deep}	m d^{-1}	Beta (see text)	3.8	13.36	90% to Rm_{shall} limit (see text)
19	Υ_c	-	Beta	0.013	0.25	Upper and lower literature
20	Θ	-	Davies	10.0	333.0	Upper and lower literature

4.3 Results

Table 4.4 gives the CO_2 flux, export and primary production at the four sites, calculated using the standard HadOCC parameter values as detailed in Table 4.1. The direction of the CO_2 flux results compare favourably with the Takahashi et al. [2002] climatology, with outgassing in the tropics and in-gassing at higher latitudes, while the export and primary production results appear resonable for the locations. Table 4.5 details the minimum, maximum, median, scaled median absolute difference from the median, mean and standard deviation of the screened results from the perturbed parameter suites. Variation in the parameter values used has a significant effect on all the output values at all the sites. The median and means for CO_2 flux are comparable with the control results at all sites, while for export and primary production the control results compare more favourably with the medians of the perturbed results than the means, which are consistently much greater, reflecting the very high export and primary production calculated by some perturbed parameter combinations. For CO_2 flux, the 0°N site has the smallest range of results, all of which are outgassing. The results for the central sites at 15°N and 30°N have much greater ranges, and while the mean values for these sites are for ingassing of CO_2, both high in- and out- gassing results are present. The range of results at 45°N is smaller again with most results giving a flux into the ocean. These results concur with the general pattern of ingassing and outgassing shown in the Takahashi 2002 climatology [Takahashi et al., 2002] (Figure 1.5). For export, as might be expected due to the relatively low productivity of the tropics, the smallest range and maximum is at the 0°N site. Much higher export results are obtained at the central sites with 15°N having the highest maximum and mean. The primary production results exhibit the same pattern with the lowest values at the 0°N site and the greater at the central sites. While due to the nature of this work these results are not expected to precisely match estimates of the primary production, the control and mean values for the four sites are comparable with estimates for average annual ocean primary production (e.g., Ricklefs [1990] and Field et al. [1998]).

The results shown in Table 4.5 show the huge effect which the uncertainty in the biological parameters has on the calculation of oceanic processess fundamental to controlling global climate. The CO_2 flux results show that the ocean's role in reducing the atmospheric CO_2 concentration is greatly influenced by the values used for the biological parameters. Identifying which biological parameters cause this huge variation is important to understanding the possible errors in the air-sea CO_2 flux calculated by GCMs.

Table 4.4: Control results—CO_2 flux, export and primary production calculated at 0°N, 15°N, 30°N and 45°N sites using the standard HadOCC parameter values as in Table 4.1.

Output	Location	Control result
CO_2 flux (mol CO_2 m^{-2} yr^{-1})	0°N	-0.41
	15°N	2.00
	30°N	2.22
	45°N	1.40
Export (mg C m^{-2} yr^{-1})	0°N	36.0
	15°N	7003.0
	30°N	5764.5
	45°N	1148.3
Primary production (gC m^{-2} yr^{-1})	0°N	2.0
	15°N	213.2
	30°N	211.6
	45°N	49.6

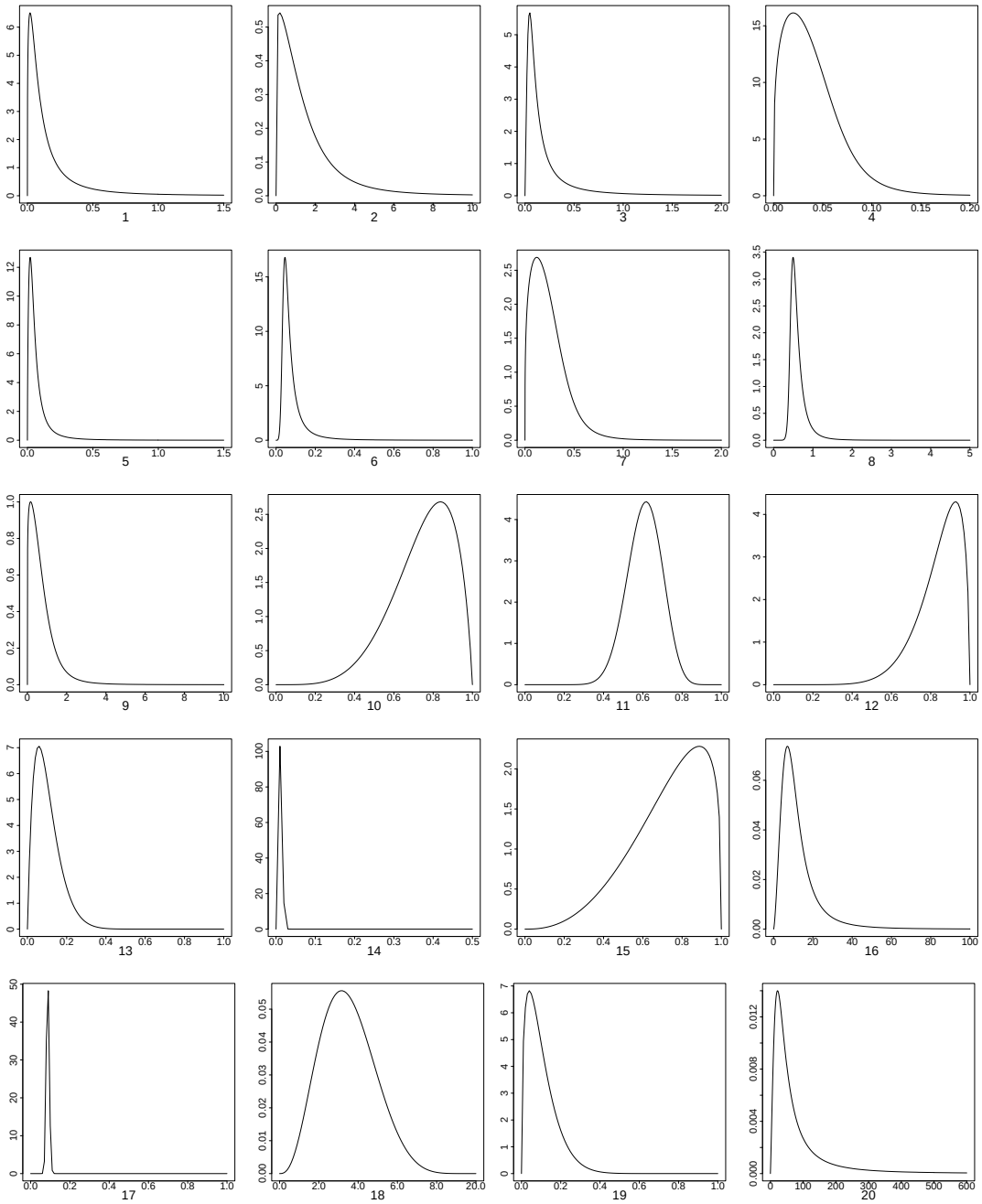

Figure 4.7: Priors for all parameters (numbered as in Table 4.3) generated from confidence intervals using Davies or Beta distributions as detailed in Table 4.3.

Table 4.5: Results for net annual air-sea CO_2 flux (mol CO_2 m^{-2} yr^{-1}), annual export below maximum MLD (mgC m^{-2} yr^{-1}) and primary production (gC m^{-2} yr^{-1}). MADM is the median absolute deviation from the median scaled such that for a normal distributon it is equal to the standard deviation σ.

Output	Location	min	max	median	MADM	mean	σ
CO_2 flux mol CO_2 m^{-2} yr^{-1}	0^oN	-0.62	-0.28	-0.41	0.024	-0.42	0.045
	15^oN	-5.2	17.1	0.51	0.97	2.1	3.6
	30^oN	-11.5	15.1	0.78	0.93	1.65	2.47
	45^oN	-0.002	3.6	1.2	0.15	1.2	0.34
Export mgC $m^{-}2$ yr^{-1}	0^oN	0.004	4167	32.3	46.8	231	552
	15^oN	0.12	478985	4269	6243	19965	46785
	30^oN	0.005	277219	3364	4862	13235	28677
	45^oN	0.032	41377	799	1148	2323	4578
Primary production gC $m^{-}2$ yr^{-1}	0^oN	0	2926	1.74	2.48	13.0	135.6
	15^oN	0	98875	89.5	111.0	443.5	4483
	30^oN	0	61805	91.4	107.3	311.9	2819
	45^oN	0	18084	24.2	21.0	91.9	828.7

4.4 Sensitivity analysis

The results from the runs across the different locations are now used to identify the most sensitive biological parameters for each of the outputs using the methods discussed in Chapter 2. However, as a first step, a one-at-a-time (OAT) analysis is performed to identify parameters whose variation has a large effect on the output and so are likely to be found to be influential in the global SA.

4.4.1 OAT analysis

Figures 4.8 (CO_2 flux), 4.9 (export), and 4.10 (primary production), show one-at-a-time (OAT) plots for each parameter varied across its 5% to 95% confidence range from Table 4.3, at the 30°N site. Two important features are clear from these OAT plots. Firstly, for each output, changing the value of a few parameters—P^s_{max}, α, g_{max} and v_s for CO_2 flux, v_s and Rm_{deep} for export, P^s_{max} and α for primary production, has a greater effect than varying the other parameters. The rest of the parameters change the output less, with variation of some having virtually no effect: for example—the value of the parameters F_{messy} and F_{nmp} have negligible influence on any of the outputs. This demonstrates that certain parameters are likely to be more sensitive than others and indicates which these are msot likely to be in the global SA. Secondly, the relationship between the outputs and the parameter values are almost all monotonic. Θ is the one exception but is monotonic for all but the lowest values. This justifies the use of correlations as an initial step to analyse the global data set in which all parameters are varied simultaenously. Additionally, the parameters that have the most effect are reasonable in the context of expected behaviour of the model and the ocean. As expected the detrital sinking parameter v_s has the strongest effect on export (Figure 4.9), with a higher daily sinking rate leading to a higher export, while the photosynthesis parameters P^s_{max} and α have the strongest effects on primary production (Figure 4.10), with higher values corresponding with higher primary production as expected.

4.4.2 Correlations between parameters and output

Correlations between each of the set of values for each parameter and the three ouputs are calculated to give a simple measure of the influence of each parameter. I calculate both the traditional linear Pearson correlation (Fig. 4.11) and the Kendall (rank) correlation (Fig. 4.12). The Pearson correlation is 1 in the case of an increasing linear relationship, -1 in the case of a decreasing linear relationship and in all other cases a value in between -1 and 1. The closer the correlation value to 1 or -1, the stronger the linear relationship between the parameter and the output. The Kendall rank correlation works similarly but calculates the strength of the relationship between the rank of each parameter value, and the rank of the corresponding output value, and so describes the strength of the monotonic relationship rather than the exclusively linear relationship assessed by the Pearson correlation (see Section 2.4.2).

Both methods broadly agree on the more influential parameters for CO_2 flux and export (Figs. 4.11 and 4.12). For primary production, the Pearson correlation overestimates the importance of

α, where a value of ≈ 1 is given, and of K_{nit}, which is given a correlation of ≈ 0.3. Scatter plots (not shown), of the parameters against outputs show that the overly high Pearson correlations arise due to a few individual data points located outside the main cluster of data. The Kendall correlation results (Fig 4.12 plots C, F, I & L), due to the use of the rank of the value instead of actual value are not affected by these. Overall, the Kendall correlation gives a better indication of parameter significance though the similarity with the Pearson results (excepting the case of primary production discussed above), show that the relationships between the parameters and the outputs are not highly non-linear.

Looking at the correlation results for the different outputs in turn, parameters with higher correlations (both Pearson and Kendall) are in general the same across all four sites. For CO_2 flux, the sink rate v_s (parameter 16), the rain ratio Υ_c (parameter 17, which implicitly parameterises carbonate formation), and phytoplankton growth parameters (P^s_{max} (parameter 2), α (parameter 3) and η (parameter 4)) have the highest correlations. As should be expected, the sink rate v_s (parameter 16), deep remineralisation rate Rm_{deep} (parameter 18) and phytoplankton growth parameters are strongly correlated with export results while primary production is most strongly correlated with phytoplankton growth parameters. The results for all three outputs at 15°N are very similar to those at 30°N. The meteorological forcings experienced by these central sites are the most alike (see Figures 4.1 and 4.2) of the four different forcings used.

Also worth noting is the similarity between the correlation results for CO_2 flux and export (parameters with high correlations are in general the same for these two outputs). The results for the CO_2 flux and export have a Pearson (linear) correlation of 0.30 at 0°N and ~ 0.7 at 15°N, 30°N and 45°N, indicating that higher CO_2 flux into the ocean is associated with greater export.

4.4.3 Regression analysis

An all-subsets regression is now applied, using the Bayesian information criterion (BIC) to select improved models. For linear regression models with normally distributed residuals the BIC is

$$BIC = n\ln(\frac{RSS}{n}) + k\ln(n) \tag{4.1}$$

where n is the sample size (here = 500 minus the small number of runs removed by the screening process), RSS is the residual sum of squares from the fit and k the number of regressors (parameters plus the intercept) used. The BIC increases with both the RSS and the number of parameters used (k), so the lowest BIC balances the fitted variance against the number of parameters used. The BIC penalises the number of parameters more strongly than the other frequently used RSS fitting selector, the Akaike information criterion (see Section 2.4.3.2). The BIC is chosen here as the purpose of this work is to identify the most significant parameters.

The results of the BIC assessed regression are shown in Fig 4.13. Here, the BIC is plotted against the twenty parameters showing twenty different regression fits containing one, two, three etc. up to all twenty parameters. Each fit using between one and twenty parameters contains the parameters that give the lowest BIC for the number of parameters used. The inclusion of a parameter in the fit is shown by shading corresponding to the parameter number (1-20) on the x-axis. The intercept (continuous bar on the left of each plot labeled 'Int') is present in every fit but is not of interest in determining the importance of parameters. The shade darkens as the BIC (y-axis) of the fit improves, such that the best fit is shown across the top of each plot consisting of the intercept and the parameters used in the BIC assessed best fit. The most important parameter is the one that along with the intercept is used in every fit (easily identified as the single continuous vertical bar in each plot in Fig 4.13—e.g. parameter 19, the rain ratio Υ_c in plot A; parameter 18, the deep remineralistaion rate Rm_{deep} for plot B etc.). The next most important parameter is that used in all but one of the fits (e.g. parameter 16, the sink rate v_s in plot A), and the next, that used in all but two of the fits, and so on.

Table 4.6 lists these results. Brackets around the parameter indicate that it is not present in the best BIC assessed fit. Across all sites, the same parameters are present for each output – Υ_c, v_s and P^s_{max} for CO_2 flux, v_s and Rm_{deep} for export and α (the initial slope of the P-I curve) for primary production. Again, the results for the central sites are very similar (identical for all outputs for the 1^{st} and 2^{nd} most important parameters).

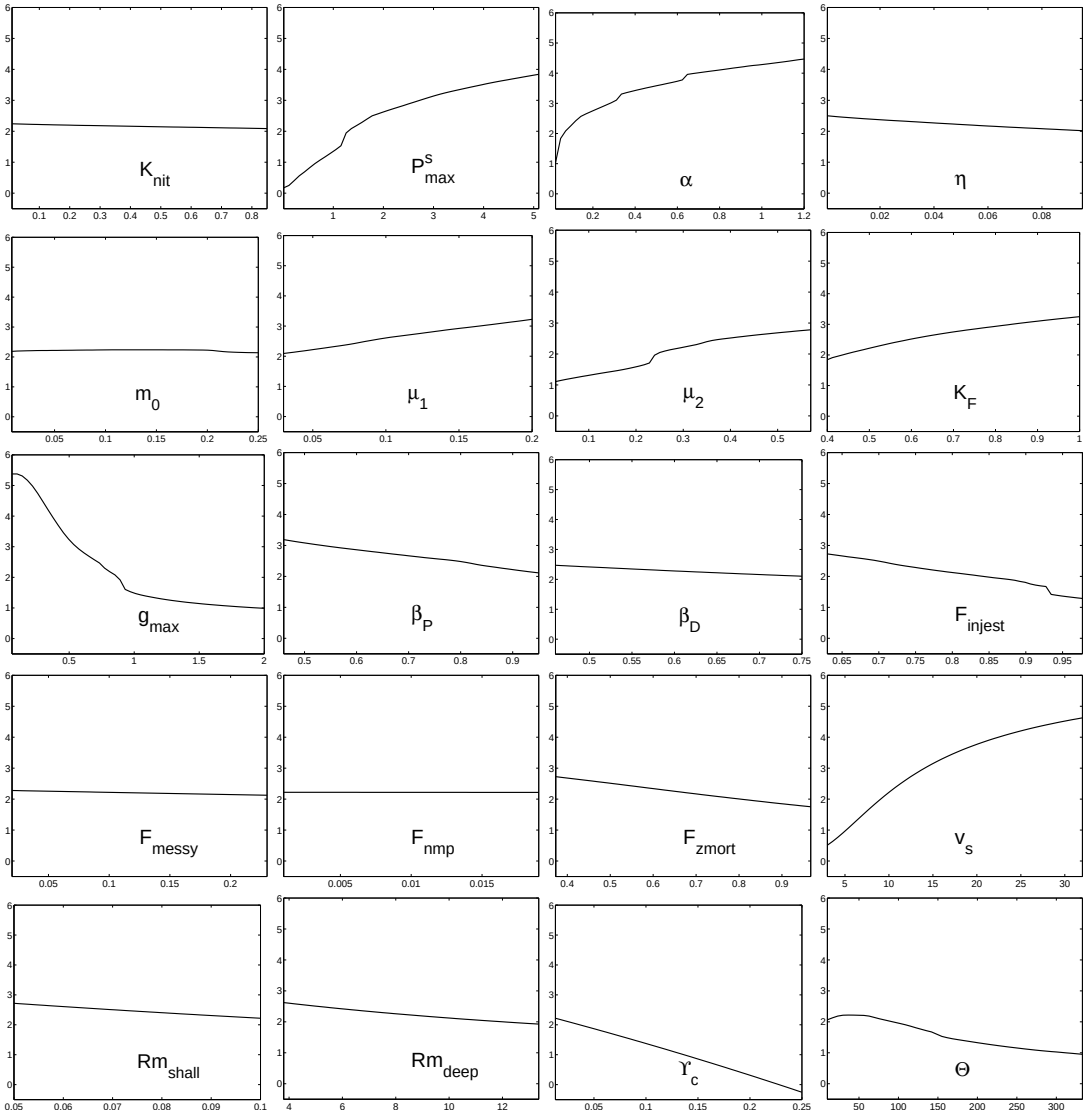

Figure 4.8: OAT plots for CO_2 flux (y-axis) in mol CO_2 m^{-2} yr^{-1}

at 30°N. The y-axis scale is the same in all plots for easy comparison of the relative effect of variation in the value of each parameter (x-axis) on the CO_2 flux. Variation in the values of P^s_{max}, α, g_{max} and v_s have the greatest effect.

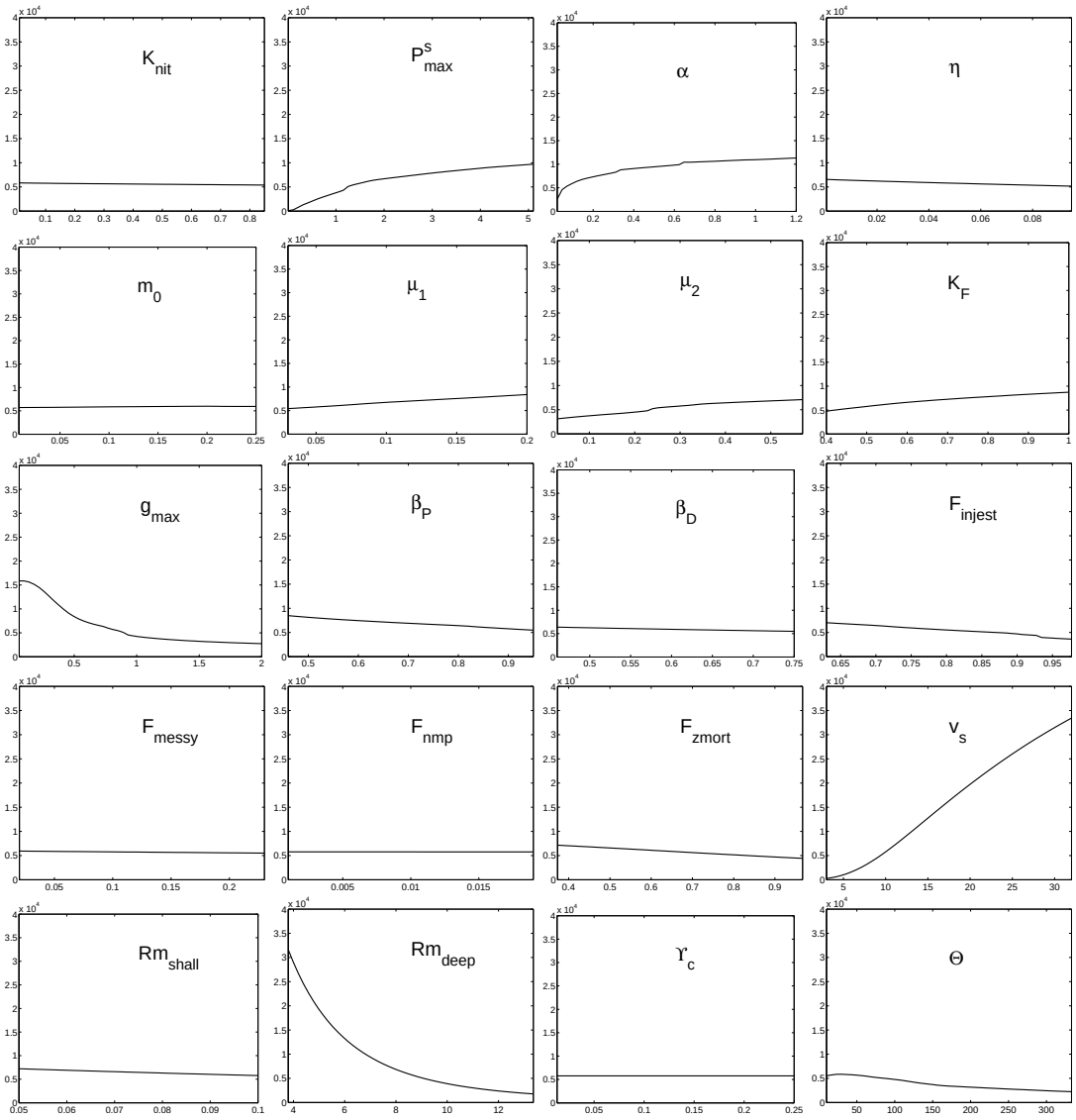

Figure 4.9: OAT plots for export (y-axis) in mgC m^{-2} yr^{-1} at 30°N. The y-axis scale is the same in all plots for easy comparison of the relative effect of variation in the value of each parameter (x-axis) on the export. Variation in the values of v_s and Rm_{deep} have the greatest effect.

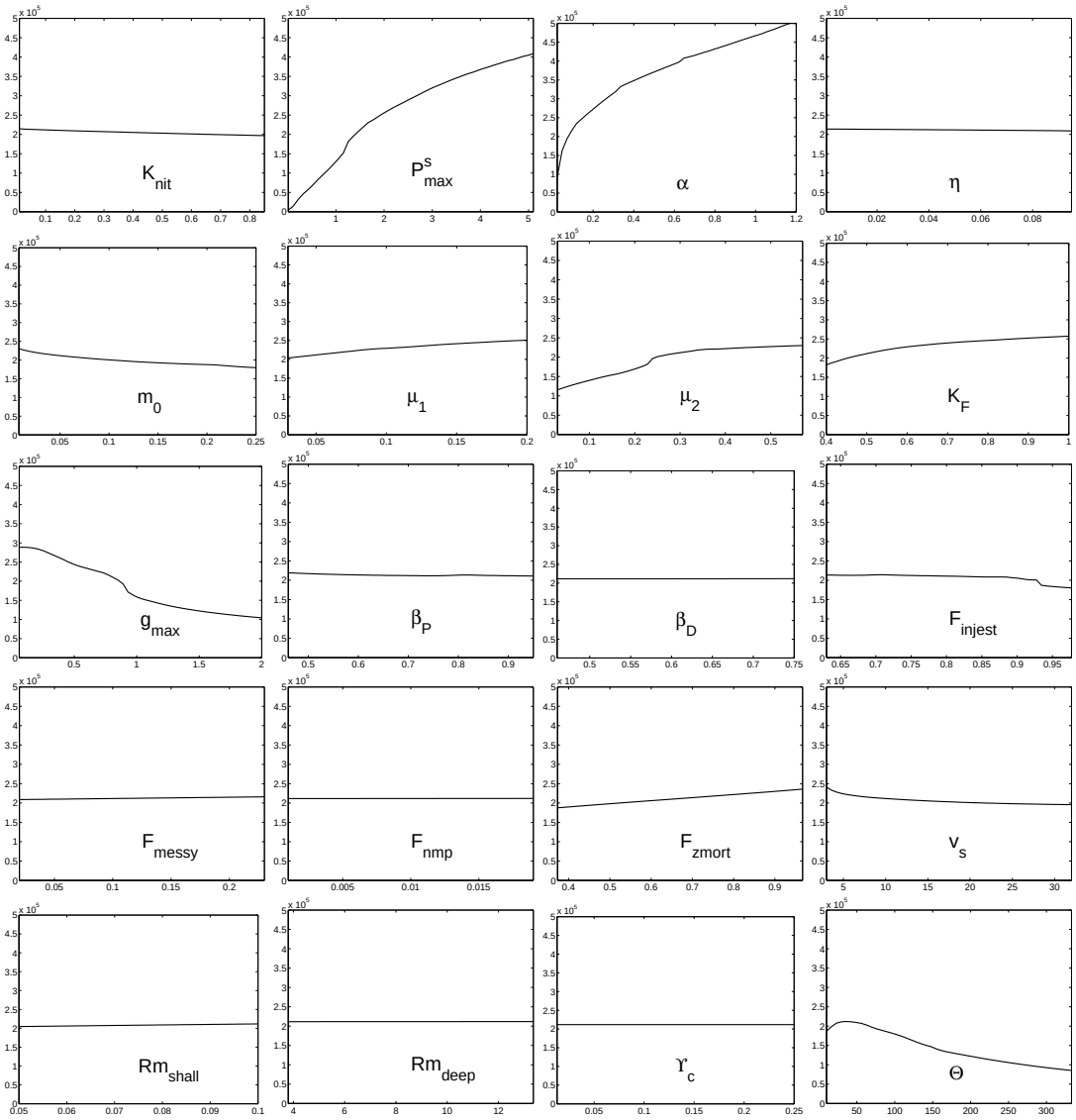

Figure 4.10: OAT plots for primary production (y-axis) in gC $m^{-}2\ yr^{-1}$ at 30°N. The y-axis scale is the same in all plots for easy comparison of the relative effect of variation in the value of each parameter (x-axis) on primary production. Variation in the values of P^s_{max} and α have the greatest effect.

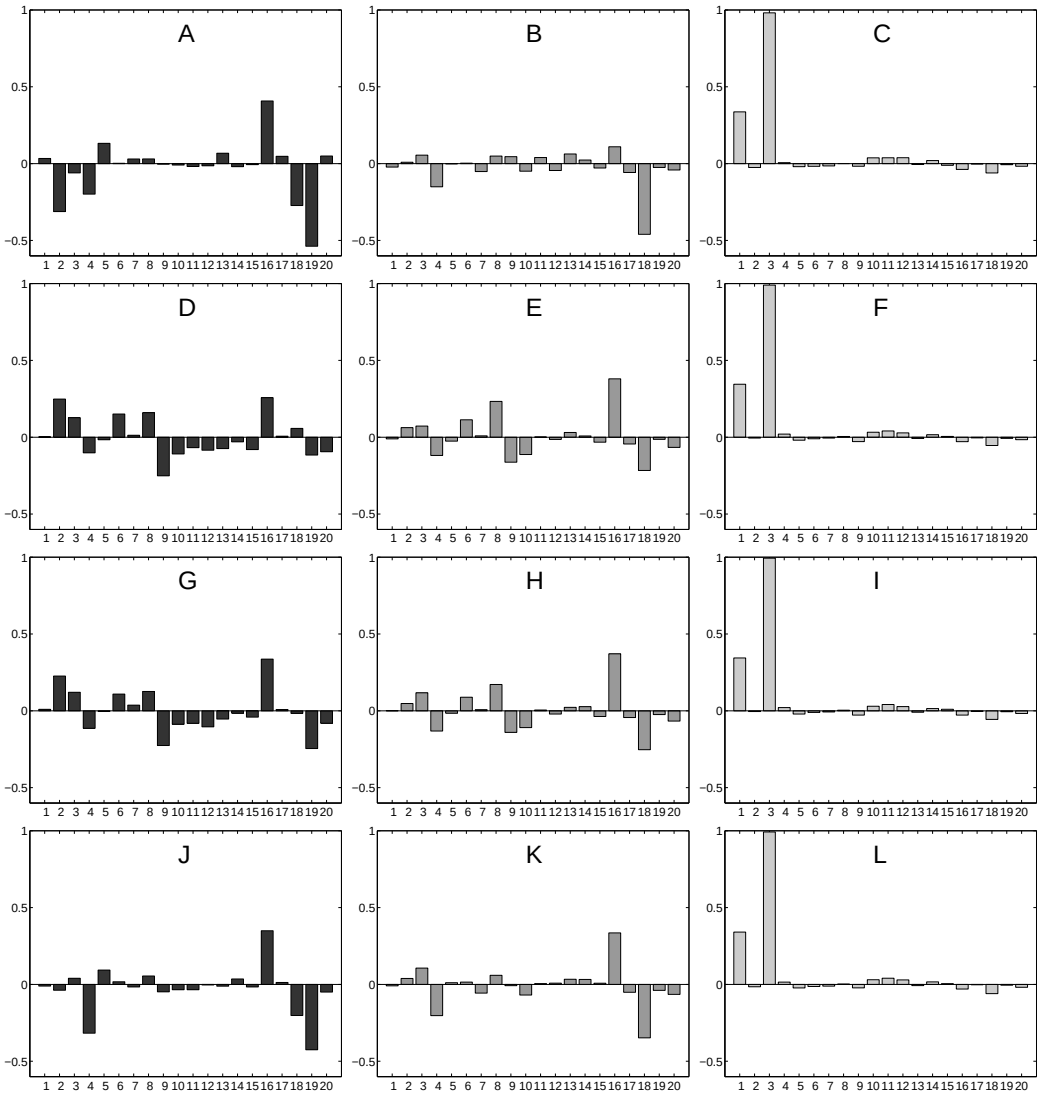

Figure 4.11: Pearson (linear) correlation of CO_2 flux (left column), export (centre column), and primary production (right column), for all sites: top to bottom 0°N (ABC), 15°N (DEF), 30°N (GHI), 45°N (JKL). Correlation is given on the y-axis and the parameters (numbered as in Table 4.3) along the x-axis.

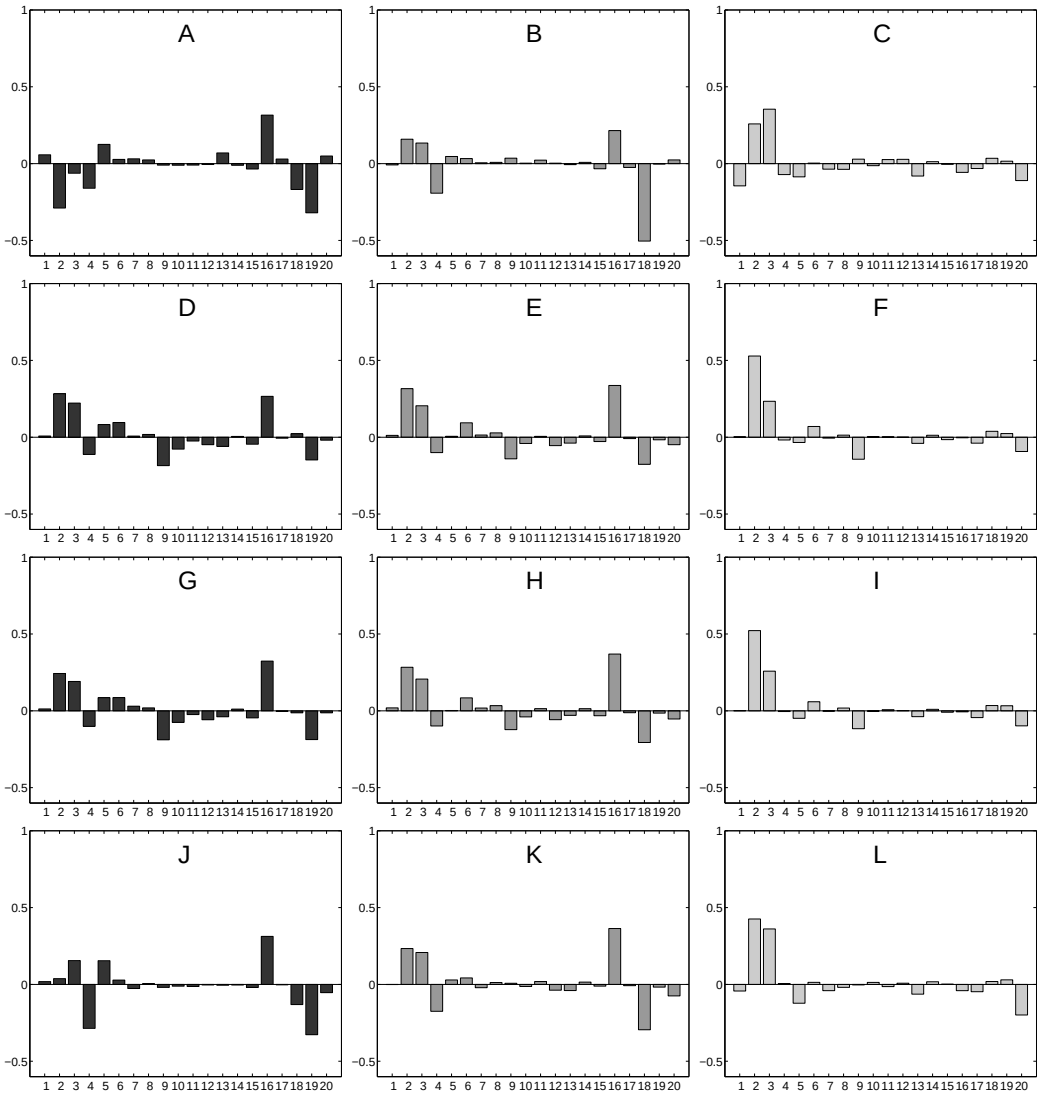

Figure 4.12: Kendall (rank) correlation of CO_2 flux (left), export (centre), and primary production (right), for all sites: top to bottom 0°N (ABC), 15°N (DEF), 30°N (GHI), 45°N (JKL). Correlation is given on the y-axis and the parameters (numbered as in Table 4.3) along the x-axis.

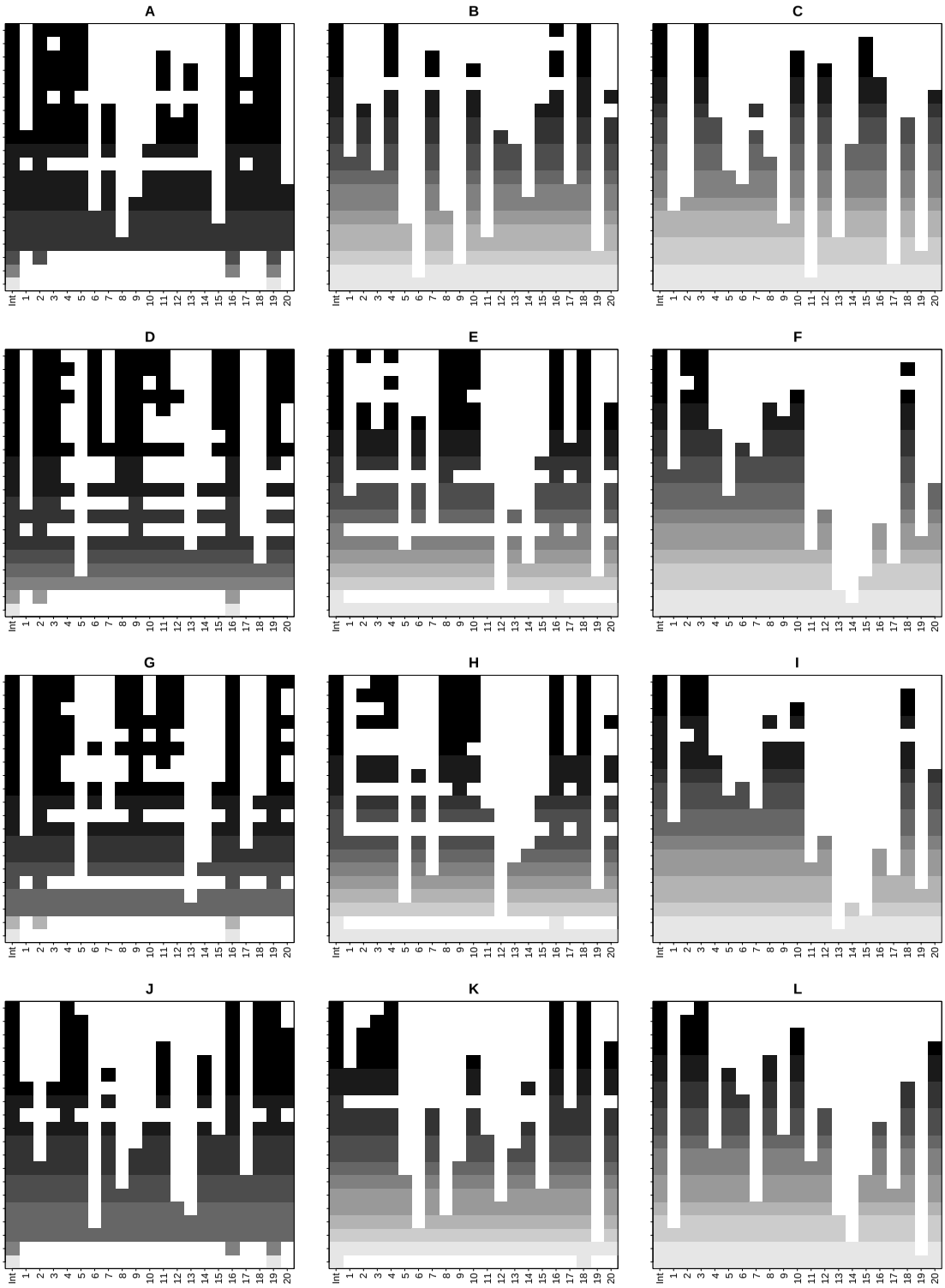

Figure 4.13: All-subset BIC regression. CO_2 flux (left column), export (centre column) and primary production (right column) for all sites: top to bottom 0°N (ABC), 15°N (DEF), 30°N (GHI), 45°N (JKL). Each plot shows the twenty best BIC-assessed regression fits containing the intercept (Int) and from one to all twenty of the parameters (numbered as in Table 4.3 along the x-axis). The shade darkens as the BIC (y-axis) improves so that the best BIC-optimised fit for each output at each location is shown across the top of each plot.

Table 4.6: BIC regression fit. Parameters listed in order of importance for each output in the BIC assessed fit (parameters in column 1 are the most important). Brackets around a parameter indicate that the parameter is not included in the BIC assessed best fit but are listed here (where relevant), as other important parameters and for comparison with results for the other sites. Eleven of the orginal twenty parameters are present in the best fit for CO_2 flux at 15°N 30°W, while only two parameters (α and P^s_{max}), are used in the best fit for primary production at this location.

Output	Site	1	2	3	4	5	6	7	8	9	10	11
CO_2 flux	0°N	Υ_c	v_s	P^s_{max}	Rm_{deep}	η	m_0	β_D	-	-	-	-
	15°N	v_s	P^s_{max}	g_{max}	K_F	Υ_c	μ_1	F_{zmort}	β_D	Θ	β_P	η
	30°N	v_s	P^s_{max}	Υ_c	g_{max}	α	β_D	K_F	F_{injest}	η	Θ	-
	45°N	Υ_c	v_s	η	Rm_{deep}	(m_0)	(Θ)	(β_D)	(F_{nmp})	(μ_1)	-	-
Export	0°N	Rm_{deep}	η	v_s	(μ_2)	(β_P)	(Θ)	(P^s_{max})	-	-	-	-
	15°N	v_s	Rm_{deep}	K_F	g_{max}	β_P	η	P^s_{max}	-	-	-	-
	30°N	v_s	Rm_{deep}	g_{max}	K_F	β_P	η	α	-	-	-	-
	45°N	v_s	Rm_{deep}	η	(α)	(P^s_{max})	(Θ)	(β_P)	-	-	-	-
Prim. prod.	0°N	α	(F_{zmort})	(β_P)	(F_{injest})	(v_s)	-	-	-	-	-	-
	15°N	α	P^s_{max}	(Rm_{deep})	(β_P)	(K_F)	-	-	-	-	-	-
	30°N	α	P^s_{max}	(Rm_{deep})	(β_P)	(K_F)	-	-	-	-	-	-
	45°N	α	(P^s_{max})	(β_P)	(Θ)	(K_F)	(m_0)	-	-	-	-	-

4.4.4 Regression results discussion

The results are as expected from the OAT and correlation results. The CO_2 flux is sensitive to Υ_c, the parameterisation of carbonate formation as a proportion of nutrient uptake, v_s the detrital sinking rate, and P^s_{max} the maximum rate of photosynthesis. These are parameters that influence the pCO_2 of the ocean surface and hence the air-sea CO_2 exchange by altering the DIC content of the sea-surface level. Υ_c directly changes the DIC concentration (and the alkalinity), by controlling the release of organic carbon to DIC through carbonate formation (Equations 3.17 and 3.18). P^s_{max} changes the DIC through controlling its uptake by phytoplankton growth. v_s exports detritus away from the sea-surface level which directly influences the DIC concentration (Equation 3.17), and by removing detritus that might remineralise and contribute to nutrient, the alkalinity (Sections 3.2.5 and 3.2.7). The recent results of Schneider et al. [2008], using the more complex PISCES model, corroborate the importance of the parameterisation of particulate sinking on the calculation of the surface pCO_2 and resulting CO_2 flux. Export is sensitive to parameters that govern the creation and transport of detritus: the detrital sinking rate v_s, Rm_{deep} the parameterisation of remineralisation of detritus below 100m in the water column, and the zooplankton grazing parameters K_F—the half saturation constant for grazing and g_{max}—the maximum grazing rate, which control the amount of detritus eaten by zooplankton (Sections 3.2.3 and 3.2.4). Primary production is sensitive to the parameters that control phytoplankton growth: α, P^s_{max} and m_0 (the phytoplankton-specific mortality rate), as has been found in previous studies such as Druon and Le Fèvre [1999]. α is more important than P^s_{max} as phytoplankton growth is light limited through the column. At the well-lit surface, P^s_{max} is more important in limiting phytoplankton growth so has greater influence on the calculation of CO_2 flux.

The BIC-optimised regression also shows how many of the original twenty parameters are essential to control the output. In Fig. 4.13, CO_2 flux is seen to be dependent on up to half the parameters under study, with between four (at 45°N Fig. 4.13 plot J) and eleven (at 15°N Fig. 4.13 plot D) parameters used in the best BIC fit, while export depends on three to seven and primary production on one or two. This indicates that CO_2 flux is probably the most difficult of these three outputs to obtain accurately with NPZD models. The inclusion of second order terms in the regression did not identify any other parameters as being more important than those detailed here.

4.5 An alternative approach: using the GEM-SA sensitivity analysis package

The results of a sensitivity analysis are to some extent dependent on the methods chosen for each stage of the SA discussed in 2.3. To provide a comparison to the results presented above, the GEM-SA SA package—see Section 2.4.4—is used. This calculates the variance in the output attributable to the variation in each individual parameter, and the total effect of each parameter

(the indiviudal effect plus interactions with all other parameters). Here, in contrast to the previous method, the 5% and 95% confidence values are used as the absolute limits for the parameter range, and a uniform probability distribution for all parameters across their given range is assumed. 200 parameter sets are generated and used to run HadOCC-GOTM at the four test sites. The outputs of air-sea CO_2 flux, export and primary production are recorded and returned to GEM-SA to train the emulator on which the SA is performed.

4.5.1 Results of GEM-SA analysis

Fig. 4.14 shows the individual contributions (normalised by the variance) of each parameter to the output variance. Fig. 4.15 shows the total effect (normalised by the sum of the total effects) of each parameter to output variance. The results are reasonably similar across all the sites, with greater similarity between the central sites as before. At all sites the individal effects and interactions account for $\sim$ 90% of the output variance for each of the different outputs showing that GEM-SA successfully emulates the model. At 0°N, 15°N and 30°N greater than 60% of the output variance is explained for all outputs by the individual contributions, while at 45°N greater than 80% is explained.

The $\sum_{i=1}^{19} i = 190$ possible pair-wise interactions between parameters account for the rest of the explained output variance. For all outputs at all sites the majority of these interactions have a value of $\ll$ 1% of the output variance. While the sum of the interactions is a non-negligible contribution to output variance, very few of the interactions are individually important. This is confirmed by the similarity between Figs. 4.14 and 4.15, where parameters with large independent contributions to the output variance (Fig. 4.14) are the same parameters that have a large total effect (Fig. 4.15). No interactions contribute more than 2-3% for CO_2 flux. For export, the most important interaction is that between v_s and Rm_{deep}—at 0°N, and 30°N and 45°N $\sim$ 6%, an expected interaction (v_s regulates the speed of detrital sinking and hence the amount of detritus that reaches depths below 100m, at which Rm_{deep} controls the rate of detrital breakdown). For primary production, the interaction between α and Θ is $\sim$ 12% at 0°N, $\sim$ 4% at 15°N and 30°N and $\sim$ 2% at 45°N. The ratio of these two parameters is used in the estimation of the light limitation on photosynthesis (see Section 3.2.1).

4.6 Comparison of SA techniques

The results of the regression analysis are now compared with those of the GEM-SA analysis. Table 4.7 shows the parameters that have a total effect of 5.0 or greater in Fig. 4.15, listed in order of the size of their total effect. Comparing Table 4.7 and Fig. 4.15 with the results of the regression in Table 4.6, most of the same parameters are found to be important (though the order is different), and the same parameters are generally shown to have low significance—F_{injest}, F_{messy}, F_{nmp} and F_{zmort} (and to a lesser extent β_P and β_D). This is to be expected from the OAT plots in Figures 4.8, 4.9 and 4.10 where it can be seen that variation in values of the assilimation efficiency parameters β_P and β_D, and in the values of the feeding fraction parameters F_{injest}, F_{messy}, F_{nmp} and F_{zmort} does not cause much change to the outputs (CO_2 flux, export and primary production).

The major difference is the presence and high contribution of Θ—the carbon to chlorophyll ratio of phytoplankton—for almost all the outputs and sites in the GEM-SA analysis (excepting CO_2 flux at 0°N 30°W), whereas it only appears (in 9^{th} and 10^{th} position) for the CO_2 flux at the central sites in the BIC analysis. This results from the use of a uniform distribution in GEM-SA which gives much greater weight to values of Θ close to the upper limit than the Davies distribution used in the regression analysis. The other parameter given greater overall prominence by GEM-SA is the phytoplankton mortality rate m_0, where high values are given much greater prominance by the uniform prior (the Davies distribution gives greater weight to lower values as the HadOCC value used for the central Davies parameter is much closer to the lower limit).

The carbon to chlorophyll ratio of phytoplankton Θ is not fixed as set here in HadOCC, but is in fact highly dynamic, changing from ~ 20 to ~ 200 over a 24 hour period [Geider et al., 1998]. To reflect this some models of the ocean ecosystem such as that of Geider et al. [1998] do not fix the value of the carbon to chlorophyll ratio and allow it to vary according to environmental conditions. While GEM-SA has probably overestimated its importance through the equal weighting of very high values (the nominal HadOCC value of 40 is closer to the lower limit), it remains a key parameter in governing the carbon uptake by phytoplankton in biogeochemical models.

The importance of m_0 however, is overestimated by GEM-SA as the majority of values used in the literature (Table 4.2) are equal to or smaller than the HadOCC value of 0.05 d^{-1} (mMol N $m^{-3})^{-1}$, which is much better represented by the Davies distribution used in the regression analysis (see Figure 4.7). By contrast, the uniform distribution used in GEM-SA gives the same importance to the very high phytoplankton mortality rate of 0.1-0.25 d^{-1} (mMol N $m^{-3})^{-1}$ from Waniek and Holiday [2006] as to all other possible values. Looking back at Table 4.1 it can be seen that all the other literature values for the phytoplankton mortality rate are much lower ($m_0 \leq 0.05$)—a fact that is well represented by the prior used for the regression analysis (see Figure 4.7) generated by the Davies distribution.

For CO_2 flux, both analyses in general highlight the importance of v_s and Υ_c, with g_{max} and P^s_{max} also present at most sites in both analyses. As expected, both sets of results for export give high significance to Rm_{deep} and v_s, while all the primary production results give high sensitivity to either or both of P^s_{max} and α.

Both SA approaches used here give results that appear reasonable, and the differences between them can be explained in terms of the assumed prior parameter dsitributions. Though it adds complexity to the exercise, the use of non-uniform probability distributions without fixed limits (as used in the regression analysis) is arguably much more realistic in representing the true spread of possible parameter values than the uniform distribution used in GEM-SA and elsewhere [Saltelli et al., 2001]. While the analysis methods performed by GEM-SA are more advanced than those used in the regression, the relatively simple (largely monotonic) nature of the response of the outputs to parameter variations (see the OAT plots in Figures 4.8, 4.9 and 4.10, and correlations in Section 4.4.2) makes the methods used in the regression analysis entirely appropriate. As explored here, the ability of the regression to use non-unifrom parameter priors is advantageous to this work. As a result of these considerations, there is greater overall confidence in the results of the regression analysis, and it is these results that will be used in the subsequent exploration of the effect of HadOCC parameter perturbations on the behaviour of the ocean ecosystem in the FAMOUS GCM in Chapter 5.

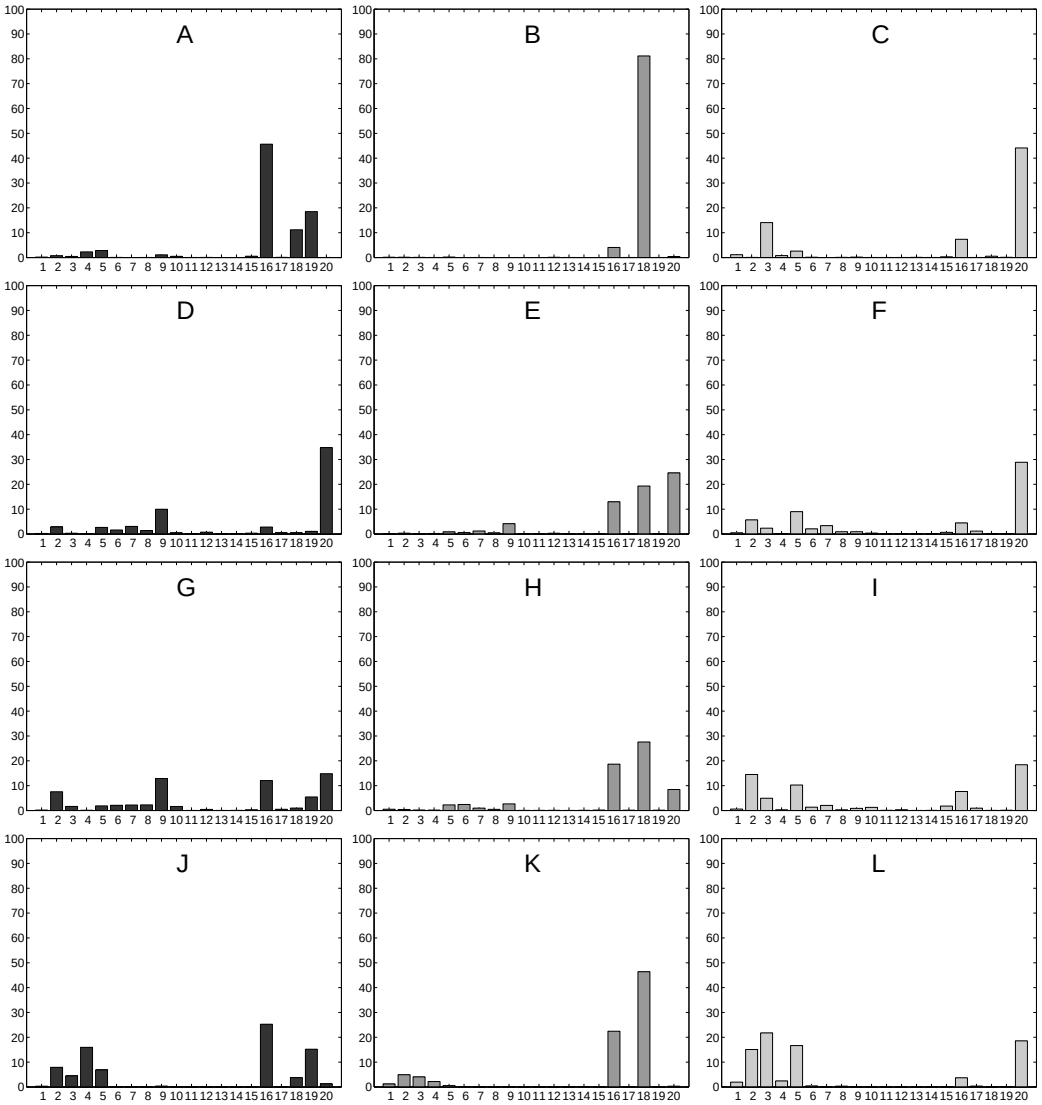

Figure 4.14: Results from GEM-SA analysis: percentage of the output variance explained by variation in each parameter. CO_2 flux (left column), export (centre column) and primary production (right column), for all sites: top to bottom 0°N (ABC), 15°N (DEF), 30°N (GHI), 45°N (JKL). Percentage is given on the y-axis and the parameters (numbered as in Table 4.3) along the x-axis.

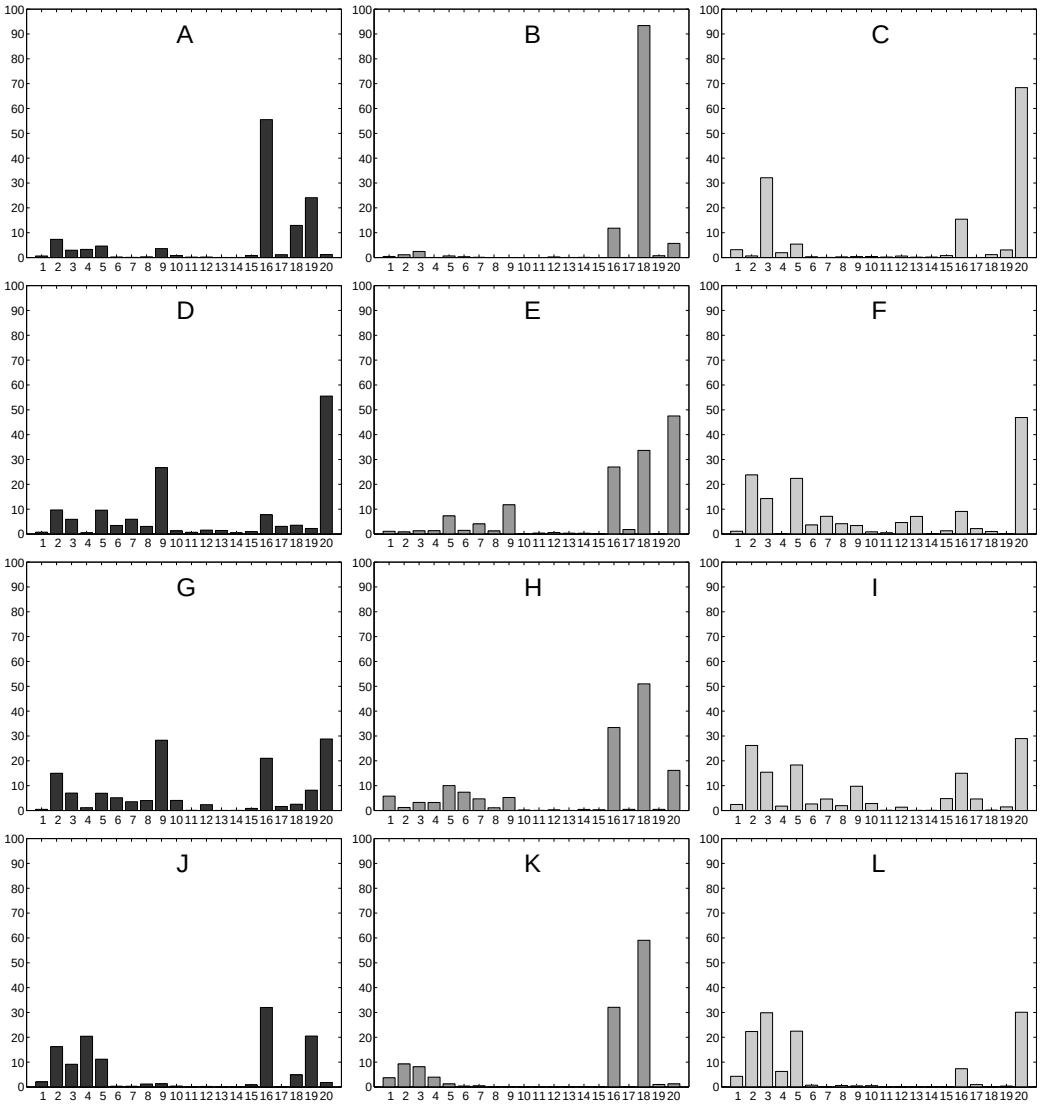

Figure 4.15: Results from GEM-SA analysis: total effect of variation in each parameter on the variance in output. CO_2 flux (left column), export(centre column) and primary production (right column), for all sites: top to bottom 0°N (ABC), 15°N (DEF), 30°N (GHI), 45°N (JKL). Total effect is given on the y-axis and the parameters (numbered as in Table 4.3) along the x-axis.

Table 4.7: GEM-SA total effect results (Fig. 4.15) with parameters listed in order of greatest overall contribution to variation in the output. The five parameters with the greatest total effect are in columns 1-5, other parameters that have total effect of 5.0 or greater listed in order in the 'others' column, c.f. Table 4.6.

Output	Site	1	2	3	4	5	others with total effect > 5
CO_2 flux	0°N	v_s	Υ_c	Rm_{deep}	P^s_{max}	-	-
	15°N	Θ	g_{max}	P^s_{max}	m_0	v_s	μ_2, α
	30°N	Θ	g_{max}	v_s	P^s_{max}	Υ_c	α, μ_1
	45°N	v_s	Υ_c	η	P^s_{max}	m_0	α
Export	0°N	Rm_{deep}	v_s	Θ	-	-	-
	15°N	Θ	Rm_{deep}	v_s	g_{max}	m_0	-
	30°N	Rm_{deep}	v_s	Θ	m_0	μ_1	K_{nit}, g_{max}
	45°N	Rm_{deep}	v_s	P^s_{max}	α	-	-
Prim. prod.	0°N	Θ	α	v_s	m_0	-	-
	15°N	Θ	P^s_{max}	m_0	α	v_s	μ_2, F_{messy}
	30°N	Θ	P^s_{max}	m_0	α	v_s	g_{max}
	45°N	Θ	α	m_0	P^s_{max}	v_s	η

4.7 Discussion

The parameters identified here to be important for the calculation of CO_2 flux, export and primary production are mostly parameters that are generic to NPZD model designs (c.f. Table 4.1 with Tables 4.6 and 4.7). Encouragingly, the less generic HadOCC parameterisations of zooplankton feeding processes (F_{injest}, F_{messy}, F_{nmp} and F_{zmort}) are shown in general not to have such a significant effect. The parameters identified to have greatest influence on the outputs do not change from site to site—their importance is shown to be generally independent of the different physical and chemical forcings used in this study. These results agree with those found in similar studies of other ocean biogeochemical models, such as the work of Druon and Le Fèvre [1999].

It is shown in Table 4.5 that variation in the values of these parameters within reasonable ranges has a major effect on the calculation of the CO_2 flux, export and primary production (see also Frenette et al. [1993]; Fennel et al. [2001]). Accurate calculation of these processes is important to modelling the ocean's role in global chemical cycling and hence its effect on climate. Here, the calculation of these processes has been shown to be highly linearly dependent on the value of certain parameters. As such, it is theoretically possible given sufficient data to tune these parameters to produce an accurate global bulk estimate of a desired quantity—indeed NPZD models (including HadOCC) can reasonably reproduce large-scale estimates of chlorophyll and primary production [Palmer and Totterdell, 2001; Kawamiya et al., 2000].

Looking at the identified significant parameters, there is much variation in the values prescribed (see Table 4.1), which come from both direct measurement and tuning models to avilable data. The application of a single value for a parameter such as the maximum photosynthetic rate P^s_{max} across the whole ocean as in HadOCC inevitably introduces geographically varying biases which this analysis suggests will be significant. The rapid development of remote sensing techniques (e.g. Hirata et al. [2008] and Nair et al. [2008]) may enable the derivation of regional phytoplankton parameter values from ocean colour measurement, though this work shows that several of the key controls of the ocean biogeochemistry and air-sea CO_2 flux are parameterisations of sub-surface effects, such as detrital sinking and deep bacterial remineralisation, which cannot be observed remotely and would hence remain uncertain unless methods were developed to allow their derivation from ocean surface data.

However, tuning the parameters of a simple NPZD model to the present situation does not necessarily enable the model to inform upon potential future changes to the ecosystems biochemical role arising from alteration to it's behaviour due to environmental change. Given that the parameter values used in this work arise from many different ocean regions and their local environments it is clear that such changes may have significant effects. Addressing this issue demands the further refinement of ocean biogeochemical models, particularly of the parameterisations identified here and elsewhere to have the potential to significantly effect the ecosystems growth and resulting chemical behaviour. Approaches to this problem include the

use of structurally more complex phytoplankton fuctional type (PFT) models such as that of Le Quéré et al. [2005] and the use of trait-based emergent-community modelling methods such as those used by Follows et al. [2007] (see also Litchman et al. [2007]). While representing an ideal successor to NPZD models, PFT models currently suffer similar problems of parameter uncertainty to NPZD models arising from our limited understanding of ocean the ocean ecosystem [Hood et al., 2006; Anderson, 2005; Flynn, 2006; Le Quéré, 2006] (see Section 1.8.1). In this respect, the emergent-behaviour approach used in Follows et al. [2007], in which the ecosystem structure evolves from competition between large numbers of members with stochastically assigned characteristics has obvious attractions in bypassing the necessity for the accurate measurement of key biological parameters, and in doing so can potentially highlight key traits that require inclusion in more complex structure-determined ecosystem models.

4.8 Summary

Variation in the values of the biological parameters used in the HadOCC NPZD ocean biogeochemical model has been shown to have a large effect on the calculation of three fundamental outputs for biogeochemical modelling and climate prediction (air-sea CO_2 flux, export and primary production). The parameters of greatest importance are generally those that are generic to most NPZD models. Parameters controlling biological carbonate formation, detrital sinking and phytoplankton growth at the ocean surface have the greatest influence on the air-sea CO_2 flux. Export is most influenced by detrital sinking, bacterial remineralisation and zooplankton grazing parameters. Parameters that control phytoplankton growth (the inital slope of the P-I curve α_{white}, the maximum photosynthetic rate P^s_{max}, and the carbon to chlorophyll ratio Θ) are most important in the calculation of primary production. Most of these parameters are poorly constrained and while some may be derivable by satellite-based remote sensing, others represent processes beneath the observable surface layer on which data is severely limited. The skill of ocean biogeochemistry models is limited by the availability of data to constrain the parameters governing ocean ecosystem processes. Here, the parameters are indentified which need greater investigation to improve ocean biogeochemistry models, and are possibly important for the accurate prediction of the role of the ocean ecosystem in the ocean carbon cycle in an ocean altered by anthropogenic activity.

Experiments using the FAMOUS GCM

5.1 Overview

In this chapter, the FAst Met Office and Universities Simulator (FAMOUS) GCM [Smith et al., 2008] is used to explore the effect of uncertainty in the sensitive biogeochemical parameters identified in Chapter 4 on global calculations of air-sea CO_2 flux. FAMOUS is a lower-resolution, fast-running GCM, which uses much of the same code, and is tuned to reproduce the results of its parent, the widely used HadCM3 GCM (see Section 3.4). Exploring the effects of parameter uncertainty on the predictions of GCMs has become an essential part of climate science (e.g., Murphy et al. [2004] and Randall et al. [2007]). However, performing large ensembles of perturbed GCM runs requires huge computing resources, such as those used for the widely publicised `climateprediction.net` project detailed in Stainforth et al. [2005]. Here, only the effects of perturbations to the value of the three most sensitive parameters—the detrital sink rate: v_s, the maximum rate of photosynthesis: P^s_{max} and the rain ratio: Υ_c (see Section 3.2.8)—on the calculation of the air-sea CO_2 flux are explored due to limited computing resource availability. Additionally, I use the same runs to investigate the effect of the perturbation of the maximum rate of photosynthesis on the primary production in FAMOUS, and the effect of the perturbation of the detrital sink rate on detrital export in FAMOUS.

The perturbation of these key parameters causes changes to the behaviour (growth and resulting biochemical effect) of the ecosystem. These changes in behaviour alter the cycling of carbon in the ocean and as a result the air-sea CO_2 flux, and aslso change the use and supply of nutrient. To fully equilibrate changes to the cycling of carbon and nutrient in the ocean requires the surface and deep ocean to fully mix—a timescale of around one thousand years. Here, FAMOUS is perturbed for one hundred years to explore the short-term effect of changes in ocean ecosystem behaviour on the air-sea CO_2 flux, primary production and detrital export. A single perturbed FAMOUS run is also extended to just over one thousand years to explore the long-term effect.

5.2 Parameter selection and perturbation

The three HadOCC parameters shown to have the greatest effect on the calculation of air-sea CO_2 flux in the 1D HadOCC-GOTM experiments in Chapter 4 are the detrital sink rate: v_s, the maximum rate of photosynthesis: P^s_{max} and the rain ratio: Υ_c. Variation in the value of these parameters changes the influence of the ocean biology by uptake or release on the inorganic carbon concentration, changing the pCO_2^{sea} of the ocean surface level and altering the air-sea CO_2 flux. The detrital sink rate (v_s) affects the air-sea CO_2 flux through the export of detritus away from the surface. Detritus breaks down to form DIC and nutrient, so changing the rate at which detritus is removed from the sea-surface level alters the surface DIC concentration. The maximum photosynthetic rate (P^s_{max}), controls the growth of phytoplankton in the light-bathed ocean surface provided nutrient is available, thus controlling the uptake of dissolved carbon which changes the pCO_2^{sea} of the ocean surface. The rain ratio (Υ_c) implicitly parameterises the formation of carbonate by calcifiers such as coccolithophores. Calcification releases organic carbon, changing the DIC concentration and hence the surface ocean pCO_2^{sea}. The effects of these parameters are discussed in more detail in Section 4.4.4.

Due to limited time with the ECDF computing facility, only a few runs using perturbed HadOCC parameters are possible. In Chapter 4 is is found that changes in the value of v_s and P^s_{max} are positively correlated, and that changes in the value of Υ_c are negatively correlated with the change in air-sea CO_2 flux. From this, and consideration of the role of each of the parameters in HadOCC, it is expected that perturbing the values of v_s and P^s_{max} in FAMOUS will change the calculated CO_2 flux in the direction of the perturbation (increasing the value of v_s and P^s_{max} will increase the CO_2 flux into the ocean), while perturbing the value of Υ_c will cause a change to the CO_2 flux in the opposite direction to the perturbation (increasing the value of Υ_c will decrease the CO_2 flux into the ocean).

In Chapter 4, the possible ranges for the HadOCC parameters were established from the literature and expert opinion (summarised in Tables 4.1 and 4.3). The values of the HadOCC parameters used in FAMOUS job xdbua differ slightly from those used in the unperturbed HadOCC-GOTM. Of the three parameters investigated here, v_s has a value of 10 m d^{-1} in both HadOCC-GOTM and FAMOUS, the value of P^s_{max} is 1.5 in HadOCC-GOTM and 0.6 in FAMOUS, and Υ_c has a value of 0.013 in HadOCC-GOTM and 0.007 in FAMOUS. FAMOUS is designed to duplicate the results of the HadCM3 GCM, so for possible comparison of the results of this work with other work undertaken on GCM parameter sensitivities, the parameter values used in FAMOUS are kept as the initial values from which pertubations are established.

For the SA work in Chapter 4, the maximum and minimum values for each parameter were used as confidence intervals for the range of possible values. For FAMOUS, with a limited number of model runs possible, the degree to which each of the three parameters is perturbed needs to reflect the uncertainty in the value of the parameter, but not be a perturbed value that, although

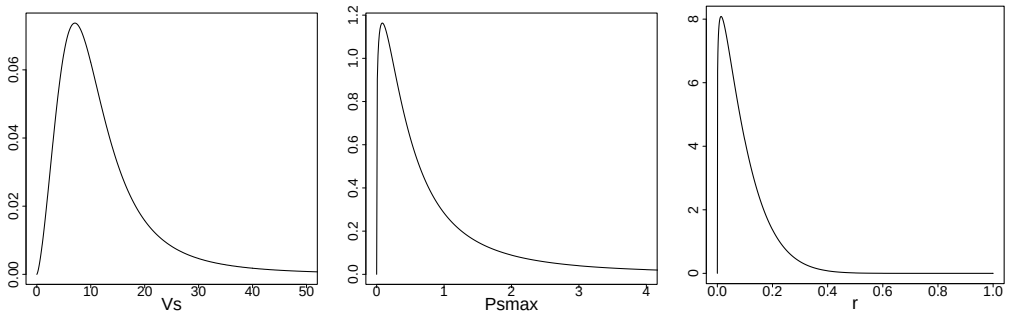

Figure 5.1: Priors used to establish perturbations in FAMOUS for v_s (Davies distribution), P^s_{max} (Davies distribution), and Υ_c (Beta distribution).

Table 5.1: Perturbed values for FAMOUS parameters, calculated as the 25^{th} percentile and 75^{th} percentile of the priors shown in Figure 5.1. Only the 75% value is given for Υ_c as the FAMOUS value for this parameter is smaller than both the percentiles (see text Section 5.2).

Parameter	Units	FAMOUS value	Distribution	25%ile	75%ile
v_s	m d^{-1}	10	Davies	6.36	15.38
P^s_{max}	d^{-1}	0.6	Davies	0.11	1.12
Υ_c	-	0.007	Beta	-	0.13

possible, is at the limits of the plausible range and hence unlikely to accurately represent the real phenomenon. To achieve this, the prior distributions used in Chapter 4 (Section 4.2.3) are revisited. For the SA, the minimum and maximum literature values were used as 5% and 95% confidence intervals, along with the nominal model value to establish priors from which the parameter values were selected. For v_s and P^s_{max}, a Davies distribution [Hankin and Lee, 2006] was used, and for Υ_c, a Beta distribution [Freund, 1992], as these distributions were appropriate to the fundamental properties of these parameters (see Section 4.2.3). For FAMOUS, the same distributions are used to establish priors, with those for P^s_{max} and Υ_c adjusted to use the parameter values used in FAMOUS (see Figure 5.1). The 25^{th} and 75^{th} percentiles of these distributions are then used as the perturbed parameter values in FAMOUS. Table 5.1 shows the perturbed parameter values calculated using this method. For v_s and P^s_{max}, this gives values lesser and greater than the present FAMOUS value, but for Υ_c, since the FAMOUS value is lower than any other literature values found, both the 25% and 75% values are greater, so only the 75% value is used.

5.3 FAMOUS set up

For this work, the well spun-up FAMOUS job xdbua[1], as detailed in Smith et al. [2008] (see Section 3.4) was ported to Edinburgh and adapted to investigate the effect of ocean biogeochemical parameter uncertainty on air-sea CO_2 flux. FAMOUS is run on the Edinburgh University Edinburgh Compute and Data Facility (ECDF) computing cluster (`www.ecdf.ed.ac.uk`), enabling a run time of approximately one model year, per ten wallclock minutes. The wind speed gas exchange parameterisation is the widely used, though possibly outdated [Wanninkhof and McGillis, 1999; Fangohr et al., 2008], Wanninkhof '92 quadratic relationship [Wanninkhof, 1992], as used in HadOCC-GOTM in Chapter 4.

An exact copy of FAMOUS job xdbua [Smith et al., 2008] is run on ECDF for one hundred years[2], (Unified Model (UM) job code xdnzh), to check that the results of FAMOUS run on ECDF are comparable to those from other high performance computing facilities. Job xdnzh is then used as the unperturbed control run (hereafter refered to in the text as job F_0), against which the results of jobs with perturbed HadOCC parameters are compared. All perturbed jobs, and the unperturbed job F_0, are started from the well spun-up job xdbua [Smith et al., 2008] dump files for the model year 6804. The ancillary reference time for all FAMOUS jobs used here is set to be the 1st December 1849 as in job xdbua.

FAMOUS job xdbua has a constant pCO_2^{air} of 290 ppm, the approximate atmospheric CO_2 concentration of the 1850's. The carbon cycle is not fully coupled, so changes in the air-sea CO_2 flux do not alter the atmospheric CO_2 concentration or the pCO_2^{air} 'seen' by the ocean surface. The net global surface pCO_2^{sea} of the ocean in the well spun up FAMOUS job xdbua of Smith et al. [2008] is in equilibrium with the atmosphere, so the net global air-sea CO_2 flux is near zero. This means that FAMOUS job xdbua has a constant ocean DIC content which is in global equilbrium with the atmosphere [Smith, 2009] (see Section 3.4.2). Changing the oceans ability to uptake CO_2 from the atmosphere will temporarily alter the net global air-sea CO_2 flux as the ocean reacts by either absorbing or releasing CO_2 until the DIC content (and hence the pCO_2^{sea}) returns to equilibrium with the atmosphere. The interpretation and limitations arising from this arrangement are discussed further in Sections 5.5, 5.7, 5.7.1 below.

5.4 FAMOUS runs

FAMOUS is run as described above in Section 5.3 for one hundred years, with the HadOCC parameter perturbations as detailed in Table 5.1. Mean decadal and annual air-sea CO_2 flux data is output for study. In order to more closely investigate the initial effects of the parameter pertur-

[1] xdbua is the National Centre for Atmopheric Sciences (NCAS) Unified Model job code.

[2] While theoretically running FAMOUS for one hundred years should take less than one day on ECDF, as it is heavily used by many other projects each one hundred year run took around one week to complete.

Table 5.2: Details of FAMOUS runs listed by job code. The perturbations used in each run are as detailed in Table 5.1. The output is mean air-sea CO_2 flux for the period stated: decadal, annual, monthly.

UM job code	Description	Run length (yrs)	Output		
			decadal	annual	monthly
xdbua	Smith et al. [2008]	-	-	-	-
xdnzh	F_0 (as xdbua)	100	Y	Y	N
xdsic	v_s & P^s_{max} $\uparrow$	100	Y	Y	N
xdsid	v_s $\uparrow$	100	Y	Y	N
xdsie	P^s_{max} $\uparrow$	100	Y	Y	N
xdsif	Υ_c $\uparrow$	100	Y	Y	N
xdsig	P^s_{max} $\downarrow$	100	Y	Y	N
xdsih	v_s $\downarrow$	100[a]	Y	Y	N
xdutc	F_0m (as xdbua)	5	N	Y	Y
xduta	v_s $\uparrow$m	5	N	Y	Y
xdutb	P^s_{max} $\uparrow$m	5	N	Y	Y
xeifd[b]	v_s $\uparrow$	1080	N	Y	N

[a] Numerical instabilities in wind speeds caused this job to crash after 90 years. It was completed by restarting the job in the 80^{th} year with the atmospheric timestep halved.

[b] This job is copy of job xdsid extended to $\approx$ 1000 yrs to enable confirmation of the return of CO_2 flux equilibrium (see Section 5.5).

bations, the first 5 years of some of these runs are repeated for 5 years, with mean monthly data output (hereafter denoted by an 'm' on the end of the job description). These different runs are summarised by job description—by which they will be referred to henceforth—in Table 5.2. From the results of Chapter 4 it is expected that increase in the value of v_s and/or P^s_{max} will increase the air-sea CO_2 flux into the ocean. In the first perturbed run (UM job xdsic), both v_s and P^s_{max} are perturbed up to establish whether the perturbations detailed in Table 5.1 are sufficiently large to result in a noticeable change in the air-sea CO_2 flux (see Section 5.5.1 below). For clarity, this job is referred to in the text as job v_s & P^s_{max} $\uparrow$ hereafter. With this confirmed, the subsequent runs perturb each parameter individually. The results for each job are detailed in Sections 5.5.1 and 5.6.

5.5 Interaction between the ecosystem and carbon in the ocean

Changing the behaviour (growth and decay) of the ocean ecosystem changes the amount of DIC that is fixed into or released from organic compounds. This changes the ocean's DIC concentration particularly near the surface where the ecosystem is most active. This change in DIC concentration alters the pCO_2^{sea} of the ocean surface, changing the size of the "$pCO_2^{sea} - pCO_2^{air}$" term in the gas exchange equation and hence the air-sea CO_2 flux (see Section 1.6). In the case of perturbations to the biology increasing the uptake of DIC and so reducing the ocean's DIC concentration, the net surface pCO_2^{sea} is reduced, triggering greater CO_2 uptake from the atmosphere until the ocean's DIC concentration becomes sufficient for the net surface pCO_2^{sea}

to regain equality with the fixed pCO_2^{air}. If the perturbations reduce the biological uptake of DIC, the ocean surface DIC concentration increases causing an increase in the surface pCO_2^{sea}. This results in outgassing to the atmosphere until the DIC concentration reduces sufficiently for the net ocean surface pCO_2^{sea} to once again equal the pCO_2^{air}. In both cases, the change in the behaviour of the biology causes a non-zero net air-sea CO_2 flux until the net surface ocean DIC concentration returns to its pre-perturbed state and the net air-sea CO_2 flux returns to zero. This can be seen in Figure 5.3 in which the FAMOUS job with v_s perturbed up is extended to a thousand years, during which the ocean carbon content gradually equilibrates with the fixed atmospheric CO_2 reducing the net CO_2 back towards zero.

In the 3D ocean mixing scheme used in FAMOUS (as in the real world), bodies of water in contact with the atmosphere are transported to the deep ocean and replaced with water from the deep (see Section 1.5.1). This slows the eventual return to equilibrium (zero net global air-sea CO_2 flux) as the whole ocean must re-equilibrate with the atmosphere. These processes are discussed further in Sections 5.5.1 and 5.7.

5.5.1 Air-sea CO_2 flux

Figure 5.2 shows the global annual mean air-sea CO_2 flux for the one hundred year jobs detailed in Table 5.2. These plots immediately show two things. Firstly, comparison of the results of the perturbed jobs with the unperturbed job F_0 (Figure 5.2) shows that the parameter perturbations have an effect on the calculated air-sea CO_2 flux. The unperturbed job F_0 shows a stable air-sea CO_2 flux compared to the other jobs (see also Table 5.3). Secondly, the change in the air-sea CO_2 flux arising from each perturbation is in the direction expected from the results of Chapter 4. Increasing the value of v_s and/or P^s_{max} increases the CO_2 flux into the ocean, while a decrease in CO_2 flux into the ocean is seen if the value of v_s or P^s_{max} decreases, or the value of Υ_c increases.

Table 5.3 compares the maximum, minimum, mean and standard deviations for the unperturbed and perturbed one hundred year jobs. Taking job v_s & P^s_{max} $\uparrow$, the maximum mean annual air-sea CO_2 flux of 0.60 mol CO_2 m^{-2} yr^{-1} is the equivalent of $\approx$ 2.61 Pg C y^{-1} uptake by the ocean, a large increase from the $\approx$ 0.0 Pg C uptake calculated from the maximum air-sea CO_2 flux of the unperturbed job F_0 [3] 2.61 Pg C is comparable with current estimates of the annual oceanic carbon uptake (IPCC fourth assessment 2.2 $\pm$ 0.5 Pg C y^{-1} Denman et al. [2007], 2.2 $\pm$ 0.3 Pg C y^{-1} Gruber et al. [2009]), indicating that the results of these perturbations are plausible within the quantities of carbon contained in the climate system.

Looking again at Figure 5.2, the direction of the change in air-sea CO_2 flux separates the results into two sets. Where the parameter perturbations cause an increase in CO_2 flux into the ocean

[3] This calculation assumes an ocean surface area of 362 million km^2 = 3.62×10^{14} m^2, and the molar mass of C = 12.01 g. 1 Pg = 1.0×10^{15} g.

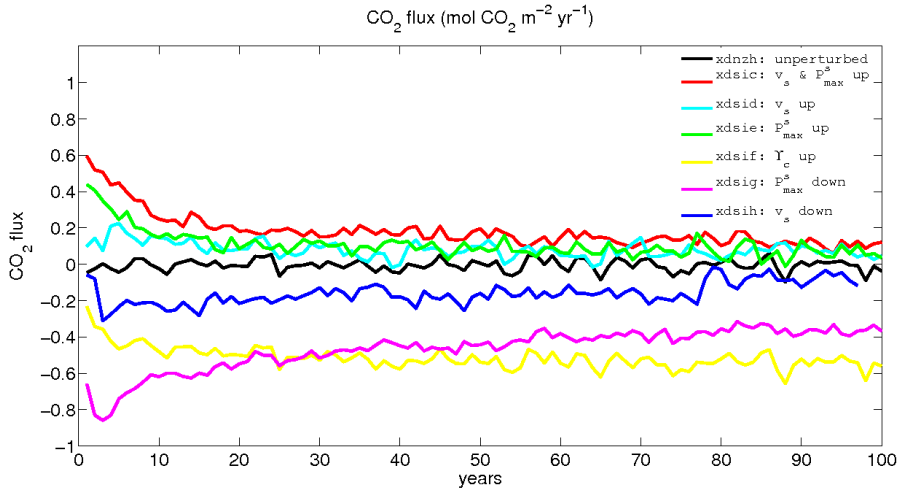

Figure 5.2: Annual mean air-sea CO_2 flux (mol CO_2 m^{-2} yr^{-1}) calculated in FAMOUS for the unperturbed job F_0, v_s and P^s_{max} perturbed up (job v_s & P^s_{max} $\uparrow$), v_s perturbed up (job v_s $\uparrow$), P^s_{max} perturbed up (job P^s_{max} $\uparrow$), P^s_{max} perturbed down (job P^s_{max} $\downarrow$), and v_s perturbed down (job v_s $\downarrow$). CO_2 flux into the ocean is positive. As noted in Table 5.3, job v_s $\downarrow$ crashed due to numerical instabilities in the wind speeds after around 90 years. To successfully complete the job the atmospheric timestep was halved and the job restarted from the 80 year dump file. However, looking at the results of job v_s $\downarrow$, it is clear that due to the effect of wind speeds on the air-sea CO_2 flux this alteration of the timestep has reduced the effect of the parameter perturbation for the last twenty years of the run. For this reason, the results of these twenty years are not used in this work.

Table 5.3: Summary of mean annual air-sea CO_2 flux results (mol CO_2 m^{-2} yr^{-1}), for FAMOUS 100 year jobs as detailed in Table 5.2. Those for job v_s $\downarrow$ are for the final decade before the change in atmospheric timestep (see Section 5.5.1).

Job	Max	Min	Mean	σ
F_0	0.062	-0.098	-0.0064	0.032
v_s & P^s_{max} $\uparrow$	0.60	0.058	0.18	0.093
v_s $\uparrow$	0.22	-0.019	0.080	0.044
P^s_{max} $\uparrow$	0.44	-0.013	0.11	0.074
Υ_c $\uparrow$	-0.23	-0.66	-0.52	0.059
P^s_{max} $\downarrow$	-0.86	-0.32	-0.47	0.11
v_s $\downarrow$	-0.016	-0.31	-0.18	0.051

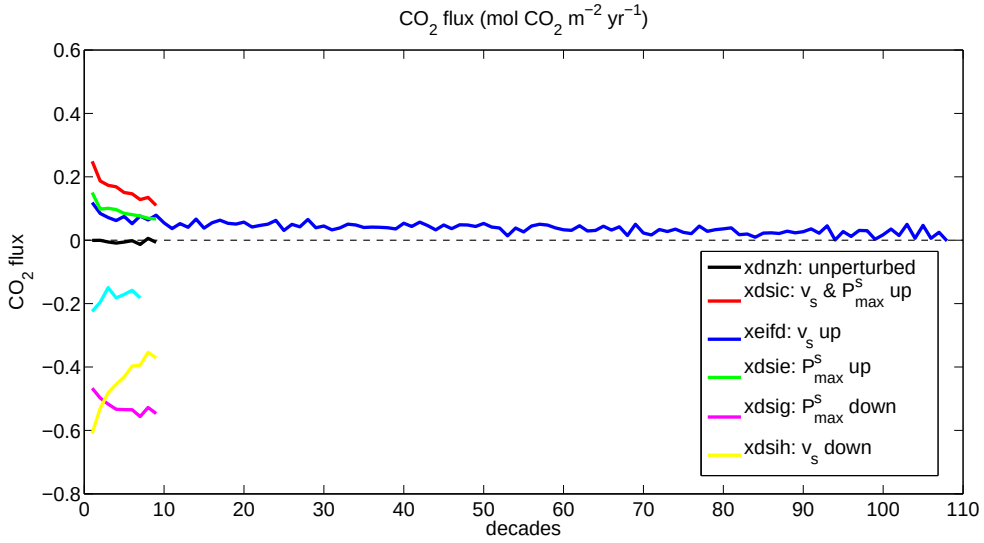

Figure 5.3: Decadal mean global air-sea CO_2 flux (mol CO_2 m^{-2} yr^{-1}) calculated in FAMOUS. This shows the FAMOUS job xeifd which is job $v_s \uparrow$ extended to $\approx$ 1000 years to allow the perturbed ocean carbon system to equilibrate with the fixed atmospheric pCO_2^{air} returning the net global air-sea CO_2 flux to near-zero (see Section 5.5). The mean decadal data for the 100 year FAMOUS jobs (see Table 5.2 and Figure 5.2) are also plotted.

(jobs v_s & $P^s_{max} \uparrow$, $v_s \uparrow$, and $P^s_{max} \uparrow$), the CO_2 flux changes rapidly, then decreases within the first 20 years to slightly higher than the CO_2 flux of the unperturbed job F_0 (cf. the maximum and minimum values for job F_0 with those for jobs v_s & $P^s_{max} \uparrow$, $v_s \uparrow$, and $P^s_{max} \uparrow$ in Table 5.3). The CO_2 flux then gradually reduces as the uptake of CO_2 into the ocean replaces the DIC taken up by the ecosystem reducing the difference between the pCO_2^{sea} and the fixed pCO_2^{air} (see Section 5.5). This is seen more clearly in Figure 5.3 which shows the decadal mean CO_2 flux for job $v_s \uparrow$ extended to just over one thousand years.

Where the parameter perturbations cause a decrease in CO_2 flux into the ocean (jobs $\Upsilon_c \uparrow$, $P^s_{max} \downarrow$, and $v_s \downarrow$), there is a rapid initial reaction (outgassing) to the increase in DIC concentration caused by the perturbation. In jobs $P^s_{max} \downarrow$ and $v_s \downarrow$ the outgassing quickly reduces as the loss of DIC to the atmosphere redresses the balance between the pCO_2^{sea} and the fixed pCO_2^{air} (see Section 5.5). Job $\Upsilon_c \uparrow$ behaves differently, with the outgassing taking longer (around 20 years) to reach its maximum and not reducing within the century of the job, although it will eventually return to zero. This will be returned to in Section 5.5.1.2.

The explanation for the behaviour of the CO_2 flux for all the perturbations arises from the decoupled carbon cycle used in FAMOUS (see Sections 5.3 and 5.5). The ocean 'sees' a constant pCO_2^{air} of 290ppm which is not influenced by changes in the air-sea CO_2 flux. Perturbing the values of HadOCC parameters alters the pCO_2^{sea}, changing the difference between the partial pressures in the gas exchange equation (see Sections 5.5, 1.6 and 5.7.1), and hence the air-sea

CO_2 flux. Initially, the parameter perturbation changes the surface pCO_2^{sea} from the stable value of the starting dump, causing a rapid (on a timescale of less than a year to five years) change in the air-sea CO_2 flux away from the stable equilibirium present in the unperturbed job F_0. These initial effects are explored in detail in Section 5.5.1.1 below. As the ingassing or outgassing returns the DIC concentration of the upper mixed ocean towards its unperturbed value the net CO_2 flux decreases, eventually returning to zero on the timescale of ocean turnover (10^3 years). Section 5.5.1.2 explores the air-sea CO_2 flux for the last decade of the jobs to look at the effect of the perturbations after a century (medium-term).

As noted in Table 5.2, job $v_s \downarrow$ crashed due to numerical instabilities in the wind speeds after around 90 years. To successfully complete the job the atmospheric timestep was halved and the job restarted from the 80 year dump file. However, looking at Figure 5.2, it is clear that this alteration of the timestep has reduced the effect of the parameter perturbation for the last twenty years of the run. For this reason, the results of these twenty years are discarded and the results for the 7th decade (the last decade before the crash) are used in Section 5.5.1.2.

5.5.1.1 Initial effects

Here, the initial effects of the parameter perturbations are explored in greater detail. Taking the different perturbations in turn, the perturbations in job v_s & $P^s_{max} \uparrow$ and job $P^s_{max} \uparrow$ immediately increase the CO_2 flux into the ocean (see Figure 5.2). Job $v_s \uparrow$, by comparison, has less of an effect, with a much smaller increase ($\approx +0.14$ mol C m^{-2} yr^{-1}) in the CO_2 flux into the ocean in the first year with a slight increase in the next few years. This indicates that the perturbation of the maximium photosythetic rate P^s_{max} has a greater and quicker initial effect (acting on a timescale shorter than a year), on the air-sea CO_2 flux, than the perturbation of the detrital sink rate v_s, which acts more slowly.

To look at the initial effects of the perturbations of v_s and P^s_{max} more closely, the FAMOUS runs $v_s \uparrow$ and $P^s_{max} \uparrow$ are repeated in jobs $v_s \uparrow$m and $P^s_{max} \uparrow$m for the first 5 years with monthly air-sea CO_2 flux output. The unperturbed job F_0 is similarly repeated as job F_0m (see Table 5.2). These monthly results are shown in Figures 5.4 (job F_0), 5.5, and 5.6 ($P^s_{max} \uparrow$). The unperturbed job F_0m (Figure 5.4) exhibits a stable annual cycle as should be expected. Job $v_s \uparrow$m (Figure 5.5) is initially very similar to the unperturbed job F_0m but after the first year the air-sea CO_2 flux annual cycle gradually increases as shown in the mean annual plot in Figure 5.2. The effect of the increase in value of P^s_{max} in job $P^s_{max} \uparrow$m (Figure 5.6) is very rapid (and much larger than that of increasing v_s), with the air-sea CO_2 flux responding to the change in the surface pCO_2^{sea} within the first month. After peaking in the first year, the annual cycle for the air-sea CO_2 flux for job $P^s_{max} \uparrow$m then slowly decreases as seen in Figure 5.2. All exhibit an annual cycle, but that for job $P^s_{max} \uparrow$m has a greater amplitude for the second part of the year than in the other jobs due to the abundant nutrient supply in the Southern Ocean. This is explored further in Sections 5.6 and 5.6.1.

Table 5.4: Mean CO_2 flux (mol CO_2 m^{-2} yr^{-1}), for the first decade of 100 year jobs detailed in Table 5.2. Mean annual carbon uptake from the ocean in Pg is also stated: ocean surface area taken to be total sea-surface area in FAMOUS = $3.62429 \times 10^{14} m^2 \approx 362$ million km^2, molar weight of carbon 12.01g. Difference in the mean carbon uptake between the unperturbed job F_0 and the perturbed job in final column. Carbon flux into the ocean is positive.

Job	Mean CO_2 flux (mol CO_2 m^{-2} yr^{-1}), for first decade	Ocean C uptake (Pg C)	Difference in C uptake from job F_0 (Pg C).
F_0	-0.000483	-0.00210	-
v_s & P^s_{max} ↑	0.249	1.08	1.085
v_s ↑	0.119	0.517	0.519
P^s_{max} ↑	0.150	0.655	0.657
Υ_c ↑	-0.467	-2.03	-2.03
P^s_{max} ↓	-0.609	-2.65	-2.65
v_s ↓	-0.225	-0.978	-0.976

Jobs Υ_c ↑, P^s_{max} ↓, and v_s ↓ all result in decreased air-sea CO_2 flux into the ocean compared to the unperturbed job F_0 (see Figure 5.2). Increasing the value of the rain ratio Υ_c in job Υ_c ↑ reduces the air-sea CO_2 flux in the first year, and reduces it further in subsequent years, with the rate of the decrease slowing. In job P^s_{max} ↓, the decrease in the value of P^s_{max} causes a large reduction in the mean annual air-sea CO_2 flux into the ocean in the first year, with further reduction for the next three years before sufficient CO_2 uptake has occured to start to slow the rate of outgassing which will eventually return to zero. Finally, decreasing the value of the detrital sink rate v_s slightly reduces the CO_2 flux into the ocean in the first year, with further decrease for the next two years, before increasing slowly to trend gradually towards zero net air-sea CO_2 flux.

Looking at the initial effect of perturbing each of the three parameters, it is clear that the air-sea CO_2 flux reacts much more quickly to change in the value of P^s_{max} than changes in the values of v_s and Υ_c. The value of P^s_{max} sets the maximum photosynthetic growth rate of phytoplankton under conditions of light saturation. Near the ocean surface, solar radiation is abundant, so phytoplankton growth is not light limited. Phytoplankton growth is very rapid (on the order of hours to days—FAMOUS has an ocean timestep of 12 hours), so changing the maximum photosynthetic rate of the phytoplankton very quickly changes the biological uptake of dissolved CO_2 near the surface, altering the surface pCO_2^{sea} and hence changing the air-sea CO_2 flux.

The detrital sink rate v_s influences the surface pCO_2^{sea}, and hence the air-sea CO_2 flux by governing the export of organic carbon away from the upper ocean. The more rapidly organic carbon sinks through the water column, the greater the amount that leaves the upper ocean, as less is broken down to dissolved inorganic carbon (DIC). To reduce the DIC concentration—and hence the pCO_2^{sea}—of the upper ocean, this sinking material must be transported away from the upper

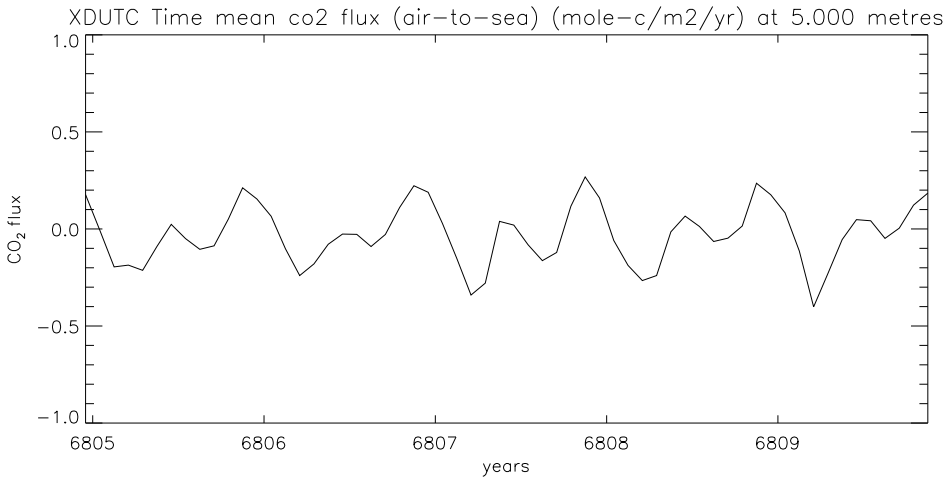

Figure 5.4: Job F_0m (unperturbed), monthly mean air-sea CO_2 flux (mol CO_2 m^{-2} yr^{-1}). CO_2 flux into the ocean is positive.

ocean to below the maximum depth of the mixed layer, a slower process than photosynthetic growth. For this reason, the effect of changes in the value of v_s is less rapid than that seen for changes in the value of P^s_{max}. The effect of increasing the value of P^s_{max} is explored further in Section 5.6.1.

In job v_s & P^s_{max} $\uparrow$, where both v_s and P^s_{max} are perturbed up, the initial change in the air-sea CO_2 flux is greater than that for jobs v_s $\uparrow$ or P^s_{max} $\uparrow$ (v_s and P^s_{max} perturbed up individually). Looking more closely at the numbers, the change in air-sea CO_2 flux of $\approx +0.64$ mol CO_2 m^{-2} yr^{-1} in the first year of job v_s & P^s_{max} $\uparrow$ is just more than the sum of the changes seen in the first year of the individually perturbed jobs—only v_s perturbed up, a change of $\approx +0.14$ mol C m^{-2} yr^{-1}, only P^s_{max} perturbed up, a change of $\approx +0.48$ mol C m^{-2} yr^{-1}. This shows that the effects of increasing these parameters work in concert, as might be expected from the results of Chapter 4.

Figures 5.7 to 5.13 (top plots) are global plots of the mean air-sea CO_2 flux in mol CO_2 m^{-2}, for the first year and first decade of the 100 year jobs detailed in Table 5.2. Ocean uptake (CO_2 flux into the ocean) is taken to be positive, with negative values showing outgassing from the ocean to the atmosphere. Figures 5.8 to 5.13 (bottom plots) show the difference between the perturbed 100 year jobs shown in the top plots, and the unperturbed job F_0. This is calculated as the CO_2 flux of each ocean grid cell for the perturbed job minus the CO_2 flux for the corresponding grid cell of the unperturbed job.

Firstly, the unperturbed job F_0 (Figure 5.7) shows a similar spatial distribution of the annual air-sea CO_2 flux to the Takahashi et al. [2002] climatology shown in Figure 1.5—notably the large region of outgassing in the tropical Pacific. Nowhere is the ingassing for job F_0 as strong as

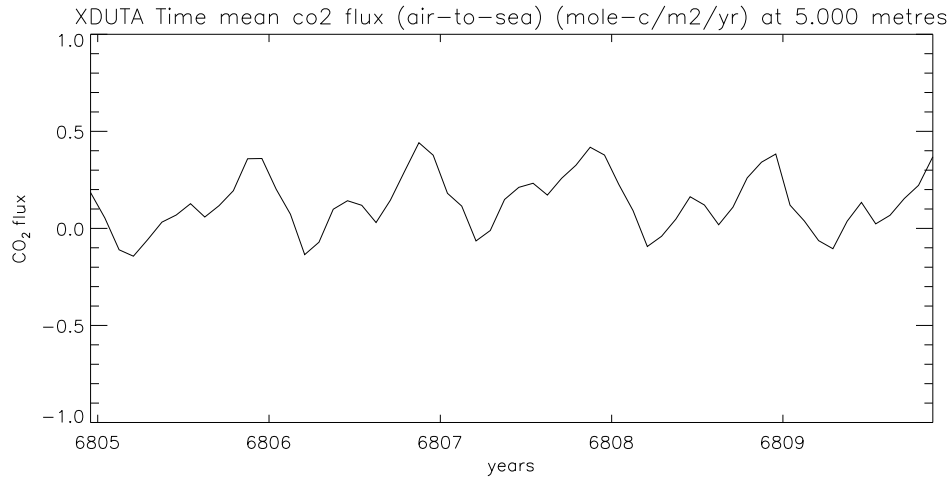

Figure 5.5: Job v_s ↑m, monthly mean air-sea CO_2 flux (mol CO_2 m^{-2} yr^{-1}). CO_2 flux into the ocean is positive.

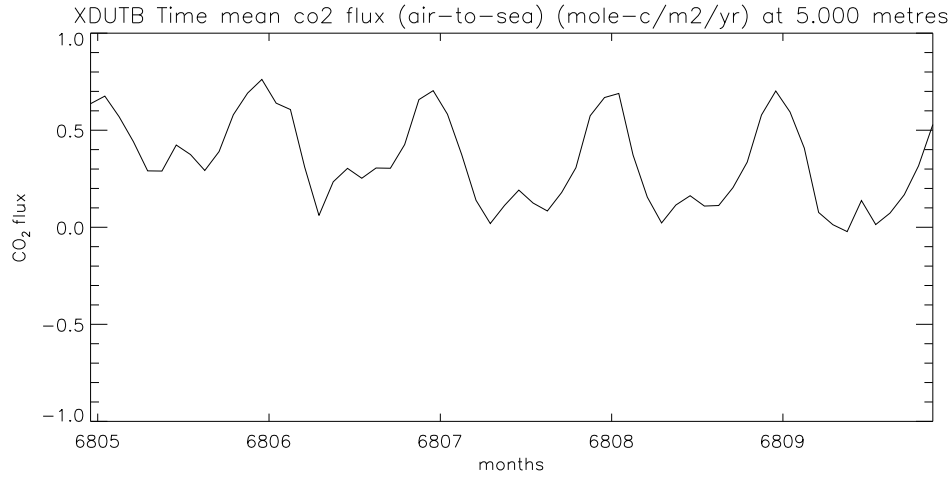

Figure 5.6: Job P^s_{max} ↑m, monthly mean air-sea CO_2 flux (mol CO_2 m^{-2} yr^{-1}). CO_2 flux into the ocean is positive.

that shown in the north-east Atlantic in Takahashi et al. [2002], but it must be remembered that job F_0 represents the conditions of 1860, not the anthropogenically forced situation of 1995.

The global plots of the first year of the perturbations (Figures 5.8 to 5.13—top left plots) do not differ greatly from the plots of the first decade (Figures 5.8 to 5.13—top right plots). In general, the perturbed jobs exhibit the same broad pattern of outgassing (in the tropics and gyres) and ingassing (high latitude) regions. The perturbations influence the size of the fluxes from these regions, but not their more general location. This is to be expected, as the perturbations affect only the ocean biology, and do not alter the physical mixing of the ocean.

Looking in more detail at the results of the perturbed jobs, as should be expected from the global mean plot for job v_s & $P^s_{max} \uparrow$ (Figure 5.2), the size of the outgassing flux in outgassing regions has been reduced, while in ingassing regions the size of the ingassing flux has been increased. The difference plots—Figure 5.8 bottom plots—show that the greatest effect of the parameter perturbations is to reduce the outgassing of the South American Pacific coastal waters by around 5 to 10 mol CO_2 m^{-2}. The individual upwards perturbation of v_s in job $v_s \uparrow$ shows only small changes to the air-sea CO_2 flux of, at very most, 5 mol CO_2 m^{-2} yr^{-1}—see Figure 5.9 bottom plots—as expected from the global annual mean plot in Figure 5.2. Figure 5.10 shows that the increase in the value of P^s_{max} in job $P^s_{max} \uparrow$ reduces the flux of outgassing regions more strongly than is seen in job $v_s \uparrow$, and also increases the flux of ingassing regions more than in job $v_s \uparrow$—c.f. the Antarctic waters in Figure 5.10 with those in Figure 5.9. Interestingly, the difference plots for jobs v_s & $P^s_{max} \uparrow$, $v_s \uparrow$, and $P^s_{max} \uparrow$ (bottom plots in Figures 5.8, 5.9 and 5.10) show that while the major effect of the increase in the value of v_s and/or P^s_{max} is to reduce the strength of the outgassing regions, some regions—most clearly in the subtropical Pacific—show a decrease in the CO_2 flux into the ocean. The explanation for this is that primary production (and resulting dissolved CO_2 uptake) in these regions is reduced as nutrient supplies are diminished by the faster sinking of detritus (in job $v_s \uparrow$), or in the case of job $P^s_{max} \uparrow$, used up by the phytoplankton in upwelling areas due to the increased growth allowed by the increase in photosynthentic rate (See Section 5.6 and Figures 5.25 to 5.28).

Moving on to job $\Upsilon_c \uparrow$, the perturbation reinforces outgassing regions and reduces the ingassing as expected. Looking at the difference plots—Figure 5.11 bottom plots—the increase in Υ_c reduces the CO_2 flux into the ocean across the whole ocean by around 1-2 mol CO_2 m^{-2}. This contrasts to the perturbations that result in increased air-sea CO_2 flux discussed above, where distinct regions are influenced much more strongly (c.f. the difference plots in Figure 5.11 with those in Figures 5.8, 5.9 and 5.10). This is due to the fact that the change in the value of the rain ratio (Υ_c) causes less DIC to be uptaken by phytoplankton growth, but does not change the use or supply of nutrient by the phytoplankton, so the distribution of phytoplankton remains the same as in the unperturbed job F_0. This is dsicussed further in Section 5.6.

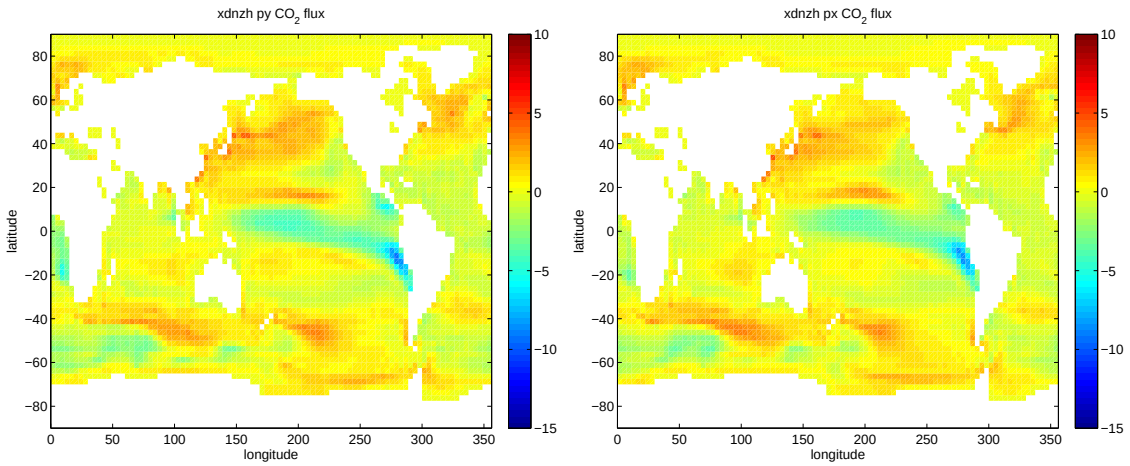

Figure 5.7: Job F_0 (unperturbed), air-sea CO_2 flux (mol CO_2 m^{-2} yr^{-1}) for the first year (left) and first decade (right) of the job. CO_2 flux into the ocean is positive.

Lastly, the plots for jobs P^s_{max} $\downarrow$ (Figure 5.12) and v_s $\downarrow$ (Figure 5.13) show that both these perturbations increase the outgassing flux from outgassing regions and reduce uptake in ingassing regions. As expected from the annual mean plots (Figure 5.2), the decrease in the value of P^s_{max} has a greater effect than the decrease in the value of v_s. A very slight increase in the CO_2 uptake in the ocean gyres can be seen in the difference plots in Figures 5.12 and 5.13, possibly due to an increase in the amount of nutrient available in the gyres due to the reduced phytoplankton growth in more productive regions (for job P^s_{max} $\downarrow$), or the reduced sinking of detritus—enabling more to be broken down to nutrient—in the case of job v_s $\downarrow$.

Comparing the difference plots for the three jobs that result in reduced CO_2 flux into the ocean (bottom plots in Figures 5.11, 5.12 and 5.13), it can be seen that for the decrease in the values of P^s_{max} and v_s there is a much clearer spatial pattern to the change in the CO_2 flux. In these jobs (P^s_{max} $\downarrow$ and v_s $\downarrow$), the flux in the high latitudes and tropics changes by around 1-5 mol CO_2 m^{-2} while there is much lesser change in the mid-latitude gyres, whereas, as noted above, the increase in value of Υ_c has a much more homogeneous effect.

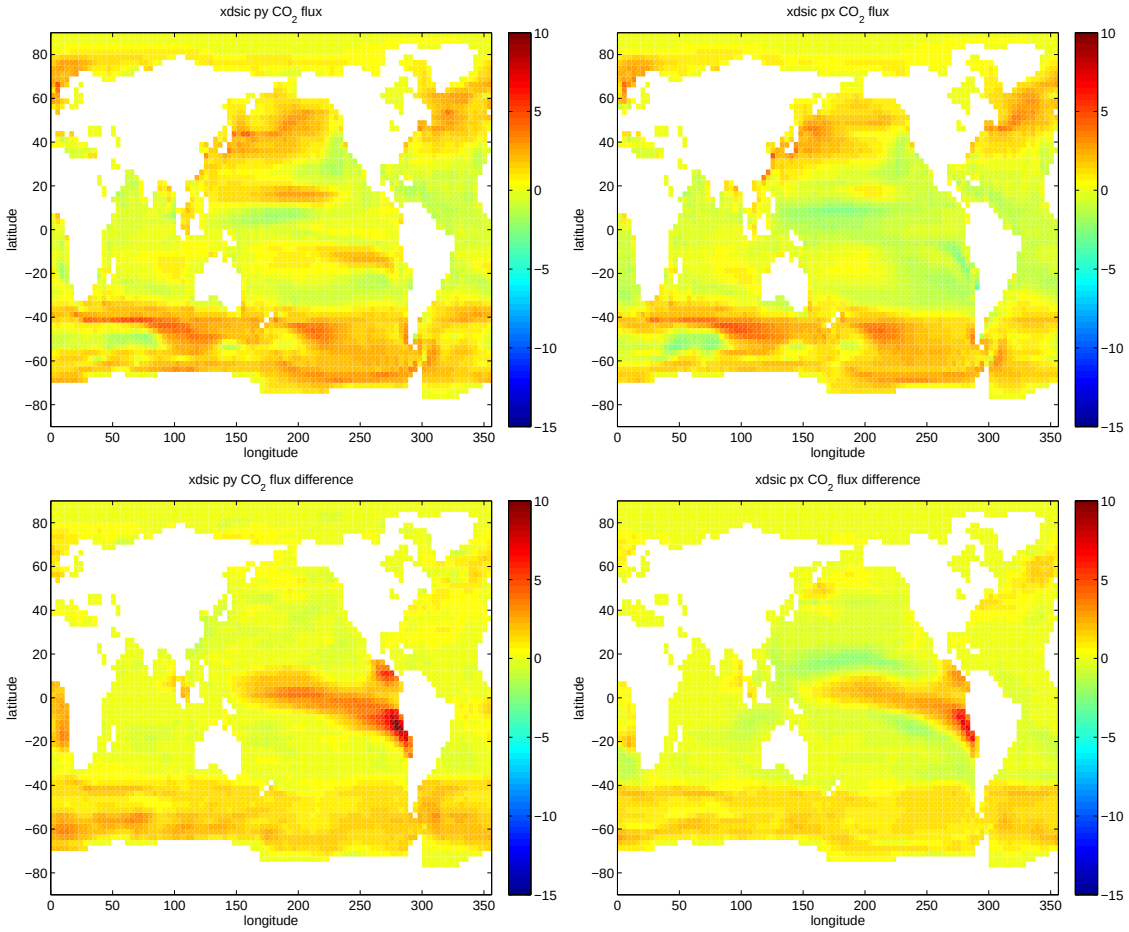

Figure 5.8: Top plots: job v_s & P^s_{max} ↑ air-sea CO_2 flux (mol CO_2 m^{-2} yr^{-1}) for the first year (left) and first decade (right) of the job. CO_2 flux into the ocean is positive. Bottom plots: Difference in air-sea CO_2 flux (mol CO_2 m^{-2} yr^{-1}), between job v_s & P^s_{max} ↑ and job F_0 for the first year (left) and first decade (right) of the jobs.

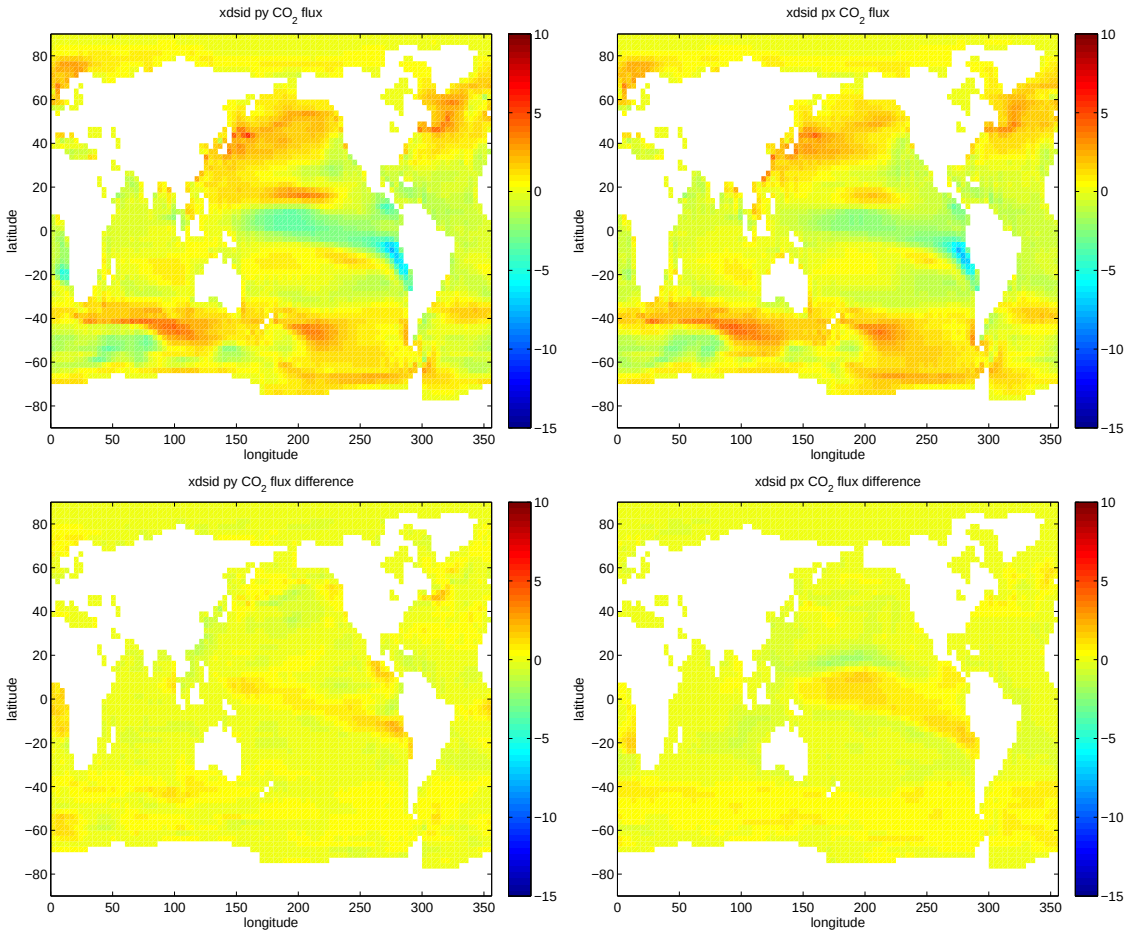

Figure 5.9: Top plots: job $v_s \uparrow$ air-sea CO_2 flux (mol CO_2 m^{-2} yr^{-1}) for the first year (left) and first decade (right) of the job. CO_2 flux into the ocean is positive. Bottom plots: difference in air-sea CO_2 flux (mol CO_2 m^{-2} yr^{-1}) between job $v_s \uparrow$ and job F_0 for the first year (left) and first decade (right) of the jobs.

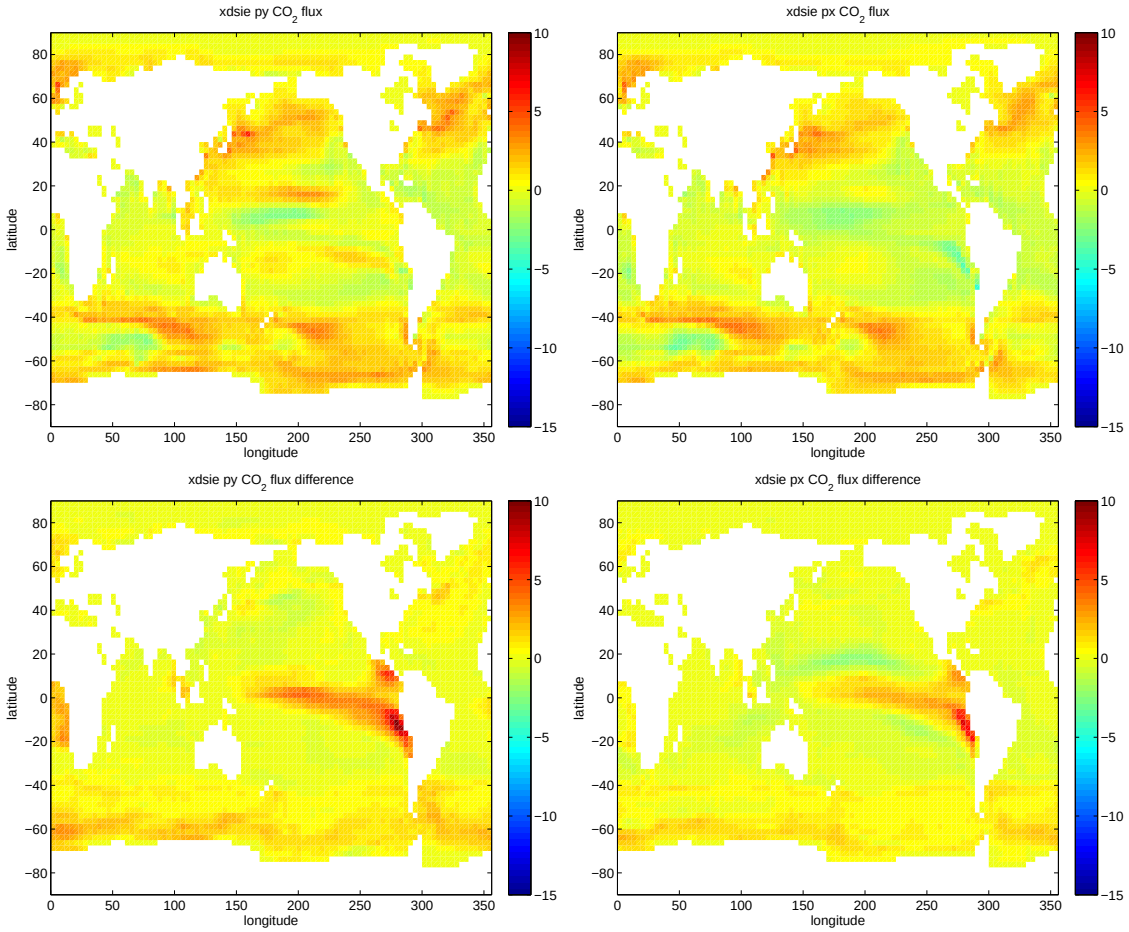

Figure 5.10: Top plots: job $P^s_{max}\uparrow$ air-sea CO_2 flux (mol CO_2 m^{-2} yr^{-1}) for the first year (left) and first decade (right) of the job. CO_2 flux into the ocean is positive. Bottom plots: difference in air-sea CO_2 flux (mol CO_2 m^{-2} yr^{-1}) between job $P^s_{max}\uparrow$ and job F_0 for the first year (left) and first decade (right) of the jobs.

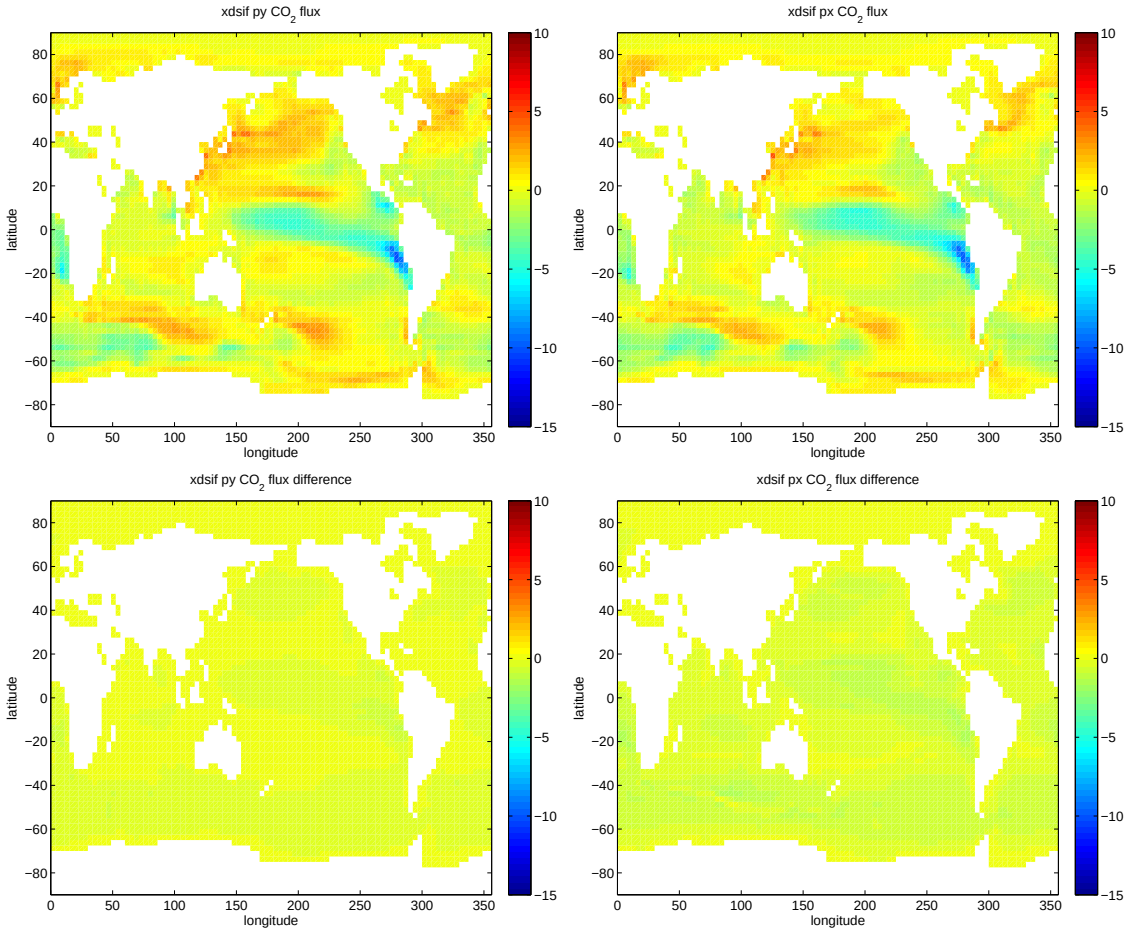

Figure 5.11: Top plots: job $\Upsilon_c \uparrow$ air-sea CO_2 flux (mol CO_2 m^{-2} yr^{-1}) for the first year (left) and first decade (right) of the job. CO_2 flux into the ocean is positive. Bottom plots: difference in air-sea CO_2 flux (mol CO_2 m^{-2} yr^{-1}) between job $\Upsilon_c \uparrow$ and job F_0 for the first year (left) and first decade (right) of the jobs.

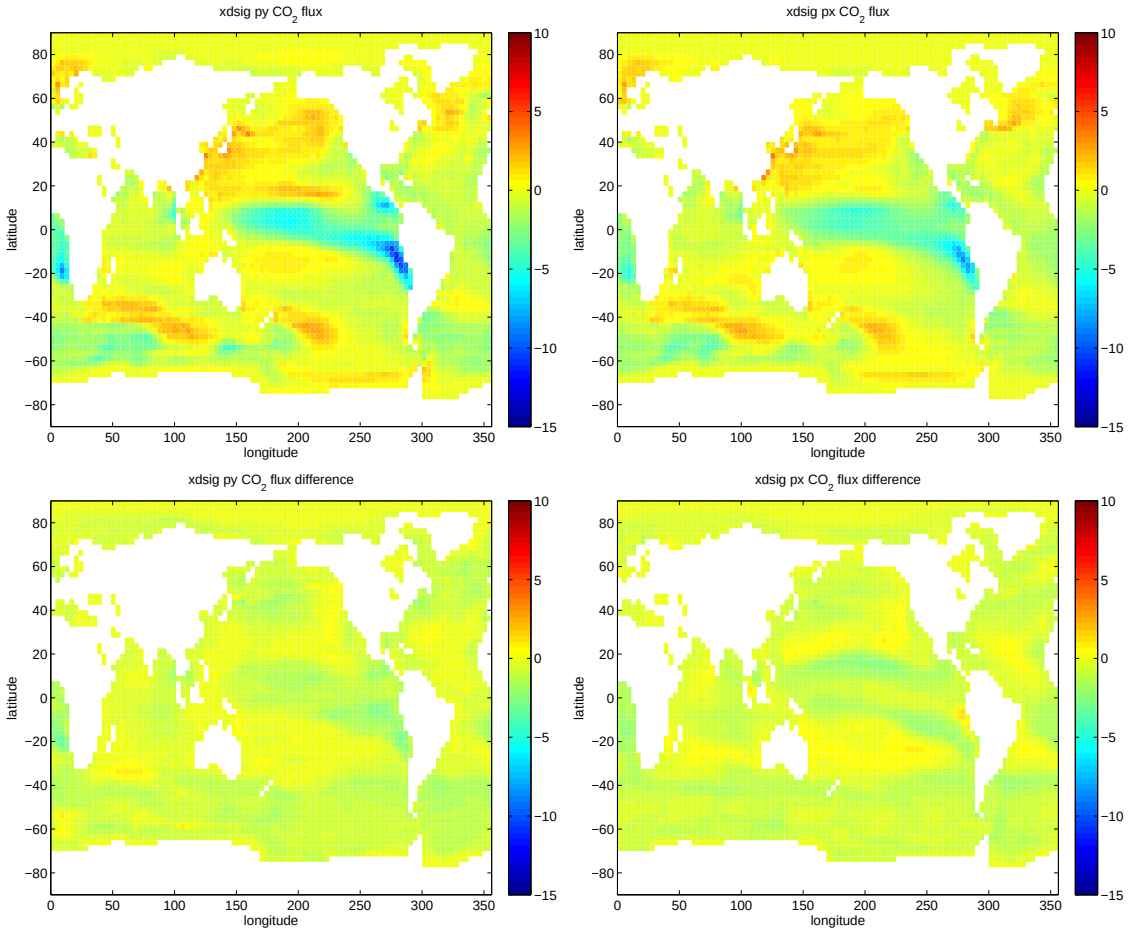

Figure 5.12: Top plots: job $P^s_{max}\downarrow$ air-sea CO_2 flux (mol CO_2 m^{-2} yr^{-1}) for the first year (left) and first decade (right) of the job. CO_2 flux into the ocean is positive. Bottom plots: difference in air-sea CO_2 flux (mol CO_2 m^{-2} yr^{-1}) between job $P^s_{max}\downarrow$ and job F_0 for the first year (left) and first decade (right) of the jobs.

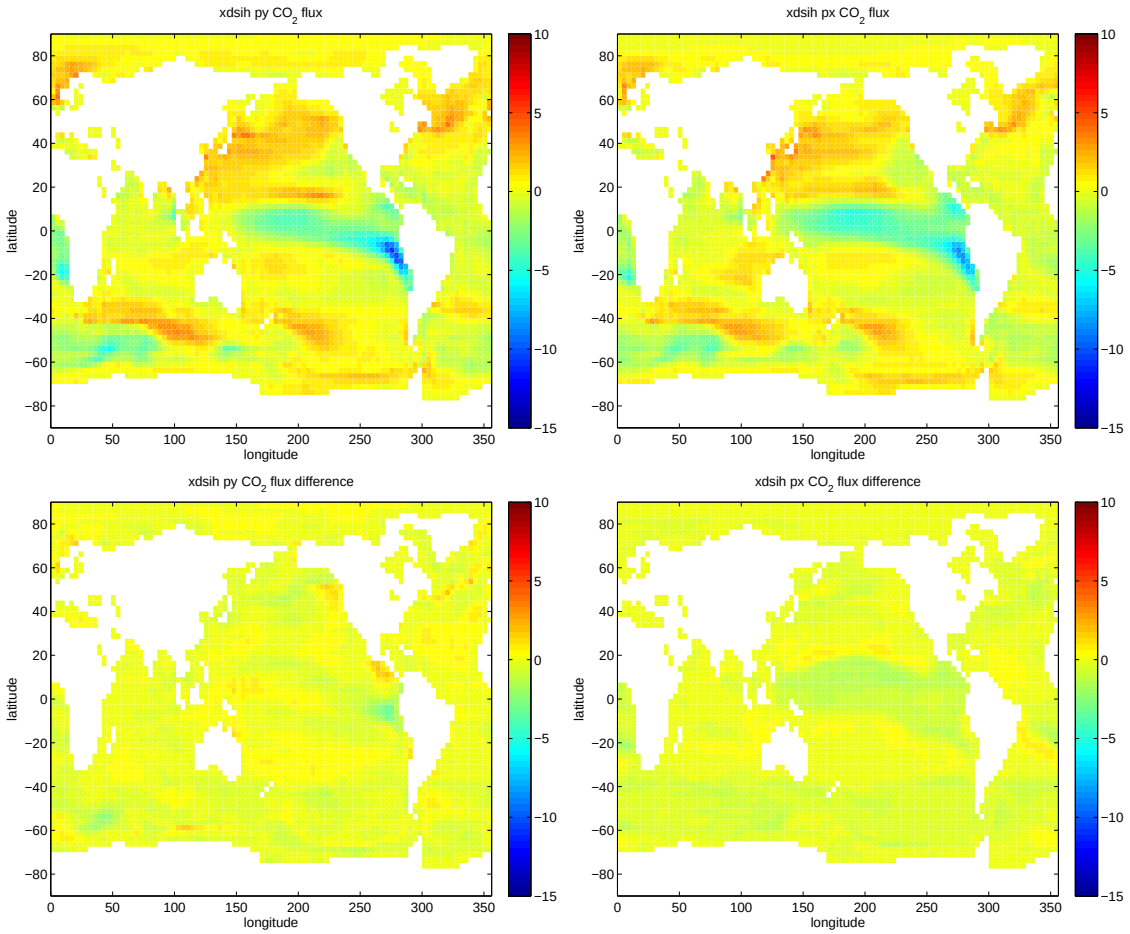

Figure 5.13: Top plots: job $v_s \downarrow$ air-sea CO_2 flux (mol CO_2 m^{-2} yr^{-1}) for the first year (left) and first decade (right) of the job. CO_2 flux into the ocean is positive. Bottom plots: difference in air-sea CO_2 flux (mol CO_2 m^{-2} yr^{-1}) between job $v_s \downarrow$ and job F_0 for the first year (left) and first decade (right) of the jobs.

5.5.1.2 Medium term effects

The annual mean air-sea CO_2 flux plots shown in Figure 5.2 show the CO_2 flux slowly trending towards a zero net flux level as the pCO_2^{sea} equilibrates with the constant atmospheric pCO_2^{air}. Here, the effects of the biogeochemical parameter perturbations at the end of the jobs (after around a century) are explored. The final decade of the perturbed jobs is compared to the final decade of the unperturbed job (for job $v_s \downarrow$ this is taken to be the last decade before the change in atmospheric timestep—see Section 5.5.1). Table 5.5 compares the mean annual air-sea CO_2 fluxes of the final decade, for the 100 year jobs detailed in Table 5.2. Comparing these with the results for the first decade in Table 5.4 (and Figure 5.2), the flux for the unperturbed job F_0 has hardly changed, while for the perturbed jobs, the air-sea CO_2 flux for the final decade is closer to the unperturbed flux than the first decade, with the exception of job $\Upsilon_c \uparrow$.

Table 5.5 also shows the change in annual carbon uptake (in Pg C) that results from the changes in air-sea CO_2 flux caused by the parameter perturbations. The perturbations that reduce the air-sea CO_2 flux into the ocean result in large losses of carbon to the atmosphere—most notably in the case of the increased rain ratio (Υ_c) scenario (job $\Upsilon_c \uparrow$)—where the amount of outgassing is comparable to the higher estimates of the current ocean carbon sink (e.g. 2.2 ± 0.5 Pg C [Denman et al., 2007]). However, the validity of these results is limited by the fact that due to the set up of FAMOUS, the outgassing does not change the atmospheric CO_2 concentration or the corresponding pCO_2^{air} 'seen' by the ocean surface (see Section 5.3 and 5.5).

The behaviour of job $\Upsilon_c \uparrow$ in Figure 5.2 contrasts with that of jobs $P^s_{max} \downarrow$ and $v_s \downarrow$ in that no reduction from the initial level of outgassing following the perturbation is seen within the one hundred years of the job (see also Tables 5.4 and 5.5). The value of Υ_c controls the proportion of organic growth that is converted to carbonate, a process that releases organic carbon to DIC, increasing the pCO_2^{sea} (see Sections 3.2.8). However, unlike decreasing the value of P^s_{max} or v_s, increasing the value of Υ_c does not directly alter the use or supply of nutrient to phytoplankton. As a result, the effect of the increased rain ratio on the DIC concentration is not mitigated by changing production, so the return of the DIC concentration to its equilibrium state takes place more slowly. This is explored again in Section 5.6.

In the case of the perturbations that result in increased CO_2 uptake by the oceans (jobs v_s & $P^s_{max} \uparrow$, $v_s \uparrow$, and $P^s_{max} \uparrow$), due to the constant pCO_2^{air} (in this case the uptake by the ocean does not decrease the atmospheric CO_2 concentration), the results in Table 5.5 are perhaps comparable to a situation in which the atmospheric CO_2 concentration is forced by the addition of an amount of carbon (e.g. by anthropogenic activity) that matches the ocean uptake and so maintains a constant atmospheric concentration. Looking at these results, the change in ocean uptake after a century is of the order of the current error in the size of the ocean carbon sink (± 0.5 Pg C [Denman et al., 2007]), with that for job v_s & $P^s_{max} \uparrow$, where both parameters are perturbed, matching the value of this error. This suggests that reasonable perturbations to the key ocean

Table 5.5: Mean CO_2 flux (mol CO_2 m^{-2} yr^{-1}), for the final decade of the one hundred year jobs detailed in Table 5.2. In all but the case of job $\Upsilon_c \uparrow$ the level of outgassing or ingassing has decreased from that seen in Table 5.4 as the ocean's DIC concentration equilibrates with fixed atmospheric CO_2. As before, the final decade of job $v_s \downarrow$ is taken to be the 7^{th} (see Section 5.5.1 and Figure 5.2). The resulting mean annual carbon uptake of the ocean in Pg is also stated: ocean surface area taken to be total sea-surface area in FAMOUS = 3.62429×10^{14} $m^2 \approx 362$ million km^2, molar weight of carbon 12.01g. Difference in mean carbon uptake between unperturbed job F_0 and perturbed job in far right column. Carbon flux into the ocean is positive.

Job	Mean CO_2 flux (mol CO_2 m^{-2} yr^{-1}), for final decade	Mean annual ocean C uptake (Pg yr^{-1})	Difference in C uptake from job F_0 (Pg yr^{-1})
F_0	-0.00678	-0.0294	-
v_s & $P^s_{max} \uparrow$	0.110	0.476	0.505
$v_s \uparrow$	0.0788	0.342	0.371
$P^s_{max} \uparrow$	0.0673	0.292	0.321
$\Upsilon_c \uparrow$	-0.547	-2.37	-2.34
$P^s_{max} \downarrow$	-0.372	-1.61	-1.58
$v_s \downarrow$	-0.182	-0.792	-0.763

biology parameters (from 10 to 15.38 m d^{-1} for v_s and from 0.6 to 1.12 d^{-1} for P^s_{max}) can have a noticable effect on the carbon uptake of the ocean as calculated by GCMs that is comparable to current uncertainties of the system.

Figure 5.14 shows the mean air-sea CO_2 flux for the unperturbed job F_0. Figures 5.15 to 5.20 show the corresponding fluxes for the perturbed 100 year jobs (top plot), and the difference between these perturbed jobs and job F_0 (bottom plot). The patterns of the difference plots are in general very similar (the first decade and last decade of the jobs have a pattern correlation[4] of 0.8) to those explored for the initial effects in Section 5.5.1.1 (see Figures 5.7 to 5.13), though as expected from the net global flux results in Figure 5.2, of slightly reduced strength in all but the case of Figure 5.18 for job $\Upsilon_c \uparrow$.

As noted before, in Section 5.5.1.1, the perturbations that result in increased air-sea CO_2 flux into the ocean (jobs v_s & $P^s_{max} \uparrow$, $v_s \uparrow$, and $P^s_{max} \uparrow$), reduce the flux from outgassing regions and increase that of ingassing regions. While the global net effect is an increased uptake of carbon by the ocean, the gyres (especially in the Pacific) show a decrease (in some places changing direction to become outgassing) in uptake in Figures 5.15, 5.16 and 5.17, with the explanation due to be reduced nutrient supply to these regions as discussed in Section 5.5.1.1 above, and in Section 5.6 below.

[4]This is the Pearson correlation between the first decade and last decade CO_2 flux data for each job—see Section 2.4.2.

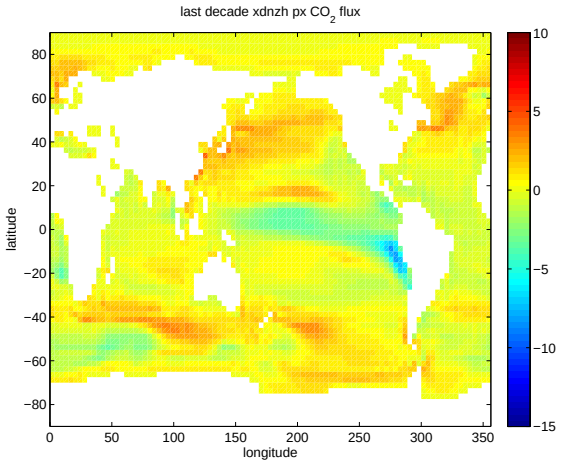

Figure 5.14: Job F_0 (unperturbed), decadal air-sea CO_2 flux (mol CO_2 m^{-2} yr^{-1}), for the last decade of the job. CO_2 flux into the ocean is positive.

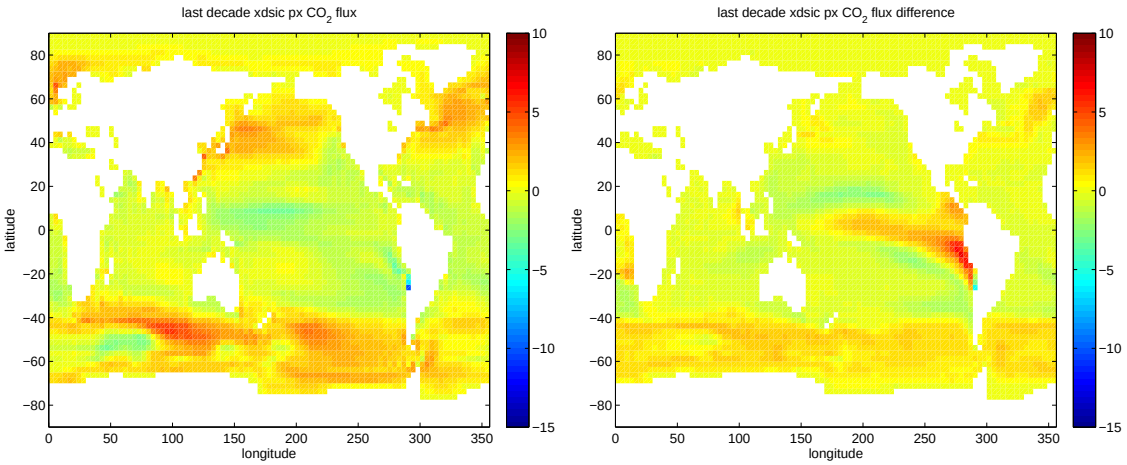

Figure 5.15: Job v_s & $P^s_{max} \uparrow$ last decade. Left plot: decadal air-sea CO_2 flux (mol CO_2 m^{-2} yr^{-1}). Right plot: difference in air-sea CO_2 flux to the last decade of the unperturbed job F_0 (Figure 5.14). CO_2 flux into the ocean is positive.

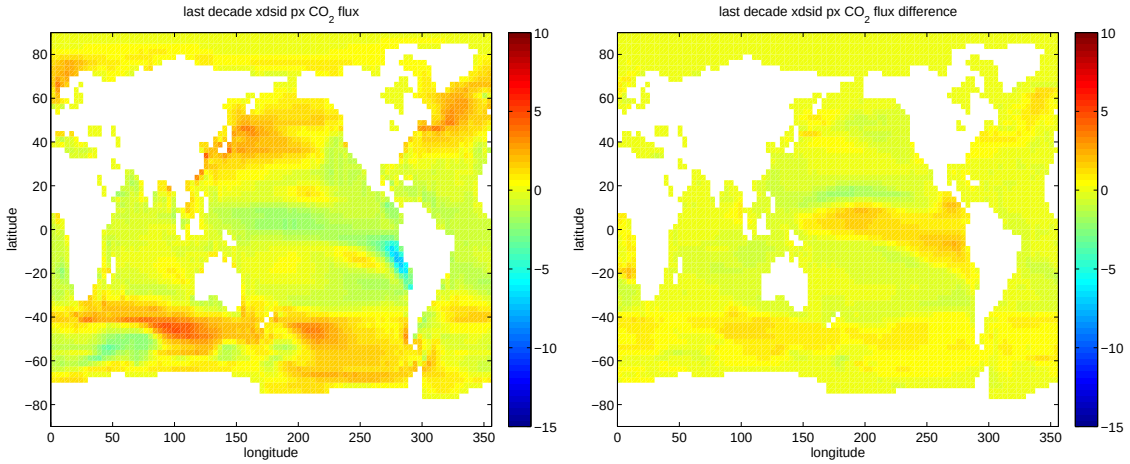

Figure 5.16: Job $v_s \uparrow$ last decade. Left plot: decadal air-sea CO_2 flux (mol CO_2 m^{-2} yr^{-1}). Right plot: difference in air-sea CO_2 flux to the last decade of the unperturbed job F_0 (Figure 5.14). CO_2 flux into the ocean is positive.

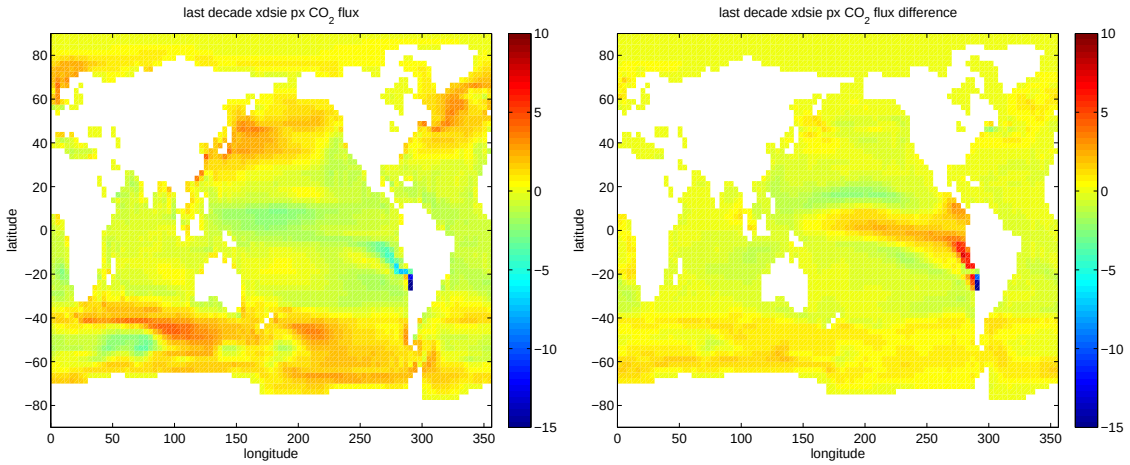

Figure 5.17: Job $P^s_{max} \uparrow$ last decade. Left plot: decadal air-sea CO_2 flux (mol CO_2 m^{-2} yr^{-1}). Right plot: difference in air-sea CO_2 flux to the last decade of the unperturbed job F_0 (Figure 5.14). CO_2 flux into the ocean is positive.

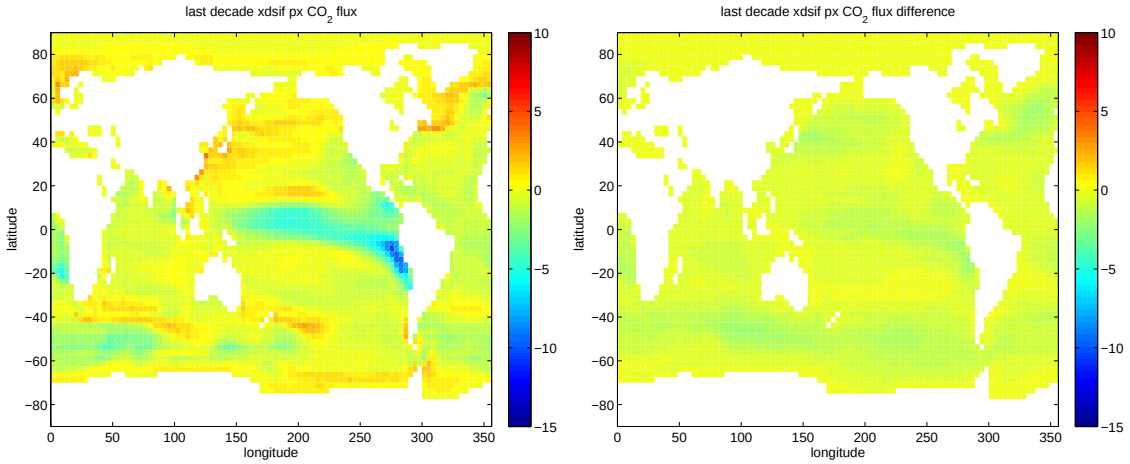

Figure 5.18: Job $\Upsilon_c \uparrow$ last decade. Left plot: decadal air-sea CO_2 flux (mol CO_2 m^{-2} yr^{-1}). Right plot: difference in air-sea CO_2 flux to the last decade of the unperturbed job F_0 (Figure 5.14). CO_2 flux into the ocean is positive.

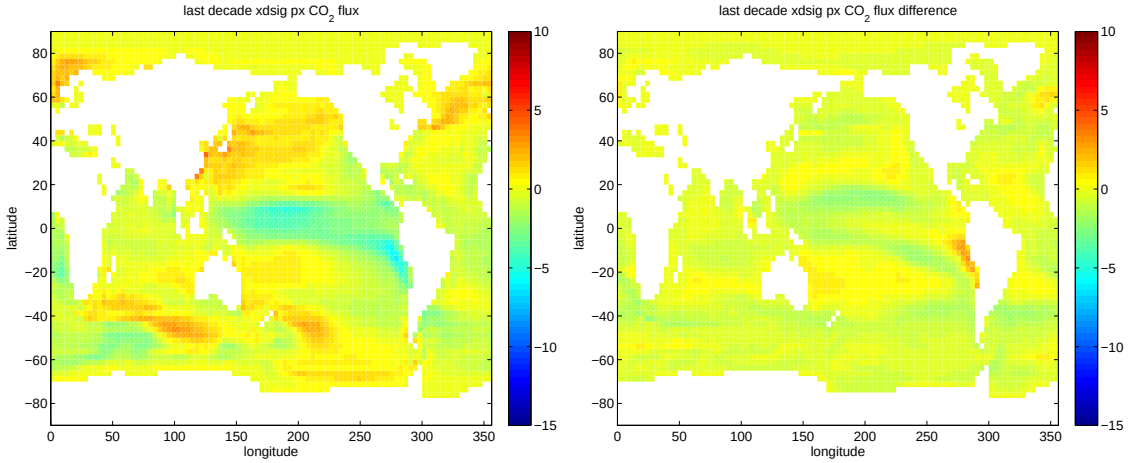

Figure 5.19: Job $P^s_{max} \downarrow$ last decade. Left plot: decadal air-sea CO_2 flux (mol CO_2 m^{-2} yr^{-1}). Right plot: difference in air-sea CO_2 flux to the last decade of the unperturbed job F_0 (Figure 5.14). CO_2 flux into the ocean is positive.

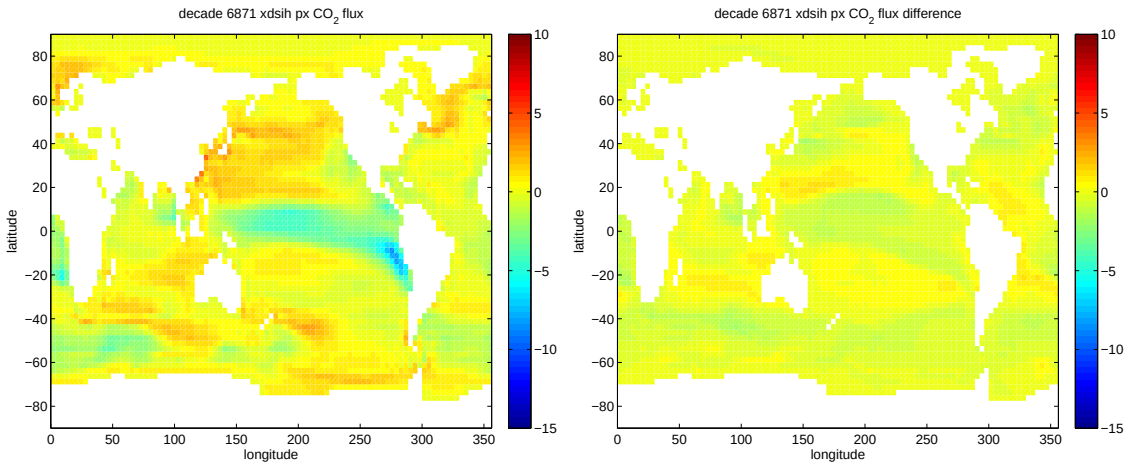

Figure 5.20: Job $\upsilon_s \downarrow$ last decade. Left plot: decadal air-sea CO_2 flux (mol CO_2 m^{-2} yr^{-1}). Right plot: difference in air-sea CO_2 flux to the last decade of the unperturbed job F_0 (Figure 5.14). CO_2 flux into the ocean is positive.

5.5.1.3 Long-term

Figure 5.3 shows the decadal mean net global air-sea CO_2 flux for job $\upsilon_s \uparrow$ extended to just over a thousand years (1080 years). This has allowed the ocean to absorb sufficient carbon for the DIC to equilibrate with the atmospheric carbon content—the final decade (108^{th}) of this job has a mean net global air-sea CO_2 flux of -0.0021 mol CO_2 m^{-2} yr^{-1}. This absorbed carbon has replaced that prevented from decaying from organic detritus by the faster detrital sinking rate. The total carbon absorbed by the ocean from the atmosphere to regain equilibrium as a result of this perturbation is $\approx$ 185 Pg C[5], which is an increase of around one and half percent to the $\approx$11 Pg C yr^{-1} exported as detritus from the surface ocean (see Section 1.5.2 and Figure 1.1) and is well within the error bounds of ocean export assessments [Najjar et al., 2007].

[5]This calculation assumes an ocean surface area of 362 million km^2 = 3.62×10^{14} m^2, and the molar mass of C = 12.01 g. 1 Pg = 1.0×10^{15} g.

5.6 Nutrient cycling, primary production and detrital export

There is no riverine input of nutrient to the ocean in FAMOUS, so the total nutrient contained in both organic structures (phytoplankton, zooplankton and detritus) and as labile nutrient is fixed—see Section 3.4.2. In the unperturbed job F_0 the nutrient cycle is well spun up resulting in stable ecosystem behaviour—the stable primary production seen in Figure 5.21 and stable CO_2 flux seen in Figure 5.2. Changing the behaviour of the ocean ecosystem by perturbing phytoplankton growth and detrital sinking parameters changes the use and supply of nutrient to the ecosystem, but the total quantity of nutrient remains constant. Table 5.6 summarises the effect of the different perturbations performed on the FAMOUS GCM on the primary production, detrital export and nutrient.

Sections 5.6.1 and 5.6.2 explore the effect of the perturbation of P^s_{max} and v_s on primary production and detrital export, and hence on the nutrient supply. The perturbation of Υ_c does not directly effect the nutrient supply as the effect of increased carbonate formation is the fixing of less carbon per unit nutrient (which increases the DIC concentration), not the ability to use nutrient (as with P^s_{max}) or changes to the amount of detritus that breaks down to nutrient (as with v_s). This can be seen by revisting the HadOCC model equations in Chapter 3 where Υ_c appears as a term in the equations governing DIC (Equation 3.17) and alkalinity (Equation 3.18) but not in those controling phytoplankton growth or nutrient. This possibly limits the model's ability to predict the true effects of large scale chemical change in the ocean (see Section 1.5.3 and 5.7).

5.6.1 P^s_{max} and production

Figure 5.21 shows the global mean annual primary production for the 100 year unperturbed job F_0, with a stable primary production of around 0.26 gC m^{-2} d^{-1} over the top 200m of the ocean. Figure 5.22 shows the same plot for the perturbed job P^s_{max} $\uparrow$, showing the large initial increase in primary production caused by the more efficient phytoplankton decaying as global labile nutrient supplies are depleted. There is also greater variability in the global primary production seen in Figure 5.22 caused by interannual nutrient depletion due to the increased phytoplankton efficiency. Figure 5.23 is a plot of the global mean annual nutrient (Mol N) for the years 6880 to 6884, showing variation in the global nutrient that matches the variation in primary production for these years in Figure 5.22. Figure 5.24 show the global plots of primary production for the last decade of these jobs, showing that the greatest increases in primary production in the perturbed job P^s_{max} $\uparrow$ are found in the upwelling Humboldt system to the west of South America leading out into the tropical Pacific, the upwelling Benguela system west of Africa, the seas around south-east Asia and to a lesser extent in the Southern Ocean. These are regions rich in nutrient, so primary production increases with a higher maximum photosynthetic rate.

In Section 5.5.1.1, job P^s_{max} $\uparrow$m explored the monthly mean air-sea CO_2 flux for the first five

Table 5.6: Effect of the different parameter perturbations on the use and supply of nutrient in the 100 year FAMOUS jobs.

Job	Effect on primary production, detrital export and nutrient supply.
F_0	Stable—no effect (see Figure 5.21).
v_s & P^s_{max} ↑	More nutrient taken up by phytoplankton, but less labile nutrient from breakdown of detritus in the upper ocean due to faster detrital sinking. This results in increased production in nutrient rich upwelling regions but reduces productivity elsewhere.
v_s ↑	Less labile nutrient supplied by detrital breakdown in upper ocean reducing primary productivity.
P^s_{max} ↑	More nutrient used by greater productivity in upwelling regions resulting in the creation of more detritus. This increase in primary production depletes nutrient supply to rest of the surface ocean reducing productivity and detritus creation away from upwelling regions.
Υ_c ↑	No change to the use of nutrient by phytoplankton. The formation of carbonate does not alter the amount of nutrient used by phytoplankton (see Section 5.6).
P^s_{max} ↓	Less primary production in nutrient rich upwelling regions, increasing the nutrient supply to the rest of the upper ocean and hence expanding the overall area of production but reducing the total global primary production. Detritus creation follows the same pattern.
v_s ↓	More nutrient in upper ocean from the breakdown of detritus allowing increased primary production, which creates more detritus in the upper ocean.

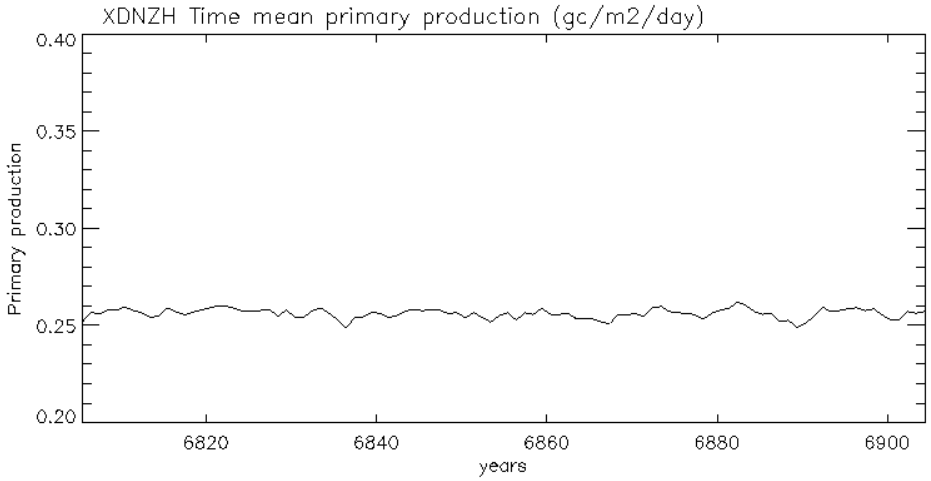

Figure 5.21: Global mean annual primary production over the top 200m of the ocean (gC m^{-2} d^{-1}) for the unperturbed job F_0 showing stable primary production.

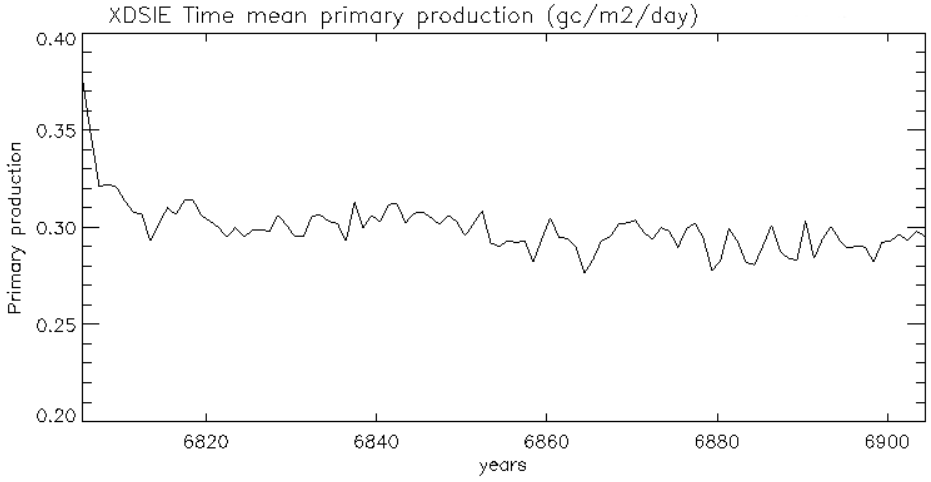

Figure 5.22: Global mean annual primary production over the top 200m of the ocean (gC m^{-2} d^{-1}) for job P^s_{max} ↑ showing initial response to perturbation decaying as the nutrient supply is depleted. The greater interannual variability to that seen in Figure 5.21 is due to a cycle of large scale nutrient depletion by the more efficient phytoplankton, leading to reduced production which allows nutrient supplies to temporally replenish before being depleted again (see Figure 5.23).

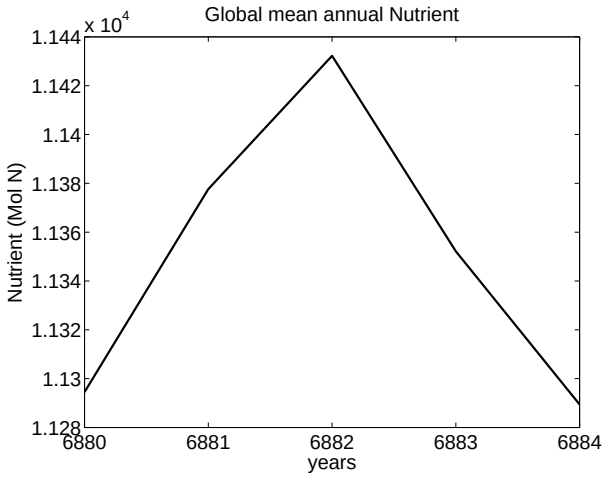

Figure 5.23: Global mean annual nutrient (Mol N) in the top four ocean levels of FAMOUS for the years 6880 to 6884. This matches the interannual variability in primary production seen for these years in Figure 5.22, showing that the more efficient phytoplankton cause large scale interannual nutrient depletion.

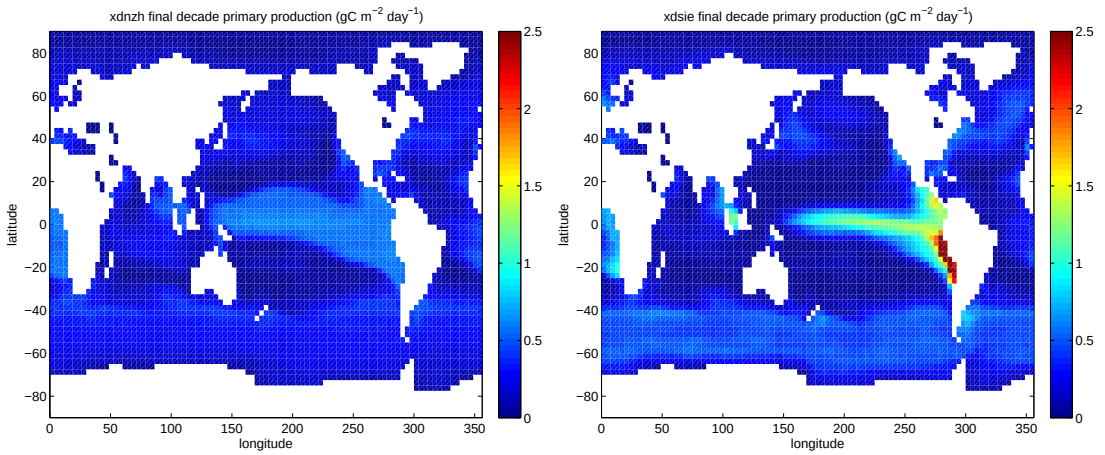

Figure 5.24: Mean primary production over the top 200m of the ocean (gC m^{-2} d^{-1}) for the last decade of unperturbed job F_0 (left), and job P^s_{max} ↑—(right). Colour scale is the same as in Figures 5.25 to 5.28.

years with the value of P^s_{max} perturbed up. In Figure 5.6 it is noted that as well as increasing the air-sea CO_2 flux into the ocean as expected, the seasonal CO_2 flux cycle is altered by the increase in the value of P^s_{max}. When compared with the unperturbed monthly job F_0m (Figure 5.4), the amplitude of the first peak in the annual CO_2 flux cycle is decreased, and the amplitude of the second peak increased when P^s_{max} is perturbed up. Here, in Figures 5.25 and 5.26 (unperturbed—job F_0m), and Figures 5.27 and 5.28 (job P^s_{max} ↑m), this effect is explored further by plotting the primary production (over the top 200m of the water column in gC m^{-2} d^{-1}) for each month of the fourth year of these two jobs (the difference described between the CO_2 flux annual cycles is most marked for the fourth year in Figures 5.4 and 5.6).

Figures 5.25 and 5.26 (unperturbed—job F_0m) show the expected pattern for primary production through the year (see Section 1.5.2), with very low productivity in the gyres and slightly higher productivity year round in the tropics. In the northern summer, high productivity occurs in the north Atlantic (May and June in Figure 5.25), while in the southern summer, high productivity is shown in the Southern Ocean (November and December in Figure 5.26). The results for job P^s_{max} ↑m in Figures 5.27 and 5.28 again show very little primary production in the gyres, but greater primary production in the more productive well-mixed regions due to the increase in the maximum photosynthetic rate enabling phytoplankton to better exploit the abundant nutrient.

Looking in greater detail at Figures 5.27 and 5.28, increasing the maximum photosythetic rate has five main effects on the primary production calculated by FAMOUS. Firstly, the areas adjacent to these more productive regions show a reduction in primary productivity. This is due to nutrient supplies to these regions being used up in the adjacent upwelling regions by the now faster growing phytoplankton. This is most clearly seen in the Pacific—compare Figures 5.27 and 5.28 to Figures 5.25 and 5.26—where the areas of low productivity (the subtropical gyres) have

increased in size due to the higher primary production in the upwelling region of the Humbolt current depeleting the supply of nutrient. Figure 5.29 compares the nutrient concentrations in the most productive upper 40m of the ocean for the fourth year of the jobs F_0m (unperturbed), and P^s_{max} ↑m explored here, showing the decrease in area of the nutrient rich tropical Pacific caused by the greater uptake of nutrient by the faster growing phytoplankton nearer to the upwelling nutrient source.

Secondly, the waters of the tropical Pacific, and the waters around south-east Asia show a small increase in primary productivity throughout the year. In these tropical regions, insolation is constant throughout the year, so an increase in the value of P^s_{max} understandably increases the productivity.

Thirdly, the productivity of the waters off south-west Africa and off the western coast of South America (linking with production in the tropical Pacific) is increased. These are both major upwelling regions—off west Africa the Benguela current system, and up the western shore of South America the Humboldt current system—transporting cold, nutrient rich waters to the surface [Fasham, 2003]. With an increased maximum photosynthetic rate, the primary production increases in these regions due to the plentiful nutrient supply, particularly during the later months of the year (September to December in Figure 5.28), when the upwelling in both these regions is strongest [Fasham, 2003].

Fourth, the increase in P^s_{max} leads to an increase in the primary production of the north Atlantic in the northern summer (April, May and June in Figure 5.27). The value of P^s_{max} controls the maximum photosynthetic rate of phytoplankton under conditions of abundant sunlight (see Section 3.2.8), so during the long days of northern summer, the primary productivity of light bathed northern waters with sufficient nutrient is increased.

Lastly, during the southern summer (November and December in Figure 5.28, and January in Figure 5.27), there is a large increase in the productivity of the Southern Ocean due to the abundance of sunlight and nutrient as before. The increased primary production in the Southern Ocean (and to a lesser extent that off western South America and west Africa) is responsible for the increased amplitude of the seasonal cycle of air-sea CO_2 flux in the latter part of the year seen in Figure 5.6.

However, as discussed in Section 1.5.2, primary production in the Southern Ocean is strongly limited, not by the availability of nitrogen, which is abundant in these well mixed waters (see Figure 5.30), but by the availability of iron, a crucial micronutrient. Phytoplankton growth in HadOCC (and FAMOUS) is limited only by the availability of sunlight and nitrogen, so the model can over-estimate primary production in 'high nitrate low chlorophyll' regions where essential micronutrients are in short supply. This demonstrates a limitation of the simplicity of the structure of the ocean biogeochemical processes in HadOCC and FAMOUS. This is not unique, as other

GCMs have been found to overestimate the primary productivity of the Southern Ocean when compared to estimates based on remotely sensed ocean colour [Carr et al., 2006].

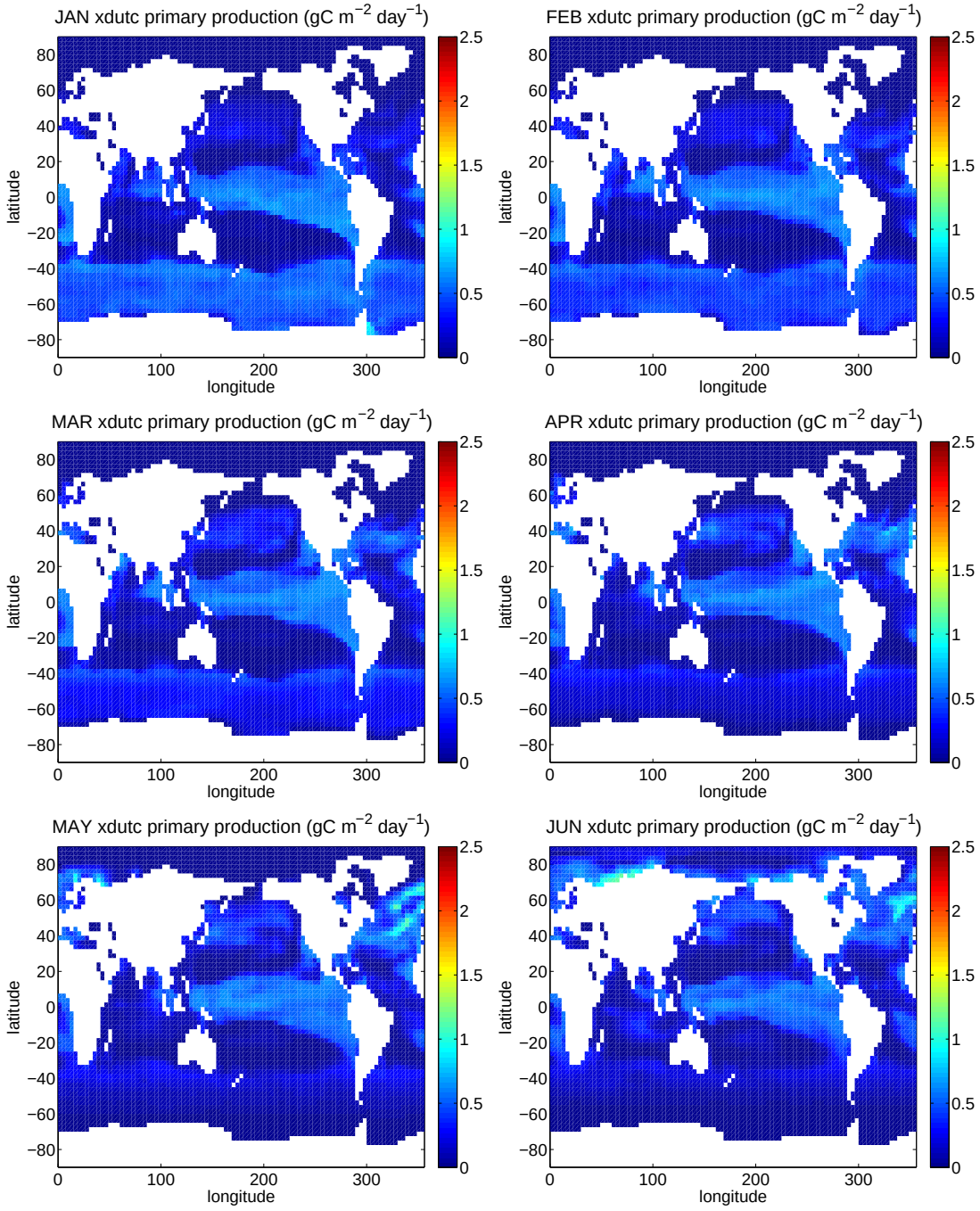

Figure 5.25: Primary production over the top 200m of the ocean (gC m^{-2} d^{-1}) for the first six months—January (top left) to June (bottom right)—for the fourth year of job F_0m (unperturbed).

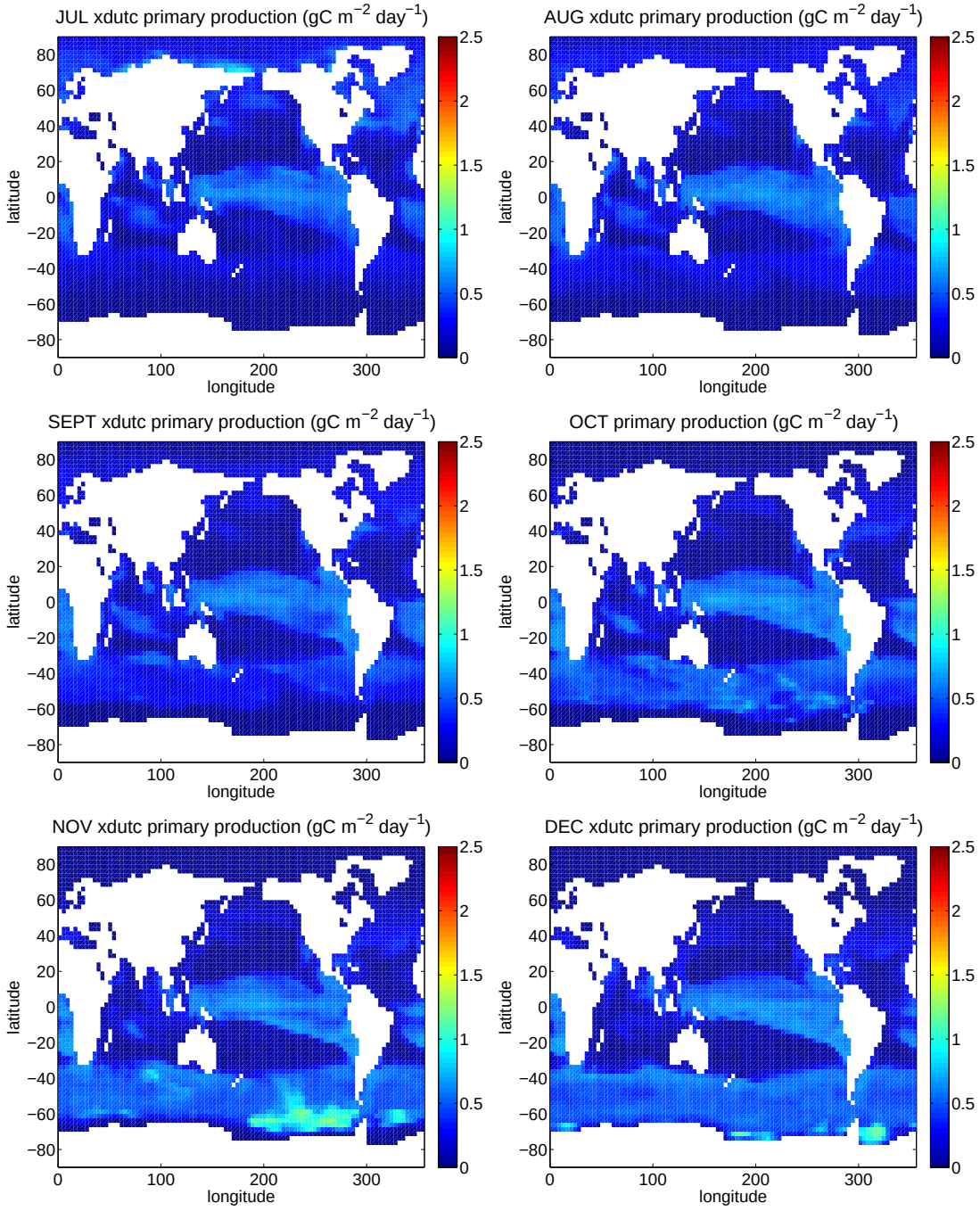

Figure 5.26: Primary production over the top 200m of the ocean (gC m^{-2} d^{-1}) for the last six months—July (top left) to December (bottom right)—for the fourth year of job F_0m (unperturbed).

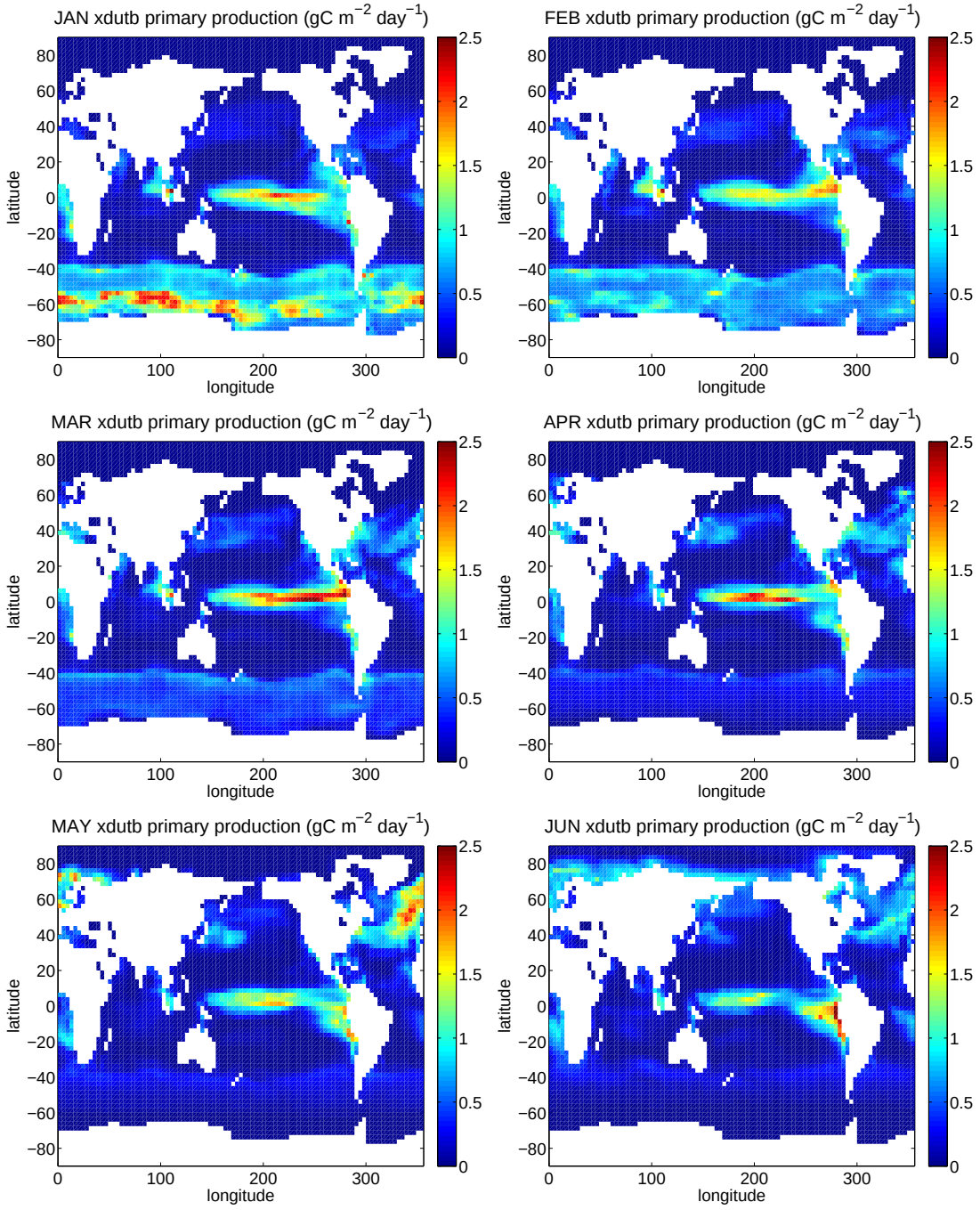

Figure 5.27: Primary production over the top 200m of the ocean (gC m^{-2} d^{-1}) for the first six months—January (top left) to June (bottom right)—for the fourth year of job P^s_{max} ↑m.

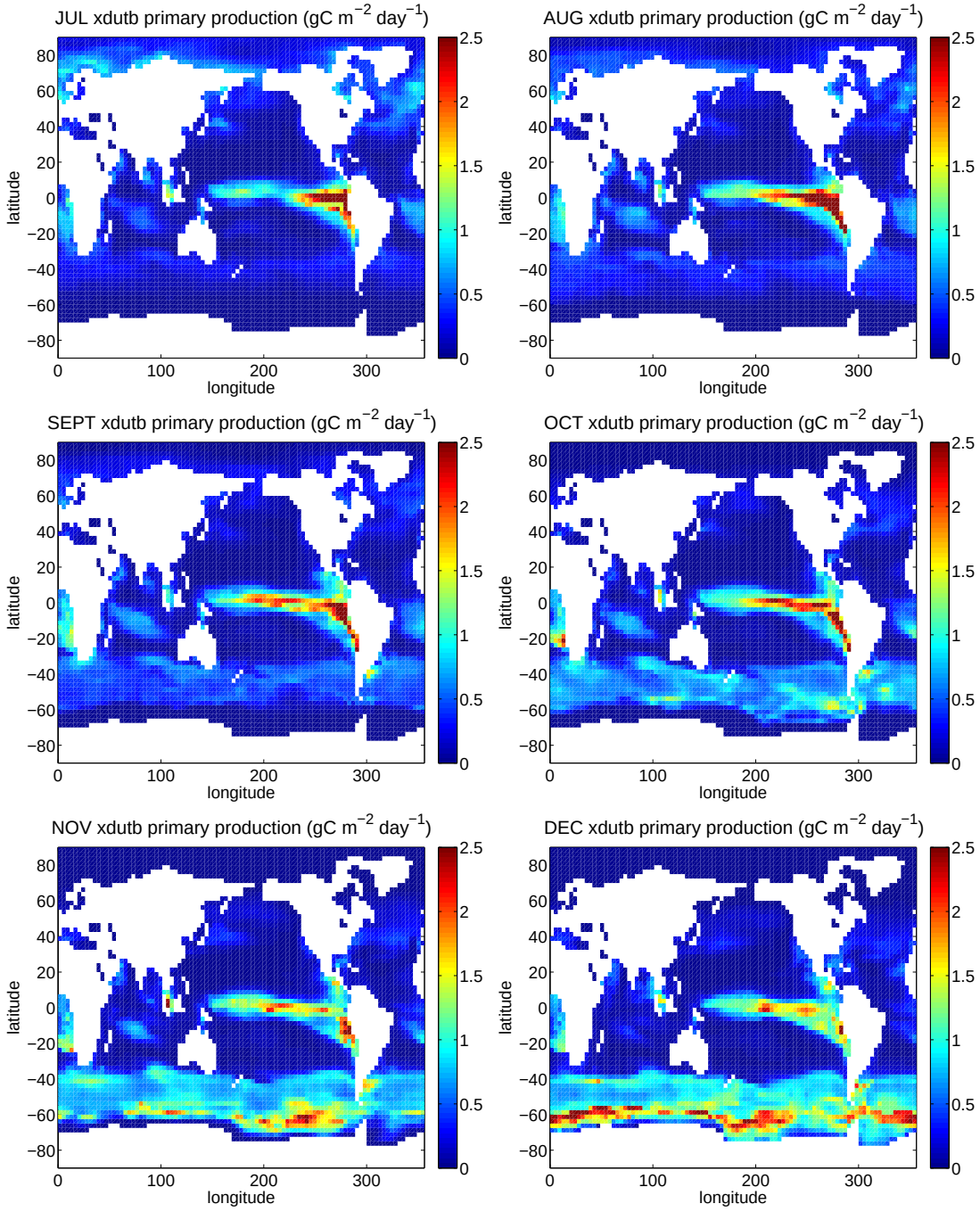

Figure 5.28: Primary production over the top 200m of the ocean (gC m^{-2} d^{-1}) for the last six months—July (top left) to December (bottom right)—for the fourth year of job P^s_{max} ↑m.

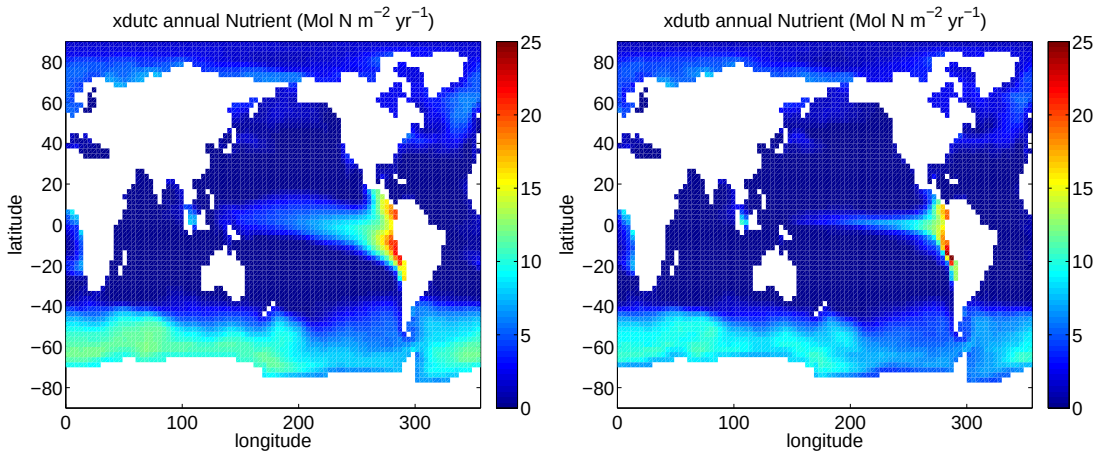

Figure 5.29: Annual nutrient (Mol N m^{-2} yr^{-1}) for the fourth year of the unperturbed job F_0m (left plot), and the fourth year of the job P^s_{max} ↑m (right plot) showing the nutrient depletion in the gyres due to increased phytoplankton growth.

5.6.2 Detrital export

In addition to having a large effect on the calculation of the air-sea CO_2 flux, the value of the detrital sink rate v_s governs the rate of export of detritus to the deep ocean, and hence influences the amount of detritus that breaks down to nutrient in the upper mixed ocean and the primary production. Here, the three FAMOUS runs in which v_s is perturbed (jobs v_s ↑, v_s ↓ and v_s & P^s_{max} ↑), are used to look at the change to detrital export due to this perturbation, and the effect of this change on the nutrient supply and primary production.

Detritus sinks through the water column at the daily rate prescribed by the value of v_s. However, the mixing of the upper ocean can cycle this detritus, slowing or increasing the overall rate at which it is transported to the deep ocean. The mixed layer depth determines the extent of the upper mixed ocean. Unless lateral transport moves detritus to a region with a deeper mixed layer, detritus that sinks below the mixed layer depth in FAMOUS sinks through the deep ocean where it is either remineralised and transported slowly back towards the surface by large-scale ocean circulation, or, if it reaches the seafloor, is reintroduced to the top of the water column (see Section 3.4.2).

The ocean in FAMOUS has 20 vertical depth levels in the water column, which gradually increase in size from a few metres near the surface to around 600 metres in the deeper areas of the ocean (see Section 3.4). Figure 5.30 shows the mean annual mixed layer depth for the final decade of job F_0. The mixed layer depths for the jobs in which v_s is perturbed do not differ significantly as the perturbation of the detrital sink rate has no effect on the ocean circulation. The mean mixed layer depth of the ocean for the final decade of job F_0 is 45.11m. From the surface downwards, the midpoint of the 5^{th} FAMOUS depth level is at 47.85m, just below the mean mixed layer depth. Here, the concentration of detritus in the next level below this—the 6^{th} depth level from

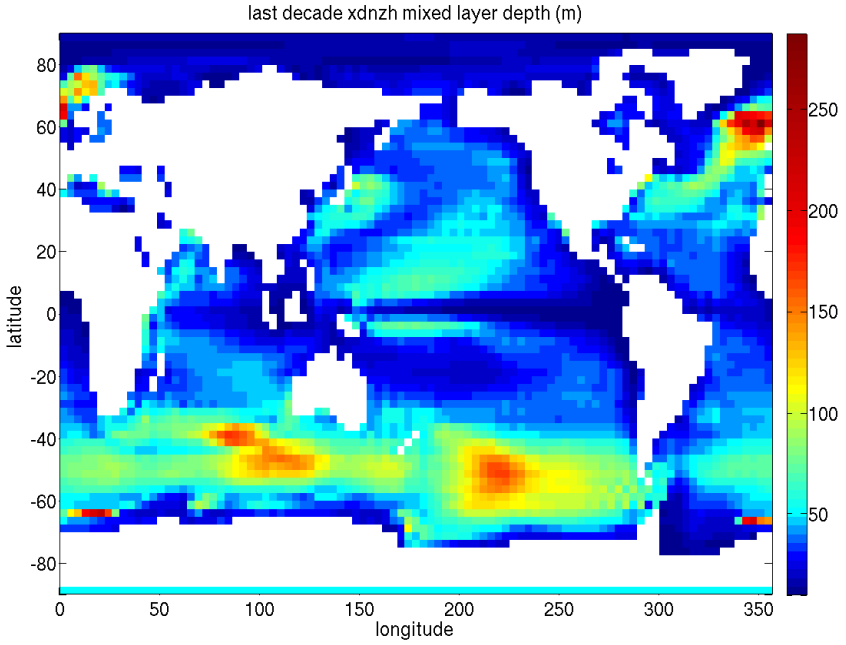

Figure 5.30: Annual mean mixed layer depth (m) for final decade of job F_0.

55.5m to 78.5m deep—during the final decade of the jobs in which v_s is perturbed are compared with that for the unperturbed job.

Figure 5.31 shows the mean concentration of detritus in mmol C m^{-3} of the 6^{th} ocean layer (midpoint at 67m) for the final decade, for the unperturbed job F_0, and the jobs in which the value of the detrital sink rate v_s is perturbed—job $v_s \uparrow$, job $v_s \downarrow$[6] and job v_s & $P^s_{max} \uparrow$. The concentration of detritus in the ocean level centered at 67m depth varies from zero in the gyres, to around 1.4 mmol C m^{-3} for the unperturbed job F_0. In the jobs in which only v_s is perturbed, the range is from zero to around 1.5 mmol C m^{-3}, while for job v_s & $P^s_{max} \uparrow$ higher detrital concentrations of up to 5 mmol C m^{-3} are seen. As expected, high concentrations of detritus are seen in the areas of high productivity, as detritus is created by the mortality and grazing of phytoplankton by zooplankton.

Looking at the differences between the three perturbed jobs and the unperturbed job F_0 in Figure 5.31, it can be seen that the increase in the speed of detrital sinking in job $v_s \uparrow$ reduces the concentration of detritus from the tropical Pacific, but has little effect elsewhere—notably in the Southern Ocean and the north-east Atlantic. This is contrary to the simple expectation that an increase in the detrital sink rate will result in increased detrital export. The explanation for this is that the increased sink-rate removes detritus that breaks down to nutrient in the unperturbed job, reducing the available nutrient in the tropical Pacific. Comparing this to the corresponding

[6] As before, the final decade used is that before the change in atmospheric timestep.

primary production plots in Figure 5.32, it can be seen that the perturbation has reduced the north-south range of the area of high productivity in the tropical Pacific, but has had little effect elsewhere, principally in the Southern Ocean (compare the plot for job $v_s \uparrow$ with that for the unperturbed job F_0 in Figure 5.32). The increased sink rate has little effect on production here as the Southern Ocean waters are better mixed (see Figure 5.30).

The reduction to the sink rate of detritus in job $v_s \downarrow$ (where the value of v_s is perturbed down), is seen in Figure 5.31 to increase the detrital concentration in low latitudes. Again, this counters the expectation that a reduction in the detrital sink rate should reduce the detrital export. As for job $v_s \uparrow$ above, the explanation for this is in the effect of the perturbation of the sink rate on the availability of nutrient. Looking at the corresponding primary production plot in Figure 5.32, this perturbation has substantially increased the area of higher productivity. This is due to the decrease in sink rate allowing more of the detritus to be broken down to nutrient which enables more primary production than in the unperturbed job F_0.

In job v_s & $P^s_{max} \uparrow$, both the detrital sink rate and the maximum rate of photosynthesis are increased. Figure 5.31 shows that the effect of these combined perturbations is to significantly reduce the distribution of higher detritus concentration in the 6^{th} ocean level in the tropical Pacific, but to increase that seen in the waters off South America. There is also a slight increase in detrital flux in the Southern Ocean. Looking again at the corresponding primary production plot in Figure 5.32, and comparing this with Figure 5.24—the primary production for job $P^s_{max} \uparrow$, where only P^s_{max} is perturbed up (N.B. different scale)—it can be seen that the change in the sink rate has had little effect compared with the change resulting from the perturbation of P^s_{max}. The increased detrital concentration is found in the regions of high primary production resulting from the increase in P^s_{max}, with the reduction in the spatial distribution of the detritus resulting from the reduction in the spatial distribution of the phytoplankton as detailed in Section 5.6.1. Similarly, the slight increase in detritus concentration in the Southern Ocean can be seen to correspond with the increase in primary production in this region.

Looking back to the global mean air-sea CO_2 flux plots for the jobs explored here (Figure 5.2), it is clear that the perturbation of v_s, and resulting change in the detrital export influences the air-sea CO_2 flux as predicted from the results of Chapter 4, with an increase in the detrital sink rate increasing the air-sea CO_2 flux into the ocean. However, in Figure 5.32, increasing the detrital sink rate is shown to decrease the primary production and hence the uptake of dissolved CO_2. To explain this apparent contradiction, it must be remembered that the air-sea CO_2 flux depends only on the pCO_2 of the surface ocean. Detritus in the upper 100m of the ocean breaks down to nutrient and DIC at a rate set by the value of the shallow remineralisation parameter Rm_{shall} (see Section 3.2.8). The higher the detrital concentration in the sea-surface level, the more is broken down, with the resulting DIC increasing the pCO_2 sea of the surface, reducing the air-sea CO_2 flux into the ocean. Figure 5.33 shows plots of the concentration of detritus in the top ocean level

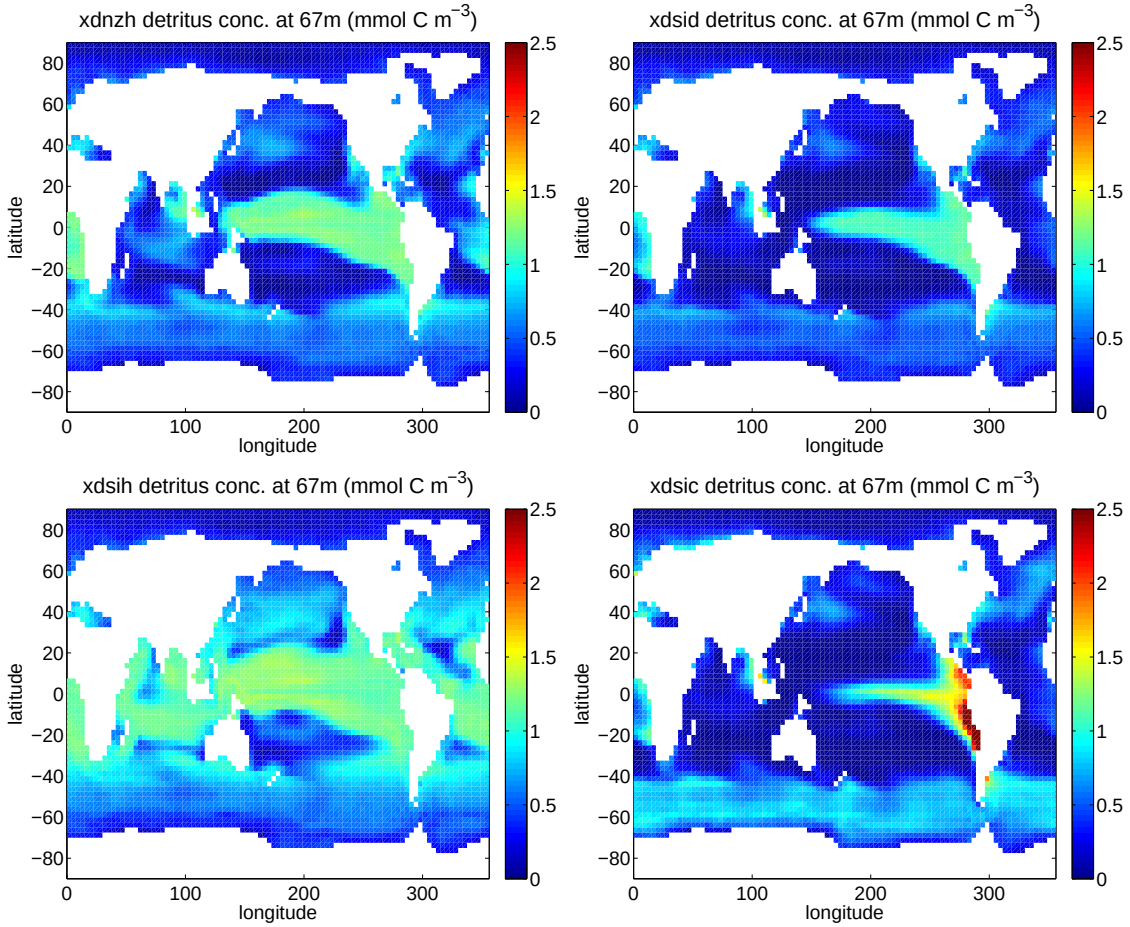

Figure 5.31: Plots of mean concentration of detritus (mmol C m^{-3}) of the sixth ocean depth level (55.5m to 78.5m deep, midpoint at 67m depth), for the final decade of job F_0 (unperturbed—top left), job $v_s \uparrow$ (top right), job $v_s \downarrow$ (bottom left), and job v_s & $P^s_{max} \uparrow$—bottom right).

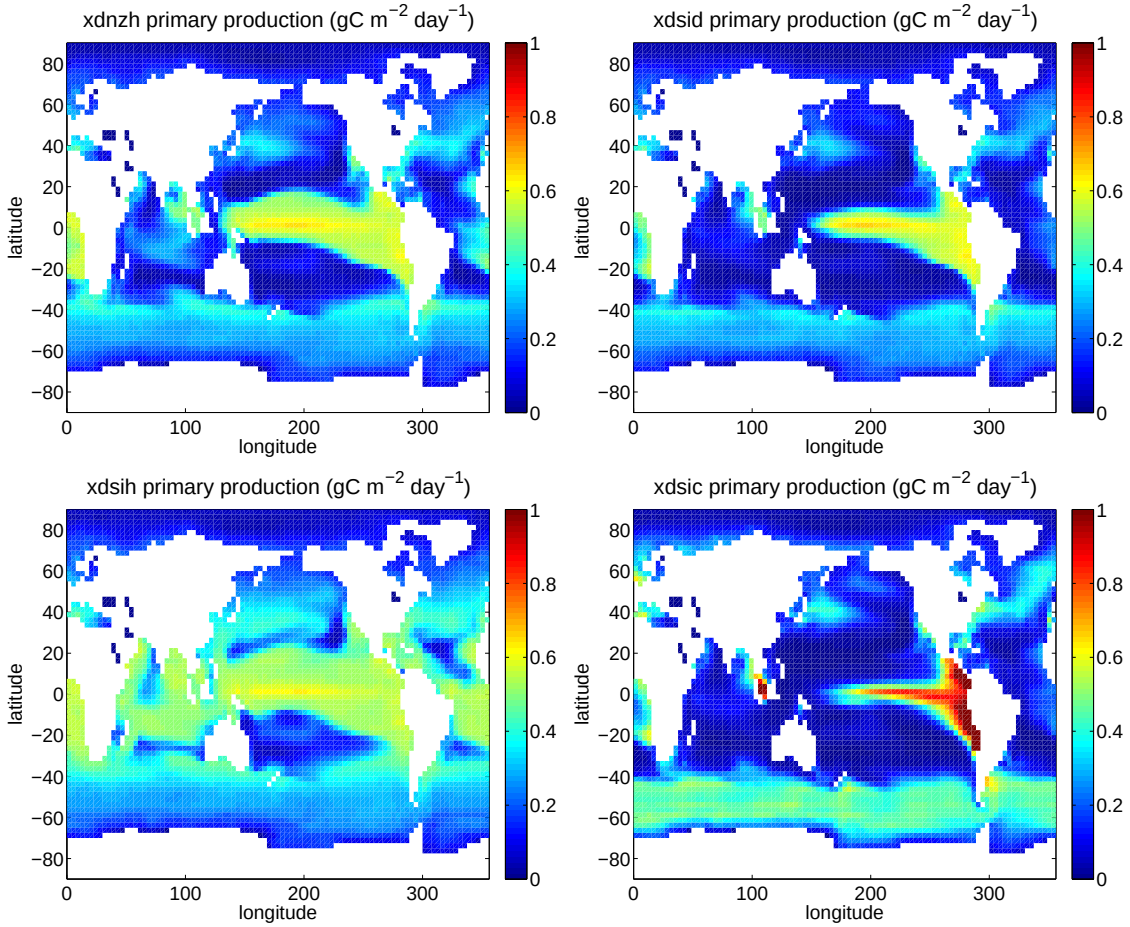

Figure 5.32: Mean primary production (gC m^{-2} d^{-1}) for the final decade of job F_0 (unperturbed—top left), job $v_s \uparrow$ (top right), job $v_s \downarrow$ (bottom left), and job v_s & $P^s_{max} \uparrow$—bottom right). N.B. for clarity a different scale is used to that in Figures 5.25 to 5.26 and Figure 5.24.

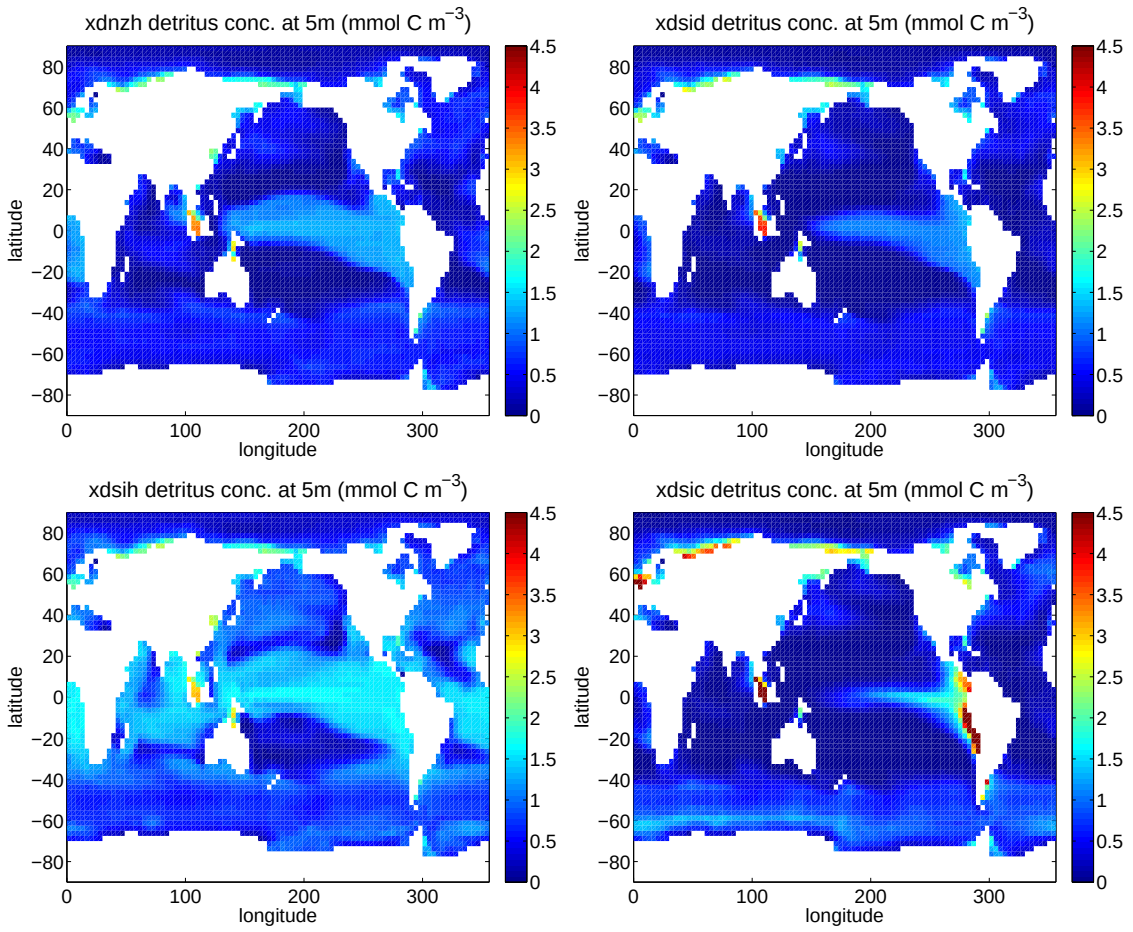

Figure 5.33: Plots of mean concentration of detritus (mmol C m^{-3}) of the top ocean level (0m to 10m deep, midpoint at 5m) for the final decade of job F_0 (unperturbed—top left), job $v_s \uparrow$ (top right), job $v_s \downarrow$ (bottom left), and job v_s & $P^s_{max} \uparrow$ (bottom right).

of FAMOUS (from 0m to 10m depth), for the unperturbed job F_0 and the jobs in which the value of v_s is changed. The plots for job $v_s \uparrow$ and $v_s \downarrow$ show that the greater the value of v_s, the lower the surface level concentration of detritus, explaining the effect on the air-sea CO_2 flux shown in Figure 5.2. The plot for job v_s & $P^s_{max} \uparrow$, shows the greater primary production producing more detritus but over a reduced area as expected from Figure 5.32. The greater CO_2 flux into the ocean for the combined perturbations of v_s and P^s_{max} (job v_s & $P^s_{max} \uparrow$), as opposed to the individual perturbations (job $v_s \uparrow$, and $P^s_{max} \uparrow$) seen in Figure 5.2, is due to the combined effect of the greater uptake of CO_2 by increased phytoplankton growth, and reduced sea-surface level DIC, due to the faster removal of the detritus produced from the surface level by more rapid sinking.

5.7 Discussion

The evaluation of the effects of parameter uncertainty has become a key part of interpreting the results of GCM climate simulations [Randall et al., 2007]. These evaluations have largely concentrated on the effect of perturbation to parameters in the atmospheric component of GCMs—e.g., Collins et al. [2007], Stainforth et al. [2005] and Murphy et al. [2004]. Recently studies have been undertaken to assess the effect of parameter uncertainty in the ocean physics of coupled atmosphere ocean GCMs [Brierley et al., 2008], finding that while the global impact of perturbations to ocean physics parameters are small compared to those found for atmospheric parameter perturbations (particularly those associated with clouds [Webb et al., 2006; Dufresne and Bony, 2008]), there are detectable variations in regional climate. Smith and Marotzke [2008] examine the influence of different ocean configurations on the modelled uptake and storage of carbon in the north Atlantic. While they find that the differences in biogeochemical models have less effect on carbon uptake than the differences in the physical representations, they conclude that changes in biological export of surface carbon have the potential to modify global ocean uptake of CO_2. The reaction of the global carbon cycle to anthropogenic forcing is known to be important in determining future climate, with carbon-cycle feedbacks expected to increase the warming due to anthropogenic activity [Friedlingstein et al., 2006; Jones et al., 2006; Cox et al., 2000; Sarmiento et al., 1998]. Chuck et al. [2005] study the oceanic response to carbon emissions over the next century using three ocean carbon cycle models, concluding that overall positive feedbacks are more likely (a decrease in carbon uptake by the ocean by 2100), but they are at most a quarter (a non-negligible quantity) of the size of those proposed for the terrestrial carbon cycle feedback of around 5 Pg C y^{-1} in the work of Cox et al. [2000].

The results of Section 5.5.1 show that the uncertainty in the biological parameters controlling phytoplankton growth near the surface (P^s_{max}), the export of detritus (v_s), and the formation of carbonate (Υ_c), have a detectable effect on the air-sea CO_2 flux calculated by the FAMOUS GCM. The interpretation of these results is limited by the de-coupled carbon cycle of the FAMOUS set-up, but indicates the relative importance of uncertainty in biological parameters for the calculation of oceanic carbon uptake in GCMs (see Section 5.7.1). The parameterisation of the relationship between wind speed and the gas transfer velocity is generally found to be the greatest source of error in the calculation of the air-sea CO_2 flux, but the accurate calculation of the surface pCO_2^{sea} is also crucial to predict the air-sea CO_2 flux [Fangohr et al., 2008; Rutgersson et al., 2008]. Here, it is shown that changes in the values of key biological parameters quickly influence the surface pCO_2^{sea} to a sufficient degree to change the air-sea CO_2 flux to an order comparable with that of current estimates. Similar changes to air-sea CO_2 flux are found in the models of Schneider et al. [2008], where the sensitivity of the air-sea CO_2 flux to different formulations of particulate fluxes in the ocean is studied, indicating that this degree of sensitivity is plausible and not unique to the FAMOUS GCM.

Perhaps most surprising is the size of the change associated with perturbation of the rain ratio

parameter Υ_c which for the one hundred years completed here is comparable with current ocean carbon uptake estimates. As explored in Sections 5.5.1.1 and 5.6, the formulation of the rain ratio in HadOCC means that changes to its value alter the carbon to nutrient ratio of phytoplankton (higher Υ_c gives a lower C:N ratio), but does not directly influence the uptake of nutrient by phytoplankton. This means that the effect of the perturbation of the rain ratio is not moderated by it causing changes to the nutrient supply, in contrast to the perturbations of the photosynthetic rate and the detrital sinking rate which affect both the DIC and nutrient concentration. As a result of this it is believed that the time taken for the ocean DIC to equilibrate with the fixed atmospheric pCO_2^{air} will be longer than that seen for the other perturbations (around a thousand years in the case of the upwards perturbation of $_{vs}$—see Figure 5.3). In fact, as it is well established that coccolithophores (the major calcifying phytoplankton group) can thrive in comparatively nutrient depleted regions due to their ability to survive periods of nutrient shortage better than other large phytoplankton types such as diatoms [Gregg and Casey, 2007; Fasham, 2003], changing the global rain ratio should alter nutrient distribution and use. The strength and formulation of the rain ratio is the subject of much current debate (see Table 4.1), but it is clear that the use of a single global value that is independent of nutrient uptake is a vast simplification of the true picture [Loubere et al., 2007]. While the perturbation applied in this study is at the upper end of estimates of a global average rain ratio, the results indicate the importance of accurately modelling the carbonate cycle for predicting the carbon uptake by biological processes in the ocean.

While the results of this GCM work concur with the expectations from the results of Chapter 4, the extension to a global 3D scheme reveals in greater detail how perturbations to these parameters effect the biologial uptake of DIC, and hence the surface pCO_2^{sea} and the resulting air-sea CO_2 flux. In the FAMOUS 3D ocean mixing scheme, the relationship between primary production, detritus creation and nutrient supply is shown to influence the regional distribution and strength of outgassing and ingassing regions. Increasing the productivity and increasing the removal of detritus from the mixed layer both deplete nutrient in areas away from upwelling ocean regions, resulting in a reduction in production, and its effect on the surface pCO_2^{sea} in these areas. By contrast, reducing the productive ability of phytoplankton or reducing the removal of potential nutrient by detrital sinking results in greater areas of production (see Section 5.6). This behaviour is not apparent in a 1D mixing scheme such as that of HadOCC-GOTM used in Chapter 4 where the use of a relaxation to a fixed profile to replenish nutrients (see Section 3.3) can artificially support the system. This shows the importance of studying ocean biogeochemical processes in a full 3D mixing framework, and highlighs a potential problem with the practice of using 1D models to tune parameters for 3D GCMs, as is the case with HadOCC in FAMOUS [Palmer, 1998].

The reaction of the ocean ecosystem and its resulting influence on the global carbon cycle to increasing ocean temperatures, decreasing ocean pH and other changes to the ocean environment due to anthropogenic activity is uncertain, e.g. Friedlingstein et al. [2006]; Doney et al. [2009b]. However, it is possible that the ocean ecosystem may change sufficiently to alter the bulk

properties represented by the parameters investigated here, such as a change in the global rain ratio due to a large reduction in calcifying biomass resulting from ocean acidification (see Section 1.5.3), and a corresponding change in average photosynthetic ability as the dominance and distribution of phytoplankton types change in response. This work shows that changes to these bulk properties can have a noticeable effect on the ocean's role in the global carbon cycle creating climate change feedbacks that should be included and explored in climate simulations.

5.7.1 A coupled situation

The interpretation of the results of this work is limited by the current uncoupled set-up of the carbon cycle in FAMOUS (see Section 5.3). However, it is possible to use these results to infer aspects of the probable effects of biogeochemical parameter uncertainty in a set-up with a coupled pre-anthropocene (un-driven) atmospheric CO_2 component, and a coupled and externally modified (driven) atmospheric CO_2 component. In such set-ups, while the size of the change in the net global air-sea CO_2 flux is expected to be different, the direction of the change seen for the different perturbations should be the same as found here—increasing the ability of the ocean ecosystem to uptake dissolved CO_2 will still increase the air-sea CO_2 flux into the ocean, while decreasing the biological uptake will decrease the air-sea CO_2 flux into the ocean.

First, consider a set-up with coupled atmosphere and ocean carbon, but with no external addition to the atmospheric CO_2 content. The unperturbed results above showed a near-zero net air-sea CO_2 flux, and it is reasonable to expect that coupling the carbon in the ocean and atmosphere would not significantly change this situation. For the upwards perturbation of P^s_{max} and/or v_s, the decreased pCO_2^{sea} will reduce the global atmospheric CO_2 concentration (and the pCO_2^{air}) until equilbrium is once again reached. This equilibrium will be achieved more quickly than seen in the results of the work above for a constant pCO_2^{air} as the atmospheric pCO_2^{air} will reduce due to the additional ocean uptake. For the downwards perturbation of P^s_{max} or v_s, the return to equilibrium between the atmosphere and ocean will again happen more quickly than in the un-coupled situation, as the pCO_2^{air} will increase due to the outgassing caused by reduced biological uptake. For the same reason, a less prolonged period of outgassing will also be seen in the case of increasing the rain-ratio (Υ_c) value. Overall, in a coupled and un-driven set-up the effect of the ocean biogeochemical parameter uncertainty is expected to be less than the initial effects found in the results presented here (see Section 5.5.1.1). Additionally, the net annual global air-sea CO_2 flux will tend to near zero more quickly as the global average pCO_2^{air} and pCO_2^{sea} will equilibrate more rapidly. As such, the results of this work can be seen to set the bounds on the size of the initial effect of the biological parameter uncertainty in a coupled situation.

Secondly, consider a coupled situation with an anthropogenically modified atmospheric CO_2 concentration. Here, the results will depend on the size and rate of the external addition to the atmospheric CO_2 content. The unperturbed model will react to the increased atmospheric CO_2

with increased uptake due to the higher pCO_2^{air}. For the upwards perturbation of P^s_{max} and/or v_s, it is noted in Section 5.5.1.2 above that the current situation could be interpreted as one in which the atmospheric CO_2 is modified by the addition of CO_2 to maintain a constant pCO_2^{air}. If the external CO_2 addition is less than that needed to maintain a constant pCO_2^{air}, a lesser initial air-sea CO_2 flux into the ocean will result as the pCO_2^{air} will decrease and the carbon in the ocean and the atmosphere will equilibrate more quickly than in the uncoupled version. Alternatively, if the atmospheric CO_2 addition exceeds that needed to maintain a constant pCO_2^{air} in the perturbed situation, then the air-sea CO_2 flux into the ocean will be greater than that seen for the uncoupled set-up used here, and if the addition is sufficiently large, the ocean may not achieve equilibrium with the atmosphere.

In the case of the perturbations that reduce the net air-sea CO_2 flux into the ocean, a coupled and externally driven set-up will produce less initial outgassing than seen in the uncoupled set-up as the pCO_2^{air} will increase in response and equilibrium will again be achieved more rapidly. However, if the size of the external CO_2 addition is sufficient to keep the pCO_2^{air} greater than the pCO_2^{sea}, a net ingassing will result instead of net outgassing, though this ingassing will be less than that seen for an unperturbed coupled and driven situation as the ability of the ocean biology to uptake carbon has been reduced by the perturbations.

Given the scale of the effect of the perturbations in the uncoupled set-up, the current size and rate of the anthropgenic driving of the atmospheric CO_2 concentration is likely to be sufficient to give a pCO_2^{air} greater than the pCO_2^{sea} for all the parameter perturbations. This would result in the uptake of atmospheric carbon by the ocean, with the perturbations either increasing (v_s or P^s_{max} perturbed up) or decreasing (v_s or P^s_{max} perturbed down, Υ_c perturbed up) the size of the uptake. More difficult to predict is whether the perturbations would have a greater or lesser effect relative to the unperturbed CO_2 uptake in a coupled and driven set-up than seen in the present FAMOUS set-up. However, the similar order of the uncoupled results over the first hundred years of the changes to the biology with the current size of the ocean uptake ($\approx$ 2 Pg C), indicates that the size of the change in uptake in a perturbed coupled and atmospheric CO_2 driven simulation is likely to be of a similar order to that seen in the uncoupled set-up results. A repeated parmeter perturbation experiment with a GCM that enables coupling and external driving of the carbon cycle is needed to confirm this.

5.8 Summary

The results of this chapter show that uncertainty in the values of key ocean biogeochemistry parameters has a detectable effect on the uptake of atmospheric CO_2 by the ocean, with parameter perturbations resulting in initial changes to the ocean uptake of the order of current estimates of the ocean carbon sink (see Section 5.5.1 and Table 5.5).

An increase in the value of the detrital sink rate (v_s), or the value of the maximum rate of photosynthesis (P^s_{max}), increases the global net air-sea CO_2 flux into the ocean, while decreasing the value of these parameters decreases the global net air-sea CO_2 flux. In both cases, the initial effect of changes in these parameters gradually decreases as the ocean uptakes carbon to achieve equilibrium with the atmosphere. Changing the value of the maximum photosynthetic rate has both a very quick (less than one month) and a greater initial impact on the global net air-sea CO_2 flux than changing the value of the detrital sink rate. Changing the value of the detrital sink rate v_s takes longer (around a year) to influence the global air-sea CO_2 flux, and causes a lesser initial change than the perturbation of the value of the maximum photosynthetic rate. The upwards perturbations of the detrital sink rate v_s from 10 to 15.38 m d^{-1} and of P^s_{max} from 0.6 to 1.12 d^{-1} (see Section 5.2) performed here have a similar effect on the global air-sea CO_2 flux calculated in FAMOUS, increasing the ocean uptake by 0.37 and 0.32 Pg C y^{-1} respectively in one hundred years. This additional uptake is directly comparable with the error of the most recent estimate of the net ocean carbon uptake of 2.2 $\pm$ 0.3 Pg C y^{-1} [Gruber et al., 2009]. The combination of both these perturbations results in a greater initial change to the air-sea CO_2 flux than either of the individual perturbations, and equilibrates more slowly giving an increased ocean uptake of around 0.5 Pg C y^{-1} after one hundred years. This is directly comparable to the error of the current IPCC estimate of 2.2 $\pm$ 0.5 Pg C y^{-1} [Denman et al., 2007]. Both these perturbations in general increase the strength of ingassing regions, and decrease the strength of outgassing regions, but the strength of ingassing in some regions—notably regions north and south of the outgassing tropical Pacific—-is reduced, with the explanation being that of reduced nutrient supply in these regions resulting from the changes in the primary production and the amount of detritus that breaks down to nutrient caused by the parameter perturbations.

The increase in the maximum photosynthetic rate also increases the primary productivity of the more productive upwelling regions, most notably year round in the tropical Pacific, and in the Southern Ocean during the southern summer. This results in a greater uptake of carbon during the southern summer months, altering the seasonal cycle of the air-sea CO_2 flux (see Section 5.6.1).

Decreasing the value of v_s from 10 to 6.36 m d^{-1}, and P^s_{max} from 0.6 to 0.11 d^{-1} decreases (causing outgassing) the initial global air-sea CO_2 flux by a greater amount than the increase in the CO_2 flux seen for the parameter increases described above, but account must be made of the set up of FAMOUS (see Section 5.3) in interpreting this. The reduction in the value of P^s_{max} causes a greater outgassing of CO_2 after one hundred years than the reduction in the value of v_s—a global outgassing equivalent to a loss of $\approx$ 1.6 Pg C y^{-1} from the ocean for the reduced P^s_{max}, and a global outgassing equivalent to a loss of $\approx$ 1 Pg C y^{-1} for the reduced value of v_s. An increase in the value of the rain-ratio (Υ_c), from 0.007 to 0.13 (see Section 5.2) initially results in an outgassing of CO_2 from the ocean amounting to a loss of around 2 Pg C y^{-1} from the ocean. This increases to 2.3 Pg C y^{-1} after around twenty years, an amount that is directly

comparable to the current estimated ocean carbon uptake (2.2 ± 0.3 [Gruber et al., 2009]). While the perturbation of the rain ratio is at the upper end of accepted values for the rain ratio, this result demonstrates the huge importance of the carbonate cycle in determining the chemistry and carbon uptake of the ocean.

The oceans play a major role in the global carbon cycle and in the regulation of the Earth's climate. The results of this work set possible bounds on the effect of ocean biogeochemical parameter uncertainties on the calculation of the air-sea CO_2 using a GCM. While uncertainties in the parameters and parameterisation of processes relating to other factors (e.g. cloud formation [Dufresne and Bony, 2008]) that control the climate and its reaction to anthropogenic forcing are considerably greater than those indicated here, the changes to the ocean uptake due to these parameter perturbations remain non-negligible, and hence it remains important to understand the reaction of the ocean ecosystem to anthropogenic climate forcing in greater detail.

Summary, conclusions and future directions

6.1 Thesis Summary

This thesis has explored the effect of uncertainty in the parameterisation of the ocean ecosystem on the role of the ocean in the carbon cycle in global circulation models. The primary focus has been on the influence of these uncertainties on the exchange of CO_2 between the atmosphere and ocean, a process that is crucial in regulating the increase in radiative forcing of the earth's climate due to anthropogenic emissions (see Section 1.3). The ocean ecosystem model used here is the HadOCC NPZD biogeochemical model (detailed in Section 3.2), which uses twenty parameters (described in Section 3.2.8) to calculate the role of the ocean ecosystem in the uptake and cycling of carbon in the ocean. HadOCC is used in both simple 1D ocean representations such as the HadOCC-GOTM model (Section 3.3), and in the full 3D global circulation models HadCM3 [Gordon et al., 2000], and its faster running derivative FAMOUS [Smith et al., 2008]—see Section 3.4.

The first step is to identify the HadOCC parameters which, given their uncertainty in value, introduce the greatest uncertainty to the air-sea CO_2 flux calculated by the model. To do this, in Chapter 4 a sensitivity analysis using the techniques discussed in Chapter 2 is performed on the 1D HadOCC-GOTM model. This requires the uncertainty in the values of the parameters to be established by comparison of the standard values with those used elsewhere. It is found that while many of the parameterisations are widely used, the values given to the parameters vary greatly, indicating considerable uncertainty (see Section 4.2.3). Based on the range of values found to be used, in Section 4.2.3, appropriate prior distributions for all the parameters are created, which are then sampled to create a suite of sets of different combinations of possible parameter values. These are run in the HadOCC-GOTM model to generate the data required to study the relationship between the uncertainty in value of each parameter, and the resulting outputs of the air-sea CO_2 flux, primary production, and deep detrital export. In Section 4.3, these outputs show large variation depending on the different parameter values used (see Table 4.5), showing that it is important to consider the uncertainty in the values of the ocean ecosystem parameters when interpreting the model results.

A variety of methods, from simple correlations, to more complex analyses as described in Chapter 2, are then used to identify which parameters have the greatest influence on the calculation of the air-sea CO_2 flux, the primary production and the deep detrital export (see Section 4.4). These find the air-sea CO_2 flux to be most influenced by uncertainty in the values of the parameters for the maximum photosynthetic rate of phytoplankton (P^s_{max}), the daily sinking rate of detritus (v_s) and the ratio of the total organic production that creates carbonate—the rain ratio Υ_c. These parameters are described in detail in Section 3.2.8. Variation in the value of these parameters alters the concentration of dissolved CO_2 in the surface waters by changing the inorganic carbon content. This changes the partial pressure of CO_2 (pCO_2^{sea}) of the ocean surface, which alters the partial pressure term in the gas transfer equation (Section 1.6), changing the air-sea CO_2 flux. The maximum photosynthetic rate (P^s_{max}) controls the growth of phytoplankton in the light-bathed ocean surface, regulating the uptake and fixing of dissolved carbon by primary production. Increasing the value of P^s_{max} increases the production and hence reduces the pCO_2^{sea} of the ocean surface. The daily detrital sink rate (v_s) affects the ocean surface pCO_2^{sea} by controlling the rate at which detritus, which breaks down to dissolved carbon, is exported away from the surface, with higher rates of export reducing the pCO_2^{sea} of the ocean surface and increasing the air-sea CO_2 flux into the ocean. The formation of carbonate, governed by the value of the rain-ratio (Υ_c) releases organic carbon into the ocean, changing the dissolved carbon content of the water and the pCO_2^{sea}. Higher values of the rain-ratio cause a greater release of organic carbon, increasing the pCO_2^{sea} and reducing the air-sea CO_2 flux into the ocean. Section 4.4.4 explores these effects in greater detail.

The primary production is found to be most influenced by the value of the initial slope of the photosythesis-irradiance curve (α), the maximum photosythentic rate (P^s_{max}), and the phytoplankton-specific mortality rate (m_0). Higher values of α and P^s_{max} cause higher productivity, while higher mortality reduces productivity. The export of detritus to the deep ocean is found to depend most on the values of the detrital sink rate (v_s), the rate of remineralisation of detritus below 100m (Rm_{deep}), and parameters that control the grazing on phytoplankton and detritus by zooplankton, the half saturation constant for grazing (K_F), and the maximum grazing rate (g_{max}). A faster daily sinking rate increases the amount of detritus in the deep ocean, while higher rates of zooplankton grazing and a greater remineralisation rate decrease detrital export. Section 3.2.8 and Section 4.4.4 describe the roles of these parameters in further detail. This work also reveals that the calculation of the primary production only depends strongly on the values of a few parameters, while the export is influenced by the value of around five parameters. In the case of the air-sea CO_2 flux, while the parameters detailed above are the most important, around half of those investigated are shown to be influential. Given the variation found in the calculated air-sea CO_2 flux (see Section 4.3 and Table 4.5), this indicates that the air-sea CO_2 flux is possibly the more difficult output to obtain with accuracy from simple ocean biogeochemistry models.

In Chapter 5, the parameters found to have the greatest effect on the air-sea CO_2 flux in the 1D HadOCC-GOTM—the maximum photosythetic rate of phytoplankton (P^s_{max}), the daily sinking rate of detritus (v_s) and the rain ratio (Υ_c)—are perturbed in the FAMOUS GCM by a degree that represents their uncertainty (see Section 5.2) to assess the global effect of ocean biogeochemical parameter uncertainty on the exchange of carbon between the atmosphere and ocean. These perturbations are found to have a detectable effect on the calculated air-sea CO_2 flux, with an initial signal of the order of current estimates of the annual ocean carbon sink (2.2 ± 0.5 Pg C y^{-1} Denman et al. [2007] and 2.2 ± 0.3 Pg C y^{-1} Gruber et al. [2009]). The unperturbed FAMOUS represents the pre-industrial climate, with very little net flux of carbon between the atmosphere and ocean. In agreement with the results of Chapter 4, the increase in value of P^s_{max} and in the value of v_s result in an increased air-sea CO_2 flux into the ocean, while decreasing the values of these parameters, or increasing the value of the rain ratio (Υ_c) results in the ocean outgassing CO_2 to the atmosphere. The atmosphere and ocean in FAMOUS are not fully coupled (see Section 5.3), but these results indicate the importance of biogeochemical parameter uncertainty to the calculation of oceanic carbon uptake, and set the bounds on the effect in a coupled set-up (see Section 5.7.1).

The initial upward perturbation of the value of the maximum photosythetic rate (P^s_{max}) results in a very rapid (less than one month) change in the net air-sea CO_2 flux into the ocean, due to increased primary productivity, especially in the Southern Ocean (see Sections 5.5.1.1 and 5.6.1). The initial upward perturbation of the detrital sink rate (v_s) has a smaller initial effect with a slight increase over the first few years of the perturbation (see Section 5.5.1.1). Combining these perturbations results in a greater increase in the air-sea CO_2 flux than the individual perturbations. These perturbations generally increase the strength of ingassing regions, and decrease that from outgassing regions. The effect of both of these perturbations on the global net air-sea CO_2 flux gradually decreases as the carbon in the ocean equilibrates with the atmosphere taking around 10^3 years to return to a zero net CO_2 flux equilibrium (see Section 5.5).

The downwards perturbation of the maximum photosythetic rate (P^s_{max}) and the detrital sink rate (v_s) parameters result in an initial outgassing of CO_2 equivalent to a loss from the ocean of ≈ 1.6 Pg C y^{-1} and ≈ 1 Pg C y^{-1} respectively (see Section 5.5.1). The upwards perturbation of the rain-ratio (Υ_c) results in the greatest initial outgassing of CO_2 from the ocean, equivalent to a loss of 2.3 Pg C y^{-1}, comparable with the estimated size of the current ocean carbon sink. However, this perturbation represents the upper end of possible values for the global rain-ratio.

While these results are limited by the de-coupled carbon cycle set-up of FAMOUS (see Sections 5.3 and 5.7.1), they show that the error in the calculated air-sea CO_2 flux due to uncertainty in the ocean biogeochemistry is on a similar scale to the uncertainty in the current estimates of the air-sea CO_2 flux. This means that the effect of unknowns in models of the ocean biogeochemistry is comparable to the range of ignorance in the system using current observation and modelling

techniques. Compared to other sources of error in climate study using GCMs, such as the modelling of the effect of clouds on radiative forcing (e.g., Dufresne and Bony [2008]), the short-term effect of uncertainty in ocean biogeochemistry models on global climate prediction appears to be slight. However, it is important to note that the error in the carbon uptake by the ocean constitutes a significant fraction ($> 10\%$) of the estimated mean uptake, and hence of global anthropogenic emissions, so changes of this scale are non-negligable in managing global carbon budgets.

6.2 Conclusions and future directions

As demonstrated by this work, our understanding of the ocean carbon cycle, and of its future evolution in the anthropogenic regime, is limited by two factors. The first is a limitation in our knowledge of the system, due in large part to the limited data currently available, and the problems associated with collecting oceanographic data. The second is the uncertainty in the size and rate of future climate forcing due to anthropogenic activity, and the effect that this has on global climate. To attempt to quantify this second limitation, the first limitation needs to be reduced as much as possible.

As currently represented in GCMs such as FAMOUS, the role of the marine ecosystem in the ocean carbon cycle, while able to provide indications, is insufficiently detailed to accurately predict the response of the ecosystem to climatic forcings and the effect of this response on the carbon cycle (e.g., Friedlingstein et al. [2006]). Ocean biogeochemical models need to include a more complete treatment of the ocean ecosystem, including different types of phytoplankton and their predators, more accurate representation of nutrient supply and limitation (including the role of micronutrients—see Section 1.5.2), a more detailed description of the export and content of detrital matter, and the effect of the changing pH of the ocean on the ecosystem and the calcium carbonate cycle.

Projects such as the C^4MIP climate-carbon cycle feedback model intercomparison [Friedlingstein et al., 2006] show that the global carbon cycle is highly sensitive to forcing by climatic change due to anthropogenic activity. However, there is huge uncertainty in the size, and in some cases, the direction of the feedback between the changing climate and the carbon cycle [Denman et al., 2007; Doney et al., 2009b]. The evolution of the ocean and of the ocean ecosystem in resonse to anthropogenic forcing of the climate is also highly uncertain. Current research indicates that the ocean uptake will increase in the first instance [Friedlingstein et al., 2006], but as ocean circulation reacts to increased global temperatures, and the ocean ecosystem reacts to changes in ocean circulation, temperature and chemistry, the future becomes uncertain [Sarmiento et al., 2004; Yoshikawa et al., 2008]. The reaction of the ocean ecosystem to the rapid lowering of the previously stable pH of the ocean (see section 1.5.3), which recent research shows is

taking place faster than previously thought [Steinacher et al., 2008], is of particular concern [Loubere et al., 2007; Doney et al., 2009a; Hofmann and Schellnhuber, 2009]. Here, the speed at which the perturbations to FAMOUS take effect—within a decade (see Sections 5.5.1.1 and 5.5.1.2)—is worth noting. Due to the time of turnover the ocean as a whole is often assumed to require centuries to react to changes, but recent observations suggest that both the biology (e.g. Behrenfeld et al. [2006], Doney [2006] and Polovina et al. [2008]) and the physical uptake of CO_2 (e.g. Park and Lee [2008] and Le Quéré et al. [2007]) are already reacting to anthropogenic forcing, and that the scale of this reaction is likely to increase.

In this setting, the results of my work on the FAMOUS GCM (Chapter 5) suggest that changes to the efficiency of the ocean ecosystem's ability to uptake carbon can potentially cause detectable effects on the global carbon cycle. The initial increase in carbon uptake by the ocean of around 0.5 Pg C y^{-1} due to the upwards perturbation of the parameters for the maximum photosynthetic rate (P^s_{max}), and detrital sink rate (v_s) (see Section 5.5.1.2), is equivalent to the uptake of an additional 5% of the current estimated annual anthropogenic forcing of the carbon cycle of around 10 Pg C y^{-1} (Canadell et al. [2007]). This matches the error of the estimate of annual anthropogenic carbon release ($\pm$ 5%), and while small is not negligible. While this is only 10% of the possible future release of 5 Pg C y^{-1} of terrestrial carbon due to climate carbon cycle feedbacks [Cox et al., 2000] it nevertheless remains important, especially in the long term role of the oceans in regulating the carbon cycle and the climate [Loubere et al., 2007].

To improve the accuracy of estimates of ocean carbon cycle climate feedbacks a clear challenge is to improve the accuracy and sensitivity to environmental change of the ocean biogeochemical models used in GCMs. Two general approaches currently being explored in the development of ocean biogeochemistry models are the use of more detailed modelling of the ecosystem and the use of trait based emergent-community modelling methods. The primary focus of more detailed modelling is on the use of phytoplankton functional types (PFTs) each with their own associated parameters to separately represent the behaviour of different types of phytoplankton and their biochemical role in the ocean, enabling a much more comphrehensive study of the reaction of the ocean ecosystem to climate forcing (e.g. Le Quéré et al. [2005]; Hood et al. [2006]).

However, while such models represent an ideal successor to the simpler NPZD-type models currently used, their design and development is based on our current knowledge of ocean biogeochemical systems. As a result, there is much debate over the use of PFT models due to the potentially subjective nature of the selection of PFT groups and the parameterisation of their characteristics arising from the relatively weak constraints of current knowledge (e.g. Hood et al. [2006]; Anderson [2005]; Flynn [2006]; Le Quéré [2006]—see also Section 1.8). Programmes such as the long-running Joint Global Ocean Flux Study (JGOFS), Sarmiento et al. [2004], have vastly improved our knowledge in recent years, but many unresolved questions remain, e.g. the role of carbonate ballasting in the export of organic carbon [Loubere et al., 2007], and the reaction

of the ecosystem to an increasingly acidic environment [Cao and Caldeira, 2008].

Trait-based emergent-behaviour modelling uses large numbers of stochastically assigned characteristics to initiate a system in which stronger subsets of characteristics out-compete others, evolving an ecosystem in which the structure is not pre-determined in the original model (e.g. Follows et al. [2007]; Litchman et al. [2007]). These models might offer a temporary solution to improving ocean biogeochemical climate predictions while the data neccessary for the more rigourous construction of PFT models is collected, but there are obvious issues of the considerable computational cost of such an approach.

The rapid development in remote sensing of the ocean surface holds huge potential to improve data and understanding on the ocean ecosystem. Current research is seeking to derive not only bulk production estimates, but information on phytoplankton functional type distribution from ocean colour (e.g., Hirata et al. [2008] and Nair et al. [2008]). Such information will hopefully provide greater insight into the effects of current climate forcing on the ocean ecosystem, and could perhaps be used to achieve greater accuracy in ocean biogeochemical models by regionally updating the values of phytoplankton parameters. However, remote sensing remains limited to collecting data on surface processes, and, as has been shown in the project, the important long term process of organic carbon export is in part governed by subsurface ecosystem behaviour. Studies such as the JGOFS programme [Sarmiento et al., 2004] remain essential.

The study of the uncertainty in climate predictions using GCMs has become a fundamental part of the study of climate [Randall et al., 2007]. This requires large numbers of model integrations to study the sensitivity of the model predictions to the parameterisation of climate regulating processes. Combined with the increased model complexity needed to better predict climate, this represents a challenge to computing technology, but one that is being answered by the increasing number and power of supercomputers available for climate research. These developments, and further developments in observation, understanding and accurate modelling of the Earth system processes that influence climate, will hopefully lead to a new generation of GCM climate models. These will be capable of more detailed climate predictions, and equally, will be able to provide detailed knowledge of the size and sources of uncertainty in these predictions.

Bibliography

Acheson, D. J. (1990). *Elementary Fluid Dynamics*. Oxford: Clarendon Press.

Anderson, T. (1993). A spectrally averaged model of light penetration and photosynthesis. *Limnology and Oceanography*, 38:1403–1419.

Anderson, T. (2005). Plankton functional type modelling: running before we can walk? *Journal of Plankton Research*, 27:1073–1081.

Anderson, T. and Pondaven, P. (2003). Non-redfield carbon and nitrogen cycling in the Sargasso Sea: pelagic imbalances and export flux. *Deep-Sea Research Part I*, 50:573–591.

Anderson, T., Ryabchenko, V., Fasham, M., and Gorchakov, V. (2007). Denitrification in the arabian sea: A 3D ecosystem modelling study. *Deep Sea Research Part I*, 54:2082–2119.

Aumont, O., Maier-Reimer, E., Blain, S., and Monfray, P. (2003). An ecosystem model of the global ocean including Fe, Si, P colimitations. *Global Biogeochemical Cycles*, 17.

Baker, K. and Frouin, R. (1987). Relation betwen photosynthetically available radiation and total insolation at the ocean surface under clear skies. *Limnology and Oceanography*, 32:1370–1377.

Baklouti, M., Faure, V., Pawlowski, L., and Sciandra, A. (2006). Investigation and sensitivity analysis of a mechanistic phytoplankton model implemented in an new modular numerical tool (eco3m) dedicated to biogeochemical modelling. *Progress in Oceanography*, 71:34–58.

Behrenfeld, M., O'Malley, R., Siegel, D., McClain, C., Sarmiento, J., Feldman, G., Milligan, A., Falkowski, P., Letelier, R., and Boss, E. (2006). Climate-driven trends in contemporary ocean productivity. *Nature*, 444:752–755.

Berner, R. (2003). The long-term carbon cycle, fossil fuels and atmospheric composition. *Nature*, 426:323–326.

Bigg, R. (2003). *Oceans and Climate*. Cambridge University Press.

Bindoff, N., Willebrand, J., Artale, V., Cazenave, A., Gregory, J., Gulev, S., Hanawa, K., Le Quéré, C., Levitus, S., Nojiri, Y., Shum, S., Talley, L., and Unnikrishnan, A. (2007). *Observations: Oceanic Climate Change and Sea Level.. In: Climate Change 2007: The Physical Science Basis. Contribution of Working Group 1 to the Fourth Assessment Report of the Intergovernmental Panel on Climate Change [Solomon, S., Qin, D. Manning, M., Chen, Z., Marquis, M., Avery, K.B., Tignor, M., Miller, H.L. (eds)]*. Cambridge University Press, Cambridge UK.

Boyd, P. and Law, C. (2001). The Southern Ocean Iron RElease Experiment (SOIREE) - introduction and summary. *Deep Sea Research II*, 48:2425–2438.

Brierley, C., Collins, M., and Thorpe, A. (2008). The impact of perturbations to ocean-model parameters on climate and climate change in a coupled model. *Climate Dynamics*.

Bryden, H., Longworth, H., and Cunningham, S. (2005). Slowing of the atlantic meridional overturning circulation at 25 n. *Nature*, 438:655–657.

Burchard, H., Bolding, K., and Ruiz Villarreal, M. (1999). GOTM. a general ocean turbulence model. Theory, applications and test cases. Research article, European Commission.

Burnham, K. and Anderson, D. (2002). *Model selection and multimodel inference : a practical information-theoretic approach*. Springer.

Canadell, J., Le Quéré, C., Raupacha, M., Field, C., Buitenhuis, E., Ciais, P., Conway, T., Gillett, N., Houghton, R., and Marland, G. (2007). Contributions to accelerating atmospheric CO_2 growth from economic activity, carbon intensity, and efficiency of natural sinks. *Proceedings of the National Academy of Sciences of the USA*, 104:18866–18870.

Cao, L. and Caldeira, K. (2008). Atmospheric CO_2 stabilization and ocean acidification. *Geophysical Research Letters*, 35:L19609.

Carlin, B. and Louis, T. (2008). *Bayesian Methods for Data Analysis*. Chapman and Hall/CRC.

Carr, M., Friedrichs, M., Schmeltz, M., Aita, M., D., A., Arrigo, K., Asanuma, I., Aumont, O., Barber, R., Behrenfeld, M., Bidigare, R., Buitenhuis, E., Campbell, J., Ciotti, A., Dierssen, H., Dowell, M., Dunne, J., Esaias, W., Gentili, B., Gregg, W., Groom, S., Hoepffner, N., Ishizaka, J., Kameda, T., Le Quéré, C., Lohrenz, S., Marra, J., Mélino, F., Moore, K., Moreld, A., Reddy, T., Ryan, J., Scardi, M., Smyth, T., Turpie, K., Tilstone, G., Waters, K., and Y., Y. (2006). A comparison of global estimates of marine primary production from ocean color. *Deep Sea Research Part II*, 53:741–770.

Chuck, A., Tyrell, T., Totterdell, I., and Holligan, P. (2005). The oceanic response to carbon emissions over the next century: investigation using three ocean carbon cycle models. *Tellus series B-chemical and physical meteorology.*, 57(1):70–86.

Clark, P., Pisias, N., Stocker, T., and Weaver, A. (2002). The role of the thermohaline circulation in abrupt climate change. *Nature*, 415:863–869.

Cloern, J., Grenz, C., and Videgar-Lucas, L. (1995). An empirical model of the phytoplankton chlorophyll:carbon ratio- the conversion factor between productivity and growth rate. *Limnology and Oceanography*, 40:1313–1321.

Collins, M., Brierley, C., MacVean, M., Booth, B., and Harris, G. (2007). The sensitivity of the rate of transient climate change to ocean physics perturbations. *Journal of Climate*, 20:2315–2320.

Cox, P., Betts, R., Jones, C., Spall, S., and Totterdell, I. (2000). Acceleration of global warming due to carbon-cycle feedbacks in a coupled climate model. *Nature*, 408:184–187.

Curry, J. and Webster, P. (1999). *Thermodynamics of Atmospheres and Oceans*. AP international geophysics series.

Denman, K., Brasseur, G., Chidthaisong, A., Ciasis, P., Cox, P., Dickinson, R., Hauglustaine, D., Heinze, C., Holland, E., Jacob, D., Lohmann, U., Ramachandran, S., da Silva Dias P.L., Wofsy, S., and Zhang, X. (2007). *Couplings Between Changes in the Climate System and Biogeochemistry. In: Climate Change 2007: The Physical Science Basis. Contribution of Working Group 1 to the Fourth Assessment Report of the Intergovernmental Panel on Climate Change [Solomon, S., Qin, D. Manning, M., Chen, Z., Marquis, M., Avery, K.B., Tignor, M., Miller, H.L. (eds)]*. Cambridge University Press, Cambridge UK.

Doney, S. (2006). Oceanography: Plankton in a warmer world. *Nature*, 444:695–696.

Doney, S., Fabry, V., Feely, R., and Kleypas, J. (2009a). Ocean acidification: The other CO_2 problem. *Annual Review of Marine Sciences*, pages 169–192.

Doney, S., Tilbrook, B., Roy, S., Metzl, N., Le Quéré, C., Hood, M., Feely, R., and Bakker, D. (2009b). Surface ocean CO_2 variability and vulnerability. *Deep Sea Research part II*, 56:504–511.

Druon, J.-N. and Le Fèvre, J. (1999). Sensitivity of a pleagic ecosystem model to variations of process parameters within a realistic range. *Journal of Marine Systems*, 19:1–26.

Dufresne, J.-L. and Bony, S. (2008). An assessment of the primary sources of spread of global warming estimates from coupled atmosphere-ocean models. *Journal of Climate*, 21:5135–5144.

Eppley, R. and Peterson, B. (1979). Particulate organic matter flux and planktonic new production in the deep ocean. *Nature*, 282:677 – 680.

Fangohr, S., Woolf, D., Jeffery, C., and Robinson, I. (2008). Calculating long-term global air-sea flux of carbon dioxide using scatterometer, passive microwave, and model reanalysis wind data. *Journal of Geophysical research*, 113:C09032.

Fasham, M. (2003). *Ocean Biogeochemistry: The role of the ocean carbon cycle in global change*. Springer.

Fennel, K., Losch, M., Schröter, J., and Wenzel, M. (2001). Testing a marine ecosystem model: sensitivity analysis and parameter optimisation. *Journal of Marine Systems*, 28:45–63.

Field, C., Behrenfeld, M., Randerson, J., and Falkowski, P. (1998). Primary production of the biosphere: Integrating terrestrial and oceanic components. *Science*, 281:237 – 240.

Flynn, K. (2006). Reply to horizons article 'Plankton functional type modelling: running before we can walk?' II. putting trophic functionality into plankton functional types. *Journal of Plankton Research*, 28:873–875.

Follows, M., Dutkiewicz, S., Grant, S., and Chisholm, W. (2007). Emergent biogeography of microbial communities in a model ocean. *Science*, 315.

Forster, P., Ramaswamy, V., Artaxo, P., Berntsen, T., Betts, R., Fahey, D., Haywood, J., Lean, J., Lowe, D., Myhre, G., Nganga, J., Prinn, R., Raga, G., Schulz, M., and Van Dorland, R. (2007). *Changes in Atmospheric Consitiuents and in Radiative Forcing. In: Climate Change 2007: The Physical Science Basis. Contribution of Working Group 1 to the Fourth Assessment Report of the Intergovernmental Panel on Climate Change [Solomon, S., Qin, D. Manning, M., Chen, Z., Marquis, M., Avery, K.B., Tignor, M., Miller, H.L. (eds)]*. Cambridge University Press, Cambridge UK.

Frenette, J.-J., Demers, S., Legendre, L., and Dodson, J. (1993). Lack of agreement among models for estimation the photosynthetic parameters. *Limnology and Oceanography*, 38(3):679–687.

Freund, J. (1992). *Mathematical Statistics, fith edition.* Prentice and Hall International Ltd.

Friedlingstein, P., Cox, P., Betts, R., Bopp, L., Von Bloh, W., Brovkin, V., Cadule, P., Doney, S., Eby, M., Fung, I., Bala, G., John, J., Jones, C., Joos, F., Kato, T., Kawamiya, M., Knorr, W., Lindsay, K., Matthews, H., Raddatz, T., Rayner, P., Reick, C., Roeckner, E., Schnitzler, K. G., Schnur, R., Strassmann, K., Weaver, A. J., Yoshikawa, C., and Zeng, N. (2006). Climate-carbon cycle feedback analysis: Results from the C4MIP model intercomparison. *Journal of Climate*, 19:3337–33353.

Fujii, M. and Chai, F. (2007). Modelling carbon and silicon cycling in the equatorial pacific. *Deep-Sea Research II*, 54:496–520.

Fujii, M., Ikeda, M., and Yamanka, Y. (2005). Roles of biogeochemical processes in the oceanic carbon cycle described with a simple coupled physical biogeochemical model. *Journal of Oceanography*, 61:803–815.

Garcia, H., Locarnini, R.A.and Boyer, T., and Antonov, J. (2006). World ocean atlas 2005, volume 4: Nutrients: phosphate, nitrate, silicate. Research article, NOAA Atlas NESDIS.

Geider, R., MacIntyre, H., and Kana, T. M. (1997). Dynamic model of phytoplankton growth and acclimation: responses of a balanced growth rate and the chlorophyll *a*:carbon ratio to light, nutrient-limitation and temperature. *Marine Ecology Progress Series*, 148:187–200.

Geider, R., MacIntyre, H., and Kana, T. M. (1998). A dynamic regulatory model of phytoplanktonic acclimation to light, nutrients, and temperature. *Limnology and Oceanography*, 43(4):679–694.

Gordon, C., Cooper, C., Senior, C., Banks, H., Gregory, J., Johns, T., Mitchell, J., , and Wood, R. (2000). The simulation of SST, sea ice extents and ocean heat transports in a version of the Hadley Centre coupled model without flux adjustments. *Journal of Climate Dynamics*, 16:147–168.

Grafen, A. and Hails, R. (2002). *Modern Statistics for the Life Sciences*. Oxford University Press.

Gregg, W. and Casey, N. (2007). Modeling coccolithophores in the global oceans. *Deep-sea research. Part II*, 54.

Gruber, N., Gloor, M., Mikaloff-Fletcher, S., Doney, S., Dutkiewicz, S., Follows, M., Gerber, M., Jacobson, A., Joos, F., Lindsay, K., Menemenlis, D., Mouchet, A., Muller, S., Sarmiento, J., and Takahsahi, T. (2009). Oceanic sources, sinks, and transport of atmospheric CO_2. *Global biogeochemical cycles*, 23.

Hankin, R. and Lee, A. (2006). A new family of non-negative distributions. *Australian and New Zealand Journal of Statistics*, 48:67–78.

Hirata, T., Aiken, J., Hardman-Mountford, N., Smyth, T., and R.G., B. (2008). An absorption model to determine phytoplankton size classes from satellite ocean colour. *Remote Sensing of Environment*, 112:3153–3159.

Hofmann, M. and Schellnhuber, H.-J. (2009). Oceanic acidification affects marine carbon pump and triggers extended marine oxygen holes. *Proceedings of the National Academy of Sciences USA*, 106:3017–3022.

Hood, R., Laws, E., Armstrong, R., Bates, N., Brown, C., Carlson, C., Chai, F., Doney, S., Falkowski, P., Feely, R., Friedrichs, M., Landry, M., Moore, J., Nelson, D., Richardson, T., Salihoglu, B., Schartau, M., Toole, D., and Wiggert, J. (2006). Pelagic functional group modeling: Progress, challenges and prospects. *Deep Sea Research Part II*, 53:459–512.

Houghton, R. (2007). Balancing the global carbon budget. *Annual Review Earth and Planetary Sciences*, 35:313–347.

Huntingford, C., Lowe, J., Booth, B., Jones, C., Harris, G., Gohar, L., and Meir, P. (2009). Contributions of carbon cycle uncertainty to future climate projection spread. *TELLUS series B: Chemical and physical meteorology*, 61B:355–360.

Iglesias-Rodriguez, D., Halloran, P., Rickaby, R., Hall, I., Colmenero-Hidalgo, E., Gittins, J., Green, D., Tyrrell, T., Gibbs, S., Dassow, P., Rehm, E., Armbrust, E., and Boessenkool, K. (2008). Phytoplankton calcification in a high-CO_2 world. *Science*, 320:336 – 340.

Jacobson, M., Charlson, J., and Rodhe, H. Orians, G. (2000). *Earth System Science*. Academic Press.

Jansen, E., Overpeck, J., Briffa, K., Duplessy, J.-C., Joos, F., Masson-Delmotte, V., Olago, D., Otto-Bliesner, B., Peltier, W., Rahmstorf, S., Ramesh, R., Raynaud, D., Rind, D., Solomina, O., Villalba, R., and Zhang, D. (2007). *Paleoclimate. In: Climate Change 2007: The Physical Science Basis. Contribution of Working Group 1 to the Fourth Assessment Report of the Intergovernmental Panel on Climate Change [Solomon, S., Qin, D. Manning, M., Chen, Z., Marquis, M., Avery, K.B., Tignor, M., Miller, H.L. (eds)]*. Cambridge University Press, Cambridge UK.

Jickells, T., An, S., Andersen, K., Baker, R., Bergametti, G., Brooks, N., Cao, J., Boyd, P., Duce, R., Hunter, K., Kawahata, H., Kubilay, N., LaRoche, J., Liss, P., Mahowald, N., Prospero, J., Ridgwell, A., Tegen, I., and Torres, R. (2005). Global iron connections between desert dust, ocean biogeochemistry, and climate. *Science*, 308:67 – 71.

Jones, C., Cox, P., and Huntingford, C. (2006). Climate-carbon cycle feedbacks under stabilization: uncertainty and observational constraints. *TELLUS series B*, 58:603–613.

Jones, C., Gregory, J., Thorpe, R., Cox, P., Murphy, J., Sexton, D., and P., V. (2005). Systematic optimisation and climate simulation of FAMOUS, a fast version of HadCM3. *Climate Dynamics*, 25:189–204.

Kawamiya, M., Kishi, M., and Suginohara, N. (2000). An ecosystem model for the North Pacific embedded in a general circulation model part I: Model description and characteristics of spatial distributions of biological variables. *Journal of Marine Systems*, 25:129–157.

Kettle, H. and Merchant, C. (2008). Modeling ocean primary production: sensitivity to spectral resolution of attenuation and absorption of light. *Progress In Oceanography*, 78:135–146.

Key, R., Kozyr, A., Sabine, C., Lee, K., Wanninkhof, R., Bullister, J., Feely, R., Millero, F., Mordy, C., and Peng, T.-H. (2004). A global ocean climatology: Results from Global Data Analysis Project (GLODAP). *Global Biogeochemical Cycles*, 18.

Kohfeld, K., Le Quéré, C., Harrison, S., and Anderson, R. (2005). Role of marine biology in glacial-interglacial CO_2 cycles. *Science*, 308:74 – 78.

Kurahashi-Nakamura, T., Abe-Ouchi, A., and Yamanaka, Y. (2009). Effects of physical changes in the ocean on the atmospheric pCO_2: glacial-interglacial cycles. *Climate Dynamics*.

Le Quéré, C. (2006). Reply to horizons article 'Plankton functional type modelling: running before we can walk?' I. abrupt changes in marine ecoystems? *Journal of Plankton Research*, 28:871–872.

Le Quéré, C., Harrison, S., Prentice, C., Buitenhuis, E., Aumont, O., Bopp, L., Claustre, H., Da Cunha, L., Geider, R., Giraud, X., Klaas, C., Kohfeld, K., Legendre, L., Manizza, M., Platt, T., Rivkin, R., Sathyendranath, S., Uitz, J., Watson, A., and Wolf-Gladrow, D. (2005). Ecosystem dynamics based on plankton functional types for global ocean biogeochemistry models. *Global Change Biology*, 11:2016–2040.

Le Quéré, C., Rodenbeck, C., E.T., B., Conway, T., Langenfelds, R., Gomez, A., Labuschagne, C., Ramonet, M., Nakazawa, T., Metzl, N., Gillett, N., and Heimann, M. (2007). Saturation of the southern Ocean CO_2 sink due to recent climate change. *Science*, 316:1735–1738.

Lee, K., Tong, L., Millero, F., Sabine, C., Dickson, A., Goyet, C., Park, G.-H., Wanninkhof, R., Feely, R., and Key, R. (2006). Global relationships of total alkalinity with salinity and temperature in surface waters of the world's oceans. *Geophysical Research Letters*, 33(19).

Levitus, S., Conkright, M., Reid, J., Najjar, R., and Mantyla, A. (1993). Distribution of nitrate, phosphate and silicate in the world oceans. *Progress in Oceanography*, 31:245–273.

Litchman, E., Klausmeier, C., Schofield, O., and Falkowski, P. (2007). The role of functional traits and trade-offs in structuring phytoplankton communities: scaling from cellular to ecosystem level. *Ecology Letters*, 10:1170–1181.

Loubere, P., Siedlecki, S., and Bradtmiller, L. (2007). Organic carbon and carbonate fluxes: Links to climate change. *Deep Sea Research II*, 54:437–446.

Luyssaert, S., E.D., S., Brner, A., Knohl0, A., Hessenmller, D., Law, B., Ciais, P., and Grace, J. (2008). Old-growth forests as global carbon sinks. *Nature*, 455:213–215.

Mackenzie, F., Lerman, A., and Andersson, A. (2004). Past and present of sediment and carbon biogeochemical cycling models. *Biogeosciences*, 1:11–32.

Martin, A. and Pondaven, P. (2006). New primary production and nitrification in the western subtropical North Atlantic: A modeling study. *Global Biogeochemical Cycles*, 20:GB4014.

McKay, M., Beckman, R., and Conover, W. (1979). A comparison of three methods for selecting values of input variables in the analysis of output from a computer code. *Technometrics*, 21:239–245.

Meehl, G., Stocker, T., Collins, W., Friedlingstein, P., Gaye, A., Gregory, J., Kitoh, A., Knutti, R., Murphy, J., Noda, A., Raper, S., Watterson, I., Weaver, A., and Zhao, Z.-C. (2007). *Global Climate Projections. In: Climate Change 2007: The Physical Science Basis. Contribution of Working Group 1 to the Fourth Assessment Report of the Intergovernmental Panel on Climate Change [Solomon, S., Qin, D. Manning, M., Chen, Z., Marquis, M., Avery, K.B., Tignor, M., Miller, H.L. (eds)]*. Cambridge University Press, Cambridge UK.

Morel, A. (1988). Optical modelling of the upper ocean in relation to its biogenous matter content (case I waters). *Journal of Geophys. Res.*, 93:10,749–10768.

Morel, A. and Maritorena, S. (2001). Bio-optical properties of oceanic water: a reappraisal. *Journal of Geophys. Res.*, 106:7163–7180.

Murphy, J., Sexton, M., Barnett, D., Jones, G., Webb, M., Collins, M., and D.A., S. (2004). Quantification of modelling uncertainties in a large ensemble of climate change simulations. *Nature*, 430:768–772.

Murray, J. (2000). *Oceans- in Earth System Science (Jacobson, Charlson, Rodhe, Orians)*. Academic Press.

Nair, A., Sathyendranath, S., Platt, T., Morales, J., Stuart, V., Forget, M.-H., Devred, E., and Bouman, H. (2008). Remote sensing of phytoplankton functional types. *Remote Sensing of Environment*, 112:3366–3375.

Najjar, R., Jin, X., Louanchi, F., Aumont, O., Caldeira, K., Doney, S., Dutay, J.-C., Follows, M., Gruber, N., Joos, F., Lindsay, K., Maier-Reimer, E., Matear, R., Matsumoto, K., Monfray, P., Mouchet, A., Orr, J., Plattner, G.-K., Sarmiento, J., Schlitzer, R., Slater, R., Weirig, M.-F., Yamanaka, Y., and Yool, A. (2007). Impact of circulation on export production, dissolved organic matter, and dissolved oxygen in the ocean: results from phase II of the Ocean Carbon-cycle Model Intercomparison Project (OCMIP-2). *Global Biogeochemical Cycles*, 21.

Orr, J., Fabry, V., Aumont, O., Bopp, L., Doney, S., Feely, R., Gnanadesikan, A., Gruber, N., Ishida, A., Joos, F., Key, R., Lindsay, K., Maier-Reimer, E., Matear, R., Monfray, P., Mouchet, A., Najjar, R., Plattner, G., Rodgers, K., Sabine, C., Sarmiento, J., Schlitzer, R., Slater, R., I.J., T., Weirig, M., Yamanaka, Y., and Yool, A. (2005). Anthropogenic ocean acidification over the twenty-first century and its impact on calcifying organisms. *Nature*, 437:681–686.

Pahlow, M., Vézina, F., Casault, B., Maass, H., Malloch, L., Wright, D., and Lu, Y. (2008). Adaptive model of plankton dynamics for the North Atlantic. *Progress in Oceanography*, 76:151–191.

Palmer, J. (1998). Hadley Centre Technical note 53: The ocean carbon cycle in the Unified Model.

Palmer, J. and Totterdell, I. (2001). Production and export in a global ecosystem model. *Deep-Sea Research I*, 48:1169–1198.

Park, G.-H. and Lee, K.and Tishchenko, P. (2008). Sudden, considerable reduction in recent uptake of anthropogenic CO_2 by the East/Japan sea. *Geophysical Research Letters*, 35.

Pätsch, J., Kühn, W., Radach, G., Santana Casiano, J., Gonzalez Davila, M., Neuer, S., Freudenthal, T., and Llinas, O. (2002). Interannual variability of carbon fluxes at the North Atlantic Station ESTOC. *Deep-Sea Research II*, 49:253–288.

Peacock, S., Lane, E., and Restrepo, J. (2006). A possible sequence of events for the generalized glacial-interglacial cycle. *Global Biogeochemical Cycles*, 20:GB2010.

Pollard, R., Salter, I., Sanders, R., Lucas, M., Moore, M., Mills, R., Statham, P., Allen, J., Baker, A., Bakker, D., Charette, M., Fielding, S., Fones, G., French, M., Hickman, A., Holland, R., Hughes, A., Jickells, T., Lampitt, R., Morris, P., Nédélec, F., Nielsdóttir, M., Planquette, H., Popova, E., Poulton, A., Read, J., Seeyave, S., Smith, T., Stinchcombe, M., Taylor, S., Thomalla, S., Venables, H., Williamson, R., and Zubkov, M. (2009). Southern ocean deep-water carbon export enhanced by natural iron fertilization. *Nature*, 457:577–580.

Polovina, J., E.A., H., and Abecassis, M. (2008). Ocean's least productive waters are expanding. *Geophysical Research Letters*, 35.

Popova, E., Lozano, C., Srokosz, M., Fasham, M., Haley, P., and Robinson, A. (2002). Coupled 3D physical and biological modelling of the mesoscale variability observed in North-East Atlantic in spring 1997: biological processes. *Deep-Sea Research I*, 49:1741–1768.

Randall, D., Wood, R., Bony, S., Colman, R., Fichefet, T., Fyfe, J., V., K., Pitman, A., Shukla, J., Srinivasan, J., Stouffer, R., Sumi, A., and Taylor, K. (2007). *Climate Models and Their Evaluation. In: Climate Change 2007: The Physical Science Basis. Contribution of Working Group 1 to the Fourth Assessment Report of the Intergovernmental Panel on Climate Change [Solomon, S., Qin, D. Manning, M., Chen, Z., Marquis, M., Avery, K.B., Tignor, M., Miller, H.L. (eds)]*. Cambridge University Press, Cambridge UK.

Reay, D., Hewitt, C., Smith, K., and Grace, J. (2007). *Greenhouse Gas Sinks*. CABI.

Ricklefs, R. (1990). *Ecology*. W.H. Freeman and Company. New York.

Riebesell, U., Schul, K., Bellerby, R., Botros, M., Fritsche, P., Meyerhfer, M., Neil, C., Nondal, G., Oschlies, A., J., W., and Zllner, E. (2007). Enhanced biological carbon consumption in a high CO_2 ocean. *Nature*, 450:545–548.

Rutgersson, A., Norman, M., Schneider, B., Pettersson, H., and Sahlee, E. (2008). The annual cycle of carbon dioxide and parameters influencing the air-sea carbon exchange in the Baltic proper. *Journal of Marine Systems*, 74:381–394.

Sabine, C., Feely, R., Gruber, N., Key, M., Lee, K., Bullister, J., Wanninkhof, R., Wong, C., Wallace, D., Tilbrook, B., Millero, F., Peng, T.-H., Kozyr, A., Ono, T., and Rios, A. (2004). The oceanic sink for anthropogenic CO_2. *Science*, 305:367–371.

Saltelli, A., Chan, K., and Scott, E. (2001). *Sensitivity Analysis*. John Wiley & Sons Ltd.

Sarmiento, J., Dunne, J., and Armstrong, R. (2004). Do we now understand the ocean's biological pump? *U.S. JGOFS News*, 12.

Sarmiento, J. and Gruber, N. (2006). *Ocean Biogeochemical Dynamics*. Princeton University Press.

Sarmiento, J., Tertia, H., Stouffer, R., and Manabe, S. (1998). Simulated response of the ocean carbon cycle to anthropogenic climate warming. *Nature*, 393:245–249.

Schneider, B., Bopp, L., and Gehlen, M. (2008). Assessing the sensitivity of modeled air-sea CO_2 exchange to the remineralization depth of particulate organic and inorganic carbon. *Global Biogeochemical Cycles*, 22.

Scholes, R., Monteiro, P., Sabine, C., and Canadell, J. (2009). Systematic long-term observations of the global carbon cycle. *Trends in Ecology Evolution*, 24:427–430.

Schuster, U. and Watson, A. (2007). A variable and decreasing sink for atmospheric CO_2 in the North Atlantic. *Journal of Geophysical Research*, 112:C11006.

Smith, J. and Smith, P. (2002). *Environmental Modelling*. Oxford University Press.

Smith, R. (2009). Personal communication.

Smith, R., Gregory, J., and Osprey, A. (2008). A description of the FAMOUS (version XDBUA) climate model and control run. *Geoscientific Model Development Discussions*, 1:147–185.

Smith, R. and Marotzke, J. (2008). Factors influencing anthropogenic carbon dioxide uptake in the North Atlantic in models of the ocean carbon cycle. *Journal of Climate Dynamics*, 31:599–613.

Solomon, S., Qin, D., Manning, M., Chen, Z., Marquis, M., Avery, K., Tignor, M., and Miller, H. (2007). *IPCC, 2007: Summary for Policymakers. In: Climate Change 2007: The Physical Science Basis. Contribution of Working Group 1 to the Fourth Assessment Report of the Intergovernmental Panel on Climate Change [Solomon, S., Qin, D. Manning, M., Chen, Z., Marquis, M., Avery, K.B., Tignor, M., Miller, H.L. (eds)]*. Cambridge University Press, Cambridge UK.

Stainforth, D., Aina, T., Christensen, C., Collins, M., Faull, N., Frame, D., Kettleborough, J., Knight, S., Martin, A., Murphy, J., Piani, C., Sexton, D., Smith, L., Spicer, R., Thorpe, A., and M.R., A. (2005). Uncertainty in predictions of the climate response to rising levels of greenhouse gases. *Nature*, 433:403–406.

Steinacher, M., Joos, F., Frölicher, T. L., Plattner, G.-K., and Doney, S. C. (2008). Imminent ocean acidification projected with the NCAR global coupled carbon cycle-climate model. *Biogeosciences Discuss*, 5:4353–4393.

Stephens, B., Gurney, K., Tans, P., Sweeney, C., Peters, W., Bruhwiler, L., Ciais, P., Ramonet, M., Bousquet, P., Nakazawa, T., Aoki, S., Machida, T., Inoue, G., Vinnichenko, N., Lloyd, J., Jordan, A., Heimann, M., Shibistova, O., Langenfelds, R., Steele, L., Francey, R., and Denning, A. (2007). Weak northern and strong tropical land carbon uptake from vertical profiles of atmospheric CO_2. *Science*, 316:1732 – 1735.

Takahashi, T. (2004). The fate of industrial carbon dioxide. *Science*, 305:352–353.

Takahashi, T., Sutherland, S., Sweeny, C., Poisson, A., Metzl, N., Tilbrook, B., Bates, N., Wanninkhof, R., Feely, R., Sabine, C., Olafsson, J., and Nojiri, Y. (2002). Global sea-air CO_2 flux based on climatological surface ocean pCO_2, and seasonal biological and temperature effects. *Deep-Sea Research II*, 49:1601–1622.

Tjiputra, J., Polzin, D., and A.M.E., W. (2007). Assimilation of seasonal chlorophyll and nutrient data into an adjoint three-dimensional ocean carbon cycle model: Sensitivity analysis and ecosytem parameter optimization. *Global Biogeochemical Cycles*, 21.

Tol, R. (2008). Why worry about climate change? A research agenda. *Environmental Values*, 17:437–470.

Waniek, J. and Holiday, P. (2006). Large-scale physical controls on phytoplankton growth in the central Irminger Sea, part II: model study of the physical and meterological preconditioning. *Journal of Marine Systems*, 59:219–237.

Wanninkhof, R. (1992). Relationship between wind speed and gas exchange over the ocean. *Journal of Geophysical Research Oceans*, 97:7373–7382.

Wanninkhof, R. and McGillis, W. (1999). A cubic relationship between air-sea CO_2 exchange and wind speed. *Geophysical Research Letters*, 26:1889–1892.

Watson, A. and Orr, J. (2003). *Carbon dioxide fluxes in the global ocean: In Ocean Biogeochemistry (M.J. Fasham)*. Springer.

Webb, M., Senior, C., Sexton, D., Ingram, W., Williams, K., Ringer, M., McAvaney, B., Colman, R., Soden, B., Gudge, R., Knutson, T., Emori, S., Ogura, T., Tsushima, Y., Andronova, N., Li, B., Musat, I., Bony, S., and Taylor, K. (2006). On the contribution of local feedback mechanisms to the range of climate sensitivity in two GCM ensembles. *Climate Dynamics*.

Wilson, R., Millero, F., Taylor, J., Walsh, P., Christensen, V., Jennings, S., and Grosell, M. (2009). Contribution of fish to the marine inorganic carbon cycle. *Science*, 323:359–362.

Yool, A. (2007). Making the paper. *Nature (reports climate change)*, 3:46.

Yoshikawa, C., Kawamiya, M., Kato, T., Yamanaka, Y., and Matsuno, T. (2008). Geographical distribution of the feedback between future climate change and the carbon cycle. *Journal of geophysical research. Biogeosciences*, 113.

Zielinski, O., Llinás, O., Oschlies, A., and Reuter, R. (2002). Underwater light field and its effect on a one-dimensional ecosystem model at station ESTOC north of the Canary Islands. *Deep-Sea Research II*, 49:3529–3542.

Zubkov, V. and Tarran, G. (2008). High bacterivory by the smallest phytoplankton in the North Atlantic Ocean. *Nature*, 455:224–226.